Materials and Solidification 2026, **2**: 9580023

https://doi.org/10.26599/MAS.2026.9580023

Review

Crystallization and solidification of scalable metal halide perovskite films for photovoltaics

Qirui Deng[1,#], Hu Guo[1,#], Ruihao Chen[2], Yuanhang Cheng[1,*]

[1] *School of New Energy, Nanjing University of Science and Technology, Jiangyin, 214443, China.*

[2] *State Key Laboratory of Solidification Processing, Center for Nano Energy Materials, School of Materials Science and Engineering, Northwestern Polytechnical University, Xi'an 710072, China.*

*Q. Deng and H. Guo contributed equally to this work.

*Corresponding author.

E-mail: yhcheng@njust.edu.cn

Received: August 20, 2025; Revised: September 8, 2026; Accepted: September 17, 2026

Abstract: Metal halide perovskite photovoltaics have emerged as promising next-generation solar technologies owing to their high efficiency and compatibility with low-temperature manufacturing. Although small-area perovskite solar cells have achieved certified efficiencies around 28%, scalable fabrication of large-area perovskite films and modules remains a major challenge for commercialization. During scale-up, film formation becomes highly sensitive to coupled transport and solidification processes, including fluid flow, solvent evaporation, vapor transport, supersaturation

evolution, nucleation, crystal growth, and phase conversion. These processes generate spatiotemporal heterogeneities that cause nonuniform crystallization, defect formation, and module-level performance losses. In this Review, we establish a crystallization-centered framework for understanding large-area perovskite film fabrication across both solution-based and vapor-based deposition routes. Solution processing methods are discussed from the perspectives of wet-film hydrodynamics and solvent-mediated crystallization, while vapor-based routes are analyzed in terms of precursor transport, surface reaction kinetics, and non-equilibrium growth. Previous studies are further used to relate precursor transport and perovskite crystallization control to film uniformity, device performance, and operational stability. Finally, we discuss emerging strategies for crystallization control and scalable manufacturing toward reliable, high-throughput perovskite photovoltaic modules.

Keywords: Large-area perovskite films; scalable deposition; crystallization control; solution processing; vapor-phase deposition; perovskite photovoltaics

1 Introduction: scalable perovskite film formation and deposition strategies

Photovoltaic (PV) technologies have become one of the cornerstones of the global energy transition, driven by continuous reductions in manufacturing cost and sustained improvements in device performance [1,2]. Among emerging PV technologies, metal halide perovskite solar cells (PVSCs) have attracted enormous attention because of their outstanding optoelectronic properties, tunable bandgap, long carrier diffusion length, and compatibility with low-temperature processing. Since the first report of PVSCs with a power conversion efficiency (PCE) of approximately 3.8% in 2009, the certified efficiency of single-junction PVSCs has rapidly increased to 28% in 2026 [3,4].

These remarkable advances have established perovskites as one of the most promising candidates for next-generation PV technologies. Despite these rapid improvements, commercialization of perovskite PV technology requires a fundamental transition from laboratory-scale devices to large-area manufacturing. While high-efficiency small-area PVSCs are routinely fabricated by spin coating, this technique suffers from low material utilization, discontinuous processing, and limited compatibility with industrial manufacturing. Practical production instead requires scalable deposition technologies capable of producing large-area perovskite films with high thickness uniformity, low defect density, and excellent reproducibility. Consequently, scalable solution-based coating and vapor-based deposition techniques have become central research directions for translating perovskite PV from laboratory demonstrations to industrial manufacturing.

Unlike spin coating, where solvent removal occurs rapidly and relatively uniformly over a small substrate, scalable deposition involves significantly longer processing times and much larger transport length scales [5]. Variations in wet-film thickness, solvent evaporation, precursor concentration, temperature, and precursor flux inevitably develop across the substrate, leading to spatially heterogeneous supersaturation and asynchronous crystallization. These spatial variations generate nonuniform perovskite nucleation, grain growth, phase distribution, and defect formation, ultimately degrading the perovskite film homogeneity, device reproducibility, and long-term operational stability. Therefore, regardless of the deposition technique employed, the key scientific challenge in scalable perovskite manufacturing is no longer simply depositing precursor materials, but achieving synchronized and spatially uniform crystallization dynamics throughout the entire film.

Large-area perovskite film fabrication can generally be divided into solution-based processing and vapor-based deposition according to precursor delivery and solidification pathways. These two routes

differ fundamentally in mass transport, phase transformation, and crystallization kinetics, thereby creating distinct film-formation environments. In solution-based processing, precursor solutions are deposited onto the substrate before being converted into crystalline perovskites through solvent evaporation, supersaturation evolution, nucleation, and crystal growth. Owing to its low processing temperature, high material utilization, and compatibility with roll-to-roll (R2R) manufacturing, solution processing remains the most extensively investigated approach for scalable perovskite fabrication. From the perspective of fluid transport and wet-film evolution, scalable solution-processing techniques can be further classified into three representative categories which are meniscus-guided coating, droplet-mediated deposition, and printing-based deposition. Meniscus-guided coating, including blade coating and slot-die coating, relies on a confined liquid bridge to continuously deposit a wet film, where film formation is governed primarily by capillary flow, viscous transport, solvent evaporation, and moving contact-line dynamics. Droplet-mediated deposition, represented by spray coating and inkjet printing, constructs the wet film through droplet generation, impact, spreading, coalescence, and subsequent drying, making crystallization particularly sensitive to droplet dynamics and local solvent redistribution. Printing-based methods, such as screen printing, flexographic printing, and gravure printing, meter precursor inks through patterned transfer processes and are especially attractive for high-throughput patterned manufacturing, although film formation is additionally influenced by rheology, ink transfer efficiency, and post-transfer solvent redistribution.

Compared with solution processing, vapor-based deposition eliminates liquid-phase transport and instead generates perovskite films through precursor vapor generation, gas-phase transport, adsorption, surface reaction, and solid-state incorporation. Depending on the precursor generation mechanism, vapor-based methods can be broadly categorized into chemical vapor deposition (CVD) and physical

vapor deposition (PVD). In CVD, volatile precursors are transported to the substrate and converted into the perovskite phase through gas-solid reactions, making film growth primarily governed by precursor transport, surface reaction, and diffusion-controlled conversion. In contrast, PVD techniques generally include thermal evaporation, sputtering, electron-beam evaporation, and pulsed laser deposition. Such techniques deposit materials through physical vapor generation under vacuum, where film growth is determined mainly by precursor flux, surface incorporation, and non-equilibrium deposition kinetics. Compared with solution processing, vapor-based routes generally offer superior control over film thickness, composition, multilayer interfaces, and process reproducibility, although they require more sophisticated equipment and tighter control of precursor stoichiometry and deposition kinetics. Although these scalable deposition technologies differ substantially in equipment configuration, precursor delivery, and processing conditions, they are fundamentally governed by the same sequence of mass transport, phase transformation, nucleation, crystal growth, and defect evolution.

A common link between the two routes is the local driving force for perovskite phase formation. In solution processing, this driving force is governed mainly by supersaturation and the associated chemical-potential difference. In vapor deposition, it depends on the chemical potentials of the arriving species and on their adsorption, reaction, diffusion, and incorporation at the substrate surface. Existing reviews have primarily discussed individual deposition technologies or summarized improvements in device performance. However, a unified understanding that links mass transport physics, crystallization kinetics, and scalable film quality across different deposition routes remains largely absent. Without such a mechanistic framework, process optimization often relies on empirical trial-and-error, and insights obtained from one deposition method are difficult to transfer to others.

In this Review, we establish a unified mechanistic framework for understanding large-area perovskite film formation across both solution-based and vapor-based deposition technologies. The fundamental principles governing mass transport, supersaturation evolution, nucleation, crystal growth, and defect formation during scalable film deposition have been discussed. Specifically, we systematically discuss representative solution-processing and vapor-based deposition methods from the perspective of their underlying film-formation mechanisms, highlighting how transport behavior and crystallization kinetics jointly determine film quality. It should be noted that the equations discussed in this work are not intended to constitute a universal quantitative model applicable to all deposition methods for perovskite film formation. The applicability and quantitative accuracy of each equation depend on the assumptions and validity range of the corresponding transport or growth regime. Rather than reviewing deposition techniques individually, we emphasize the common physical principles that govern scalable perovskite crystallization and identify the key engineering variables controlling film uniformity across different manufacturing routes. Finally, we discuss the remaining scientific and technological challenges for scalable perovskite film fabrication and outline future opportunities enabled by operando characterization, multiscale modeling, artificial-intelligence-assisted process optimization, and digital manufacturing for next-generation perovskite photovoltaics.

2 Crystallization fundamentals of solution-processed perovskite films

2.1 Wet-film hydrodynamics and thickness formation

In solution-processed perovskite films, large-area uniformity is initially established during wet-film formation. Before crystallization begins, the coupled effects of liquid flow, meniscus stability, substrate wettability, and solvent evaporation determine the thickness field, solute distribution, and

drying pathway of the precursor film. These early-stage mass transport processes provide the initial conditions for subsequent supersaturation evolution, nucleation, and crystal growth. This coupling is particularly important in meniscus-guided coating methods such as blade coating and slot-die coating, where film formation is governed by the competition among viscous entrainment, capillary forces, and evaporation. As illustrated in Fig. 1, a stable liquid bridge is formed between the coating head and the substrate. During coating, the receding meniscus continuously deposits a wet film whose thickness is primarily controlled by hydrodynamic conditions.

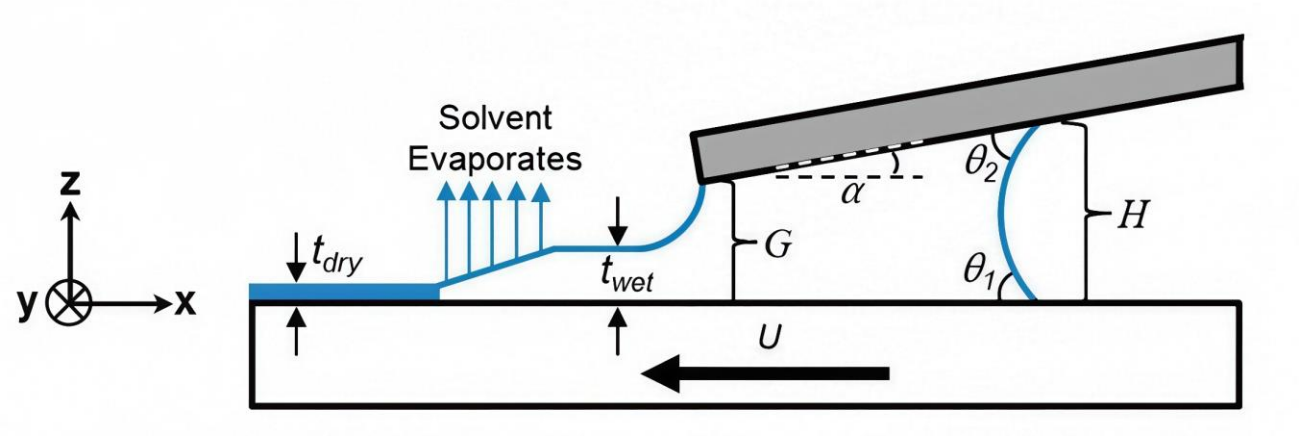

Fig. 1 Schematic illustration of a meniscus-guided coating process. Reproduced with permission from Ref. [6], © American Chemical Society 2014.

The relative importance of viscous drag and capillary restoring force can be quantified by the capillary number (Ca) [7]:

$$Ca = \frac{\mu v}{\gamma} \tag{1}$$

where μ is the solution viscosity, v is the coating speed and γ is the liquid-air surface tension. A larger capillary number corresponds to stronger viscous entrainment and generally produces a thicker wet film.

Under sufficiently high coating speeds, evaporation becomes secondary and the system enters the classical Landau–Levich–Derjaguin (LLD) regime, where wet-film thickness scales as:

$$t_{\mathrm{wet}} = 0.94\kappa^{-1}Ca^{2/3} \tag{2}$$

where $\kappa^{-1}=\sqrt{\gamma/\rho g}$ is the capillary length, ρ is the solution density, and g is the gravitational acceleration [8]. This scaling indicates that increasing coating speed or solution viscosity increases the deposited film thickness. In contrast, under low-speed conditions, solvent evaporation becomes increasingly important and the coating process gradually transitions toward an evaporation-dominated regime.

In practical large-area coating, wet-film thickness is further influenced by coating geometry and boundary conditions, including gap height, meniscus curvature, and substrate wettability. The LLD relation therefore provides a useful scaling law rather than a complete process model. The actual film thickness reflects the coupled effects of viscous entrainment, capillary confinement, evaporation, and interfacial wetting. After deposition, the wet film remains highly dynamic. Solvent evaporation induces internal flow fields, including capillary flow, Marangoni convection, concentration-driven transport, and thermal circulation. These flows continuously redistribute solutes and reshape local thickness profiles during drying. Stable flow and uniform evaporation generally favor smooth and homogeneous films, whereas hydrodynamic instabilities can generate striations, edge accumulation, coffee-ring-type nonuniformity, and local thickness fluctuations. Such effects become increasingly pronounced as coating width and process throughput increase. The final dry (solid) film thickness can be related to the wet film via mass/volume conservation using the solute/solvent volume fractions:

$$\frac{t_{\mathrm{dry}}}{t_{\mathrm{wet}}} = \frac{w_{\mathrm{solute}}/\rho_{\mathrm{solute}}}{w_{\mathrm{solute}}/\rho_{\mathrm{solute}} + w_{\mathrm{solvent}}/\rho_{\mathrm{solvent}}} \tag{3}$$

where w_{solute} and w_{solvent} are the mass fractions of solute and solvent, respectively, and ρ_{solute} and ρ_{solvent} are their corresponding densities. Therefore, wet-film hydrodynamics not only determines the initial thickness field, but also establishes the spatial distribution of solvent, solute, and

flow within the precursor film, thereby defining the boundary conditions for subsequent supersaturation evolution and crystallization.

2.2 Supersaturation evolution and nucleation kinetics

Following wet-film deposition, solvent evaporation progressively increases precursor concentration and drives the system away from thermodynamic equilibrium. The resulting supersaturation provides the fundamental driving force for nucleation and crystallization. Once local supersaturation becomes sufficiently high to overcome the nucleation free-energy barrier, stable nuclei emerge and the precursor solution transitions into rapid crystallization. The thermodynamic basis of this process can be described using classical nucleation theory (CNT) [8]. For a spherical nucleus with radius (r), the total free-energy change is given by:

$$\Delta G(r) = 4\pi r^2\gamma - \frac{4}{3}\pi r^3 \Delta G_v \tag{4}$$

$$\Delta G_v = \frac{RT \ln S}{V_m} \tag{5}$$

$$S = \frac{C}{C_s} \tag{6}$$

where γ denotes the surface free energy, ΔG_v is the magnitude of the bulk free-energy decrease per unit volume. The supersaturation S is defined by the precursor concentration C and the saturation concentration C_s. R is the ideal-gas constant, T is the absolute temperature, and V_m is the molar volume. Maximizing $\Delta G(r)$ gives the critical radius (r_c):

$$r_c = \frac{2\gamma}{\Delta G_v} \tag{7}$$

Competition between interfacial energy and bulk free-energy reduction leads to the formation of a critical nucleus radius r_c. Nuclei smaller than r_c tend to redissolve, whereas nuclei larger than r_c can grow spontaneously. Substituting r_c back into $\Delta G(r)$ gives the critical nucleation barrier ΔG^*—the energetic hurdle that must be overcome to form a stable nucleus:

$$\Delta G^* = \frac{16\pi\gamma^3}{3\Delta G_v^2} \tag{8}$$

The nucleation rate J can then be written in a Boltzmann – Arrhenius form:

$$J = A\exp\left(-\frac{\Delta G^*}{k_B T}\right) = A\exp\left[-\frac{16\pi\gamma^3 V_m^2}{3k_B R^2 T^3 (\ln S)^2}\right] \tag{9}$$

where A is a kinetic prefactor and k_B is the Boltzmann constant.

Although CNT provides a useful thermodynamic framework, nucleation in scalable coating processes is rarely spatially uniform. In practice, nucleation is strongly influenced by substrate wettability, local evaporation rate, surface energy, interfacial defects, and flow-induced solute redistribution. As a result, supersaturation evolution should be understood as both a temporal and spatial process. The temporal pathway determines when the system enters the nucleation-permitted regime, whereas the spatial pathway determines where nucleation occurs first and whether crystallization remains synchronized across the substrate. This coupling between supersaturation dynamics and spatial transport is particularly important in large-area coating, where small variations in evaporation or wetting can amplify into significant nonuniformities in nucleus density and grain structure [9].

The overall crystallization process can be conceptually described using the LaMer model (Fig. 2(a)) [10–13], which divides film formation into three stages: precursor accumulation, burst nucleation, and crystal growth. During solvent evaporation, precursor concentration initially increases without significant nucleation. Once the concentration reaches a critical supersaturation, rapid nucleation occurs over a short time window. Subsequent crystallization is then dominated primarily by crystal growth rather than by continued nucleation. This framework directly links drying kinetics with film microstructure (Fig. 2(b)). Slow solvent evaporation generally produces lower supersaturation and lower nucleus density, favoring larger grains but potentially poorer coverage uniformity. In contrast,

rapid solvent extraction induces stronger nucleation bursts and higher nucleus densities, which improve coverage synchronization but may also increase grain-boundary density.

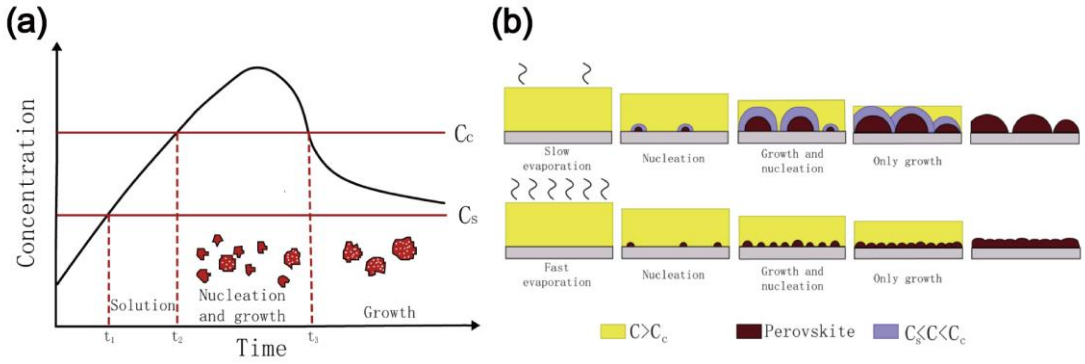

Fig. 2 (a) LaMer model describing nucleation and growth during perovskite film formation. (b) Schematic illustration of how solvent evaporation rate alters the supersaturation pathway and nucleus density during perovskite film formation.

2.3 Crystal growth, grain competition, and microstructure evolution

After stable nuclei form, crystallization progressively transitions from nucleation-dominated behavior to growth-dominated behavior. The final microstructure is therefore determined not only by initial nucleus density, but also by subsequent crystal growth, grain competition, and coarsening. Crystal growth involves two coupled processes: transport of precursor species to the crystal surface and their subsequent incorporation into the lattice. Depending on which step is slower, growth may become diffusion-limited or interface-limited. In scalable solution processing, growth kinetics are jointly governed by solvent evaporation, solute transport, and surface incorporation dynamics.

The commonly used strategy of “fast nucleation and slow growth” originates directly from this competition. Rapid early-stage nucleation establishes sufficient nucleus density and coverage uniformity, whereas slower subsequent growth favors improved crystallinity and reduced structural disorder. As crystallization proceeds, neighboring grains compete for both solute supply and available growth space. Low nucleus density generally enables larger grains because each nucleus occupies a

larger capture zone. However, insufficient nucleus density may also produce discontinuous coverage and void formation. Conversely, high nucleus density improves coverage synchronization but accelerates grain impingement and restricts final grain size. Therefore, final grain structure is determined by the coupled interplay among nucleus density, solute redistribution, and growth competition.

After formation of a continuous polycrystalline network, further microstructural evolution often occurs through grain coarsening and Ostwald ripening. Smaller grains possess higher interfacial energy and gradually dissolve, while larger grains continue to grow. This process reduces total grain-boundary area and can suppress some grain-boundary-related defects. Importantly, many crystallization additives and annealing strategies influence final grain size not primarily by changing initial nucleation density, but by modifying grain-boundary mobility and coarsening kinetics during later stages of film evolution. Consequently, the ultimate objective of crystallization engineering is not simply to maximize grain size, but to achieve an optimized balance among coverage uniformity, grain structure, defect density, and large-area reproducibility.

2.4 Non-equilibrium crystallization and transport-field regulation

Perovskite film formation rarely occurs under near-equilibrium conditions. Instead, scalable solution processing is typically governed by strongly non-equilibrium transport fields generated by gas flow, temperature gradients, rapid solvent extraction, and dynamic substrate motion. These external fields continuously reorganize local heat and mass transfer, thereby modifying supersaturation evolution, nucleation timing, and subsequent crystal growth. In this Review, non-equilibrium crystallization describes film formation in which solvent removal, precursor delivery, or thermal processing proceeds faster than structural relaxation. This imbalance can preserve kinetically trapped

intermediates or metastable phases before their conversion into the final thermodynamically favored perovskite phase.

Gas-assisted drying provides a representative example. Rapid gas quenching accelerates solvent extraction and drives the wet film rapidly into a high-supersaturation regime, producing dense early-stage nucleation. In contrast, slow natural drying delays supersaturation buildup and promotes growth-dominant crystallization pathways. Gas flow therefore acts not merely as a drying accelerator, but as a regulator that fundamentally changes the nucleation–growth balance during film formation. Temperature gradients provide another important non-equilibrium control parameter. Localized heating modifies both evaporation kinetics and surface-tension distributions, thereby inducing Marangoni flow within the wet film. Competition among capillary flow, thermal convection, and evaporation-driven transport strongly influences solute redistribution and crystallization uniformity. Appropriate thermal regulation can suppress coffee-ring-type accumulation and improve film homogeneity, whereas excessive heating may induce premature crystallization and destabilize coating uniformity.

More generally, non-equilibrium processing modifies the relative durations and spatial distributions of nucleation-dominant and growth-dominant stages. External transport fields reshape when and where critical supersaturation is reached, thereby redefining the initial conditions for later microstructure evolution. Importantly, non-equilibrium processing does not necessarily eliminate intermediate phases. Instead, it often compresses the formation and conversion time windows of these intermediates. The key challenge is therefore not whether intermediate phases form, but whether their transformation into the target perovskite phase occurs rapidly and uniformly throughout the coated area. From a manufacturing perspective, successful non-equilibrium crystallization control requires

coordinated matching between external transport conditions and intrinsic crystallization time scales. Parameters such as gas velocity, substrate temperature, coating speed, wet-film thickness, and solvent volatility must therefore be optimized collectively rather than independently. When these coupled processes are properly synchronized, non-equilibrium processing becomes a powerful strategy for regulating large-area crystallization and achieving highly uniform perovskite films.

3 Solution-processed scalable deposition methods and crystallization regulation

3.1 Meniscus-guided coating methods

Meniscus-guided coating represents one of the most important scalable process platforms for large-area perovskite film fabrication. In these methods, a confined liquid meniscus continuously deposits a precursor wet film onto a moving substrate, enabling efficient material utilization and compatibility with continuous R2R manufacturing. Blade coating and slot-die coating are the two most representative implementations of this strategy and have been extensively explored for scalable perovskite photovoltaics.

3.1.1 Blade coating

Blade coating is among the most widely studied and practically relevant approaches for scalable perovskite film deposition. As shown in Fig. 3(a), precursor solution is confined between a coating blade and the substrate and continuously spread into a wet film during relative substrate motion. Compared with spin coating, blade coating significantly reduces precursor consumption, improves material utilization, and provides a mechanically simple and scalable process configuration. In addition, its relatively broad processing window and compatibility with different ink formulations make it highly

attractive for process optimization and manufacturing scale-up. From the perspective of crystallization control, the central challenge of blade coating lies in maintaining synchronized wet-film evolution and solvent extraction across large areas. Unlike spin coating, where rapid centrifugal thinning shortens the wet-film lifetime, blade-coated films typically remain in a liquid state for much longer periods. As coating width increases, local variations in coating speed, gap height, substrate wettability, ink delivery, and evaporation rate can progressively amplify into macroscopic thickness gradients and spatially nonuniform supersaturation fields. These heterogeneities subsequently induce asynchronous nucleation and uneven crystal growth, ultimately degrading film uniformity and module reproducibility. Consequently, solvent-removal kinetics become a critical control parameter in scalable blade coating. In many cases, natural evaporation alone is insufficient to drive rapid and spatially synchronized crystallization. Instead, accelerated solvent extraction is commonly introduced to regulate supersaturation buildup and promote more uniform nucleation across the wet film.

Substrate heating represents one widely used strategy for enhancing solvent evaporation and accelerating film densification and crystallization. Elevated substrate temperatures increase local evaporation flux and shorten the wet-film residence time. However, under continuous large-area operation, maintaining a spatially uniform temperature field across a moving substrate remains challenging. Nonuniform heating can introduce local variations in supersaturation evolution and thereby destabilize crystallization synchronization. Gas-assisted drying provides a second important approach for non-equilibrium crystallization control. As illustrated in Fig. 3(b), a directed gas flow enhances convective mass transfer above the wet film and continuously removes solvent vapor from the boundary layer. This process accelerates solvent extraction and helps suppress edge-to-center drying asymmetry during large-area coating. In blade coating, parameters such as gas-flow velocity,

nozzle geometry, flow-field uniformity, and nozzle-to-substrate distance directly influence local heat and mass transfer and therefore strongly affect supersaturation evolution and nucleation behavior.

Vacuum-assisted processing offers another route for rapid solvent removal. As shown in Fig. 3(c), vacuum flash treatment lowers the effective solvent boiling point and extracts solvent within a short time window, thereby substantially reducing wet-film residence time and promoting more synchronized nucleation. In practical manufacturing systems, however, implementation of vacuum-assisted drying often requires careful integration of pumping capacity, thermal management, and solvent-vapor recovery.

Beyond external drying regulation, crystallization pathways can also be tailored through precursor chemistry. Antisolvent extraction, solvent engineering, and additive incorporation are frequently employed to modify solvent volatility, intermediate-phase formation, and supersaturation kinetics [14]. These strategies provide additional flexibility for regulating nucleation density, grain growth, and film morphology during scalable coating. Because these coating, drying, and formulation parameters are strongly coupled, data-driven optimization has recently been introduced to guide blade-coating process design; for example, machine-learning-guided analysis of blade-coating parameters has been used to screen high-dimensional process windows and improve device reproducibility [15].

Practical progress in blade coating has therefore relied on the coordinated control of crystallization kinetics, drying-induced solute transport, and precursor coordination chemistry. Li et al. [16] used in situ grazing-incidence wide-angle X-ray scattering and real-time optical microscopy to determine how substrate temperature affects phase evolution during blade coating. At 25 °C, the dimethyl sulfoxide (DMSO)/γ-butyrolactone (GBL) wet film followed an intermediate-phase-mediated pathway and crystallized during subsequent annealing. This pathway produced needle-like domains and incomplete

surface coverage. When the substrate temperature was increased to 150 °C, rapid solvent removal suppressed the long-lived intermediate pathway and enabled methylammonium lead iodide ($MAPbI_3$) to crystallize within seconds. The microscopy sequences in Fig. 3(d) show the corresponding change from one-dimensional needle-like growth to rapid radial growth of spherulitic domains. This direct-crystallization route produced a denser and more continuous film. The resulting devices reached PCEs of 18.74% for 0.09 cm^2 cells and 17.06% for 1 cm^2 cells. Deng et al. [17] addressed a different limitation associated with lateral solute redistribution during drying. Fig. 3(e) summarizes the proposed transport mechanism. Without an additive, solvent evaporation drove the precursor solution toward growing perovskite islands and depleted the regions between them, resulting in gaps and discontinuous coverage. The addition of a small amount of L-α-phosphatidylcholine (LP) changed the surface-tension gradient within the wet film. The resulting Marangoni flow opposed the original direction of solute transport and reduced accumulation around the perovskite islands. The macroscopic comparison in Fig. 3(f) shows the corresponding improvement in film continuity after LP addition. The films were deposited in air at a coating rate of 180 $m \cdot h^{-1}$. The resulting modules achieved stabilized efficiencies of 15.3% and 14.6% for aperture areas of 33.0 and 57.2 cm^2, respectively. Bu et al. [18] extended crystallization control to larger-area formamidinium–caesium perovskite films. Methylammonium chloride was introduced into an N-methyl-2-pyrrolidone (NMP)/N,N-dimethylformamide (DMF) precursor system to regulate competition between perovskite–DMF intermediates and PbI_2-NMP adducts. This modification suppressed the formation of the undesirable δ-phase and promoted an α-phase intermediate during self-drying. Subsequent annealing completed its conversion into the target α-phase perovskite. Fig. 3(g) presents the resulting fully blade-coated 15 × 15 cm^2 sub-module and its current density-voltage characteristic. The sub-module contained 21

series-connected cells, had an aperture area of 205 cm^2, and reached a PCE of 15.3%. Collectively, these studies demonstrate that the scalability of blade coating depends not only on coating mechanics but, more fundamentally, on precise regulation of wet-film transport, supersaturation evolution, and crystallization synchronization across large areas.

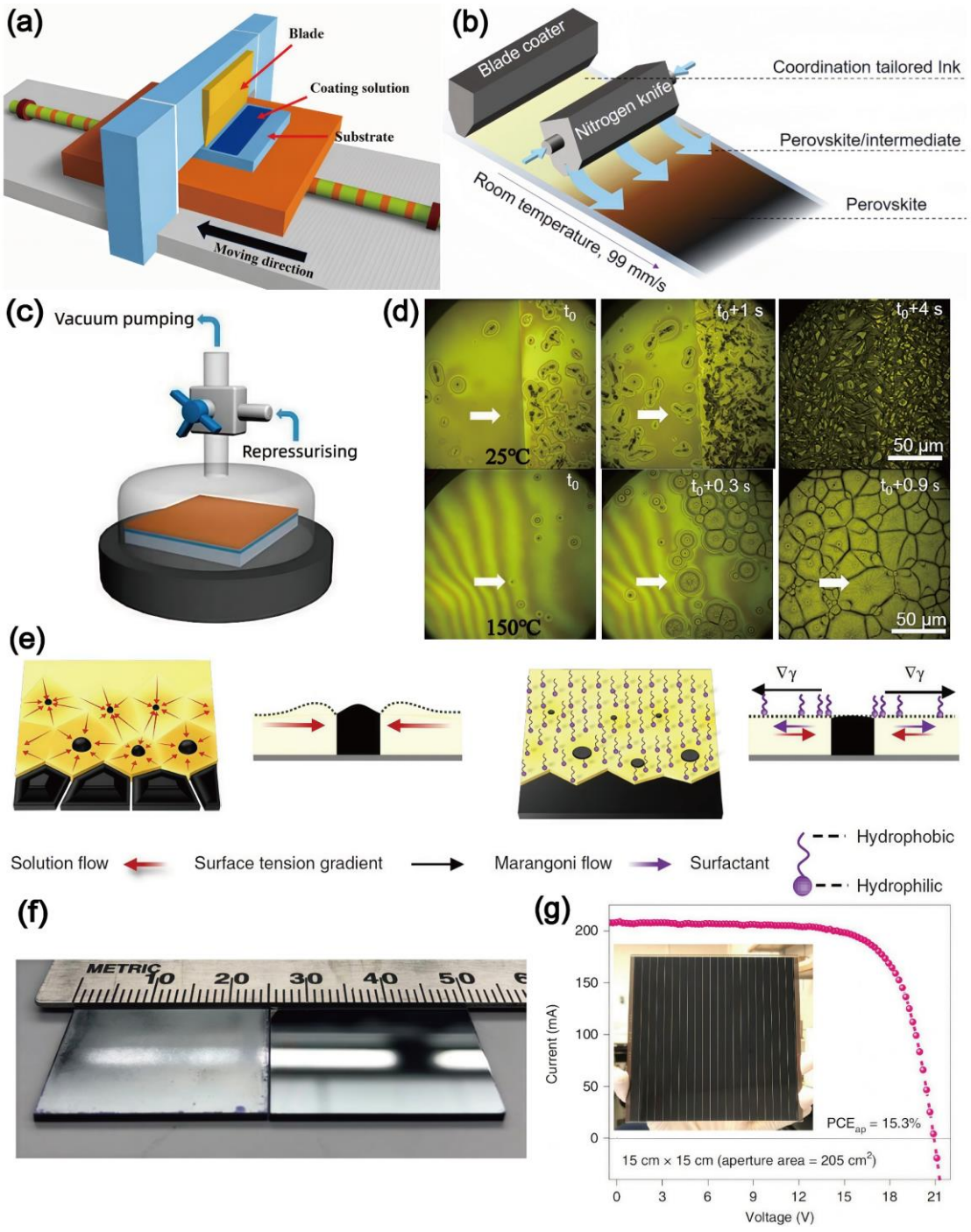

Fig. 3 (a) Schematic illustration of the blade-coating process. Reproduced from Ref. [19] under CC

BY 4.0, © The Author(s) 2022. (b) Schematic illustration of gas-quenching-assisted blade coating. Reproduced with permission from Ref. [20], © The Authors 2019. (c) Schematic illustration of a vacuum-flash process. Reproduced from Ref. [21] under CC BY 4.0, © The Author(s) 2022. (d) Real-time optical microscopy images of DMSO/GBL films processed at 25 and 150 °C, showing needle-like crystal growth and rapid radial growth of spherulitic domains, respectively. Reproduced with permission from Ref. [16], © Elsevier Inc. 2018. (e) Schematics of evaporation-induced solute transport without surfactant and the opposing Marangoni flow induced by LP surfactant. (f) Photographs of blade-coated perovskite films prepared without and with LP, showing improved film continuity after LP addition. Reproduced with permission from Ref. [17], © Macmillan Publishers Limited, part of Springer Nature 2018. (g) Photograph and current–voltage characteristic of a fully blade-coated 15 × 15 cm^2 perovskite solar sub-module with an aperture area of 205 cm^2. Reproduced with permission from Ref. [18], © Springer Nature Limited 2022.

3.1.2 Slot-die coating

Slot-die coating is a pre-metered meniscus-guided coating technique widely regarded as one of the most promising manufacturing routes for large-area perovskite photovoltaics. In this process, precursor ink is continuously delivered from a reservoir through a manifold and narrow slit inside the die head, forming a confined liquid bead between the die lip and the moving substrate as shown in Fig. 4(a). As the substrate translates relative to the die, the liquid bead continuously deposits a wet film with controlled thickness. Compared with blade coating, slot-die coating provides more precise fluid metering and better compatibility with automated R2R manufacturing. Because precursor delivery is regulated mechanically through the die manifold and pumping system, slot-die coating generally offers improved thickness reproducibility, higher process stability, and greater scalability for continuous

production. From the perspective of crystallization control, the key challenge in slot-die coating is maintaining stable and spatially uniform wet-film formation across the entire coating width. Stable coating requires the liquid bead to remain continuously pinned between the die and substrate without flooding, air entrainment, bead breakup, or wetting failure. In practice, bead stability is governed by the coupled effects of volumetric flow rate, coating speed, die-to-substrate gap, ink rheology, and interfacial wetting behavior. Under quasi-steady conditions, the deposited wet-film thickness approximately scales with the ratio between precursor flow rate and substrate translation speed. As coating width increases, cross-web flow uniformity becomes increasingly important. Small perturbations arising from pump pulsation, nonuniform pressure distribution inside the manifold, tubing fluctuations, or local wetting heterogeneity can progressively amplify into thickness gradients, streak defects, or local bead rupture. These hydrodynamic nonuniformities subsequently generate spatial variations in solvent evaporation and supersaturation evolution, ultimately leading to asynchronous nucleation and nonuniform crystallization over large areas. Consequently, suppression of flow instability and maintenance of bead uniformity are central requirements for scalable slot-die processing.

Similar to blade coating, solvent-removal kinetics strongly influence crystallization synchronization during slot-die coating. Because wet films deposited by slot-die coating often possess relatively long residence times, natural evaporation alone is generally insufficient to achieve rapid and uniform supersaturation buildup. Additional non-equilibrium drying strategies, including substrate heating, gas-assisted drying, and vacuum-flash treatment, are therefore widely employed to accelerate solvent extraction and regulate crystallization pathways. These approaches not only shorten drying time, but more importantly reshape local heat and mass transfer during the transition from liquid

precursor to crystalline perovskite. Recent studies illustrate how slot-die coating can be improved by controlling wet-film formation and its subsequent conversion into the perovskite phase. Li et al. [22] adjusted the rheological properties of a 2-methoxyethanol-based formamidinium lead iodide ($FAPbI_3$) ink by adding low-viscosity acetonitrile (ACN). Without ACN, the wet film exhibited pronounced ribbing. These thickness variations remained visible after annealing. Increasing the ACN content to 46 vol% reduced the dynamic viscosity, whereas the surface tension changed only slightly. The lower viscosity promoted wet-film leveling and suppressed ribbing, as shown by the comparison in Fig. 4(b). The optimized ink produced homogeneous films after gas quenching and annealing. It enabled a certified steady-state PCE of 22.3% for small-area cells and a PCE of 17.1% for a mini-module with an active area of 12.7 cm^2. Geistert et al. [23] focused on the spatial control of gas quenching. They used a charge-coupled device camera to track the drying front relative to the center line of the gas jet. When the drying front remained behind the center line, post-drying caused uncontrolled solvent removal and pinhole formation. When it moved ahead of the center line, pre-drying induced premature nucleation and reduced the grain size. The most uniform morphology was obtained under instant-drying conditions, in which the drying front approached the center line (Fig. 4(c)). Adjustments to the nozzle geometry and gas flow suppressed gas backflow and extended the instant-drying region across the substrate. Under these conditions, a 50 × 50 mm^2 mini-module reached a PCE of 17.2% over an active area of 1,296 mm^2, with only a 5% relative upscaling loss (Fig. 4(d)). Zimmermann et al. [24] used sequential slot-die coating to separate inorganic precursor deposition from perovskite formation. A CsI-PbI_2 layer was first deposited and vacuum-dried to retain a porous CsI-PbI_2(DMSO) intermediate. Organic salts were then applied in a second slot-die pass, followed by thermal annealing to complete the conversion (Fig. 4(e)). The porous intermediate facilitated the penetration of organic

cations into the precursor layer. In contrast, dense crystalline PbI_2 hindered complete conversion. This process produced uniform perovskite layers over 5 × 10 cm^2 substrates. The resulting devices reached PCEs of 19% for small-area cells and 15.2% for mini-modules with an aperture area of 12 cm^2.

Overall, slot-die coating highlights the importance of coupling flow-field engineering with crystallization regulation during scalable perovskite manufacturing. Achieving stable large-area deposition requires not only precise precursor delivery but also synchronized solvent extraction and spatially uniform supersaturation evolution throughout the coating process.

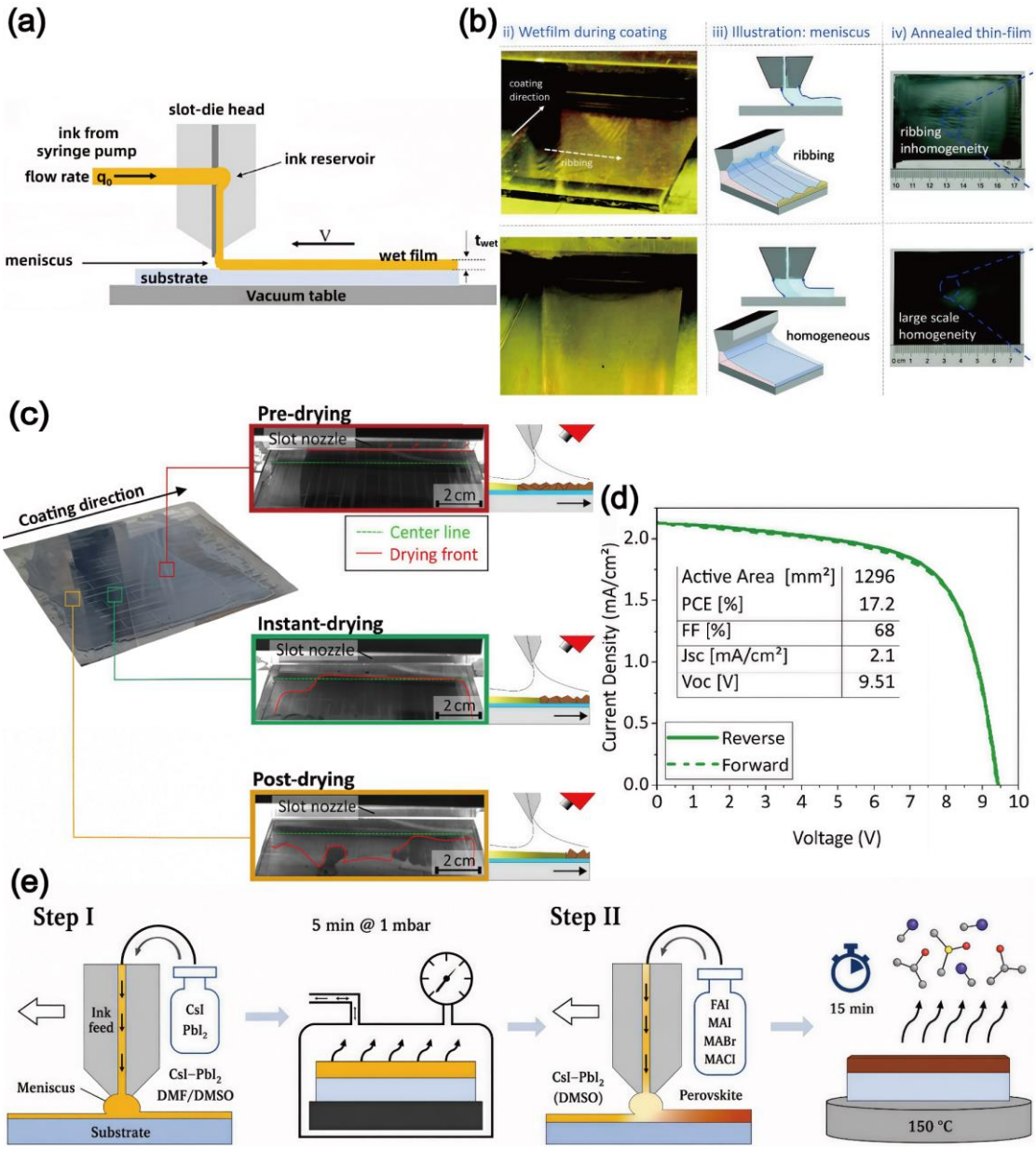

Fig. 4 (a) Schematic illustration of slot-die coating, showing pre-metered ink delivery and wet-film formation. Reproduced with permission from Ref. [25], © Wiley-VCH GmbH 2024. (b) Wet-film appearance, meniscus behavior, and annealed films obtained from $FAPbI_3$ inks containing 0 and 46 vol% ACN, showing the suppression of ribbing after ink optimization. Reproduced from Ref. [22] under CC BY, © The Author(s) 2023. (c) In situ observation of pre-, instant-, and post-drying regimes, as defined by the position of the drying front relative to the center line of the gas jet. (d) Current density-voltage (J-V) characteristics of a 50 × 50 mm^2 mini-module with an active area of 1,296 mm^2 and a PCE of 17.2%. Reproduced with permission from Ref. [23], © The Authors 2023. (e) Schematic illustration of sequential slot-die coating, including inorganic precursor deposition, vacuum drying, organic-salt deposition, and thermal conversion into the perovskite phase. Reproduced with permission from Ref. [24], © Wiley-VCH GmbH 2021.

3.2 Droplet-mediated deposition

Unlike meniscus-guided coating, which relies on a continuous liquid film and a moving contact line, droplet-mediated deposition delivers precursor ink discretely and without direct mechanical contact. In these methods, the precursor solution is first broken into micron-scale droplets, which subsequently travel through the gas phase, impact the substrate, spread, and merge with neighboring droplets. A continuous wet film is then gradually assembled from these individual droplets before undergoing solvent evaporation and crystallization to form a perovskite layer. Since the film formation originates from discrete droplet events rather than from a continuous liquid bridge, the uniformity of droplet spreading and coalescence becomes the key prerequisite for synchronized crystallization. Consequently, understanding droplet impact dynamics is essential for rationally controlling wet-film formation, local supersaturation evolution, and final film morphology in droplet-mediated deposition

processes.

At the process level, droplet-mediated deposition is governed by the coupled interactions among nozzle characteristics, ink fluid properties, and substrate conditions. To quantitatively describe these coupled effects, droplet behavior is commonly analyzed using several dimensionless hydrodynamic parameters, including the Weber number (We), Reynolds number (Re), and Ohnesorge number (Oh), together with its inverse form (Z) [8]:

$$We = \frac{\rho U^2 D}{\gamma} \tag{10}$$

$$Re = \frac{\rho U D}{\mu} \tag{11}$$

$$Oh = \frac{1}{Z} = \frac{\mu}{\sqrt{\rho \gamma D}} = \frac{\sqrt{We}}{Re} \tag{12}$$

where ρ is the ink density, U is the droplet impact velocity, D is the characteristic droplet length scale (often the diameter), γ is the surface tension, and μ is the dynamic viscosity.

These dimensionless numbers provide a unified framework for evaluating whether droplets can be generated, transported, spread, and merged stably before crystallization begins. Physically, the Weber number describes the competition between inertial and capillary forces during droplet impact. Larger We values generally enhance droplet spreading but also increase the probability of splashing and instability. The Reynolds number compares inertial and viscous forces and strongly influences spreading dynamics and coalescence behavior. The Ohnesorge number characterizes the extent to which viscous dissipation suppresses inertial-capillary oscillation and is widely used to evaluate droplet printability and jetting stability [26,27].

In practical droplet-mediated deposition, stable processing typically requires these parameters to fall within an appropriate operating window, for example,$1 < Z < 10, We > 4$, and $We^{1/2} Re^{1/4} \leq 50$ [28]. If viscosity is excessively high (Z too small), stable droplet atomization or ejection becomes

difficult. Conversely, if inertial forces become too dominant (high We and Re), splashing, satellite droplets, and irregular wetting are more likely to occur. These hydrodynamic instabilities directly translate into local thickness fluctuations and nonuniform crystallization during film drying.

Importantly, these dimensionless criteria also establish direct links between process parameters and film formation. Droplet velocity is influenced by driving pressure, electric-field strength, nozzle design, and nozzle-to-substrate distance. Ink formulation determines viscosity, density, and surface tension through solvent composition, precursor concentration, and additive chemistry. Meanwhile, substrate temperature and wettability regulate droplet spreading, contact-line motion, and solvent evaporation kinetics. Together, these parameters define whether droplets can coalesce into a spatially uniform wet film prior to crystallization.

Once a continuous precursor film is established, crystallization generally follows pathways similar to those described for meniscus-guided coating, including solvent evaporation, supersaturation buildup, nucleation, and crystal growth. However, compared with continuous coating methods, droplet-mediated deposition introduces additional spatial heterogeneity arising from droplet overlap, local thickness fluctuations, and edge-concentrated solute redistribution during drying. Contact-line pinning and evaporation-driven capillary flow can further induce local concentration accumulation and coffee-ring-type nonuniformity. As a result, droplet-mediated deposition is particularly sensitive to the coupling between drying kinetics and crystallization kinetics. In practical processing, substrate heating, gas-assisted drying, solvent engineering, and additive incorporation are frequently employed to regulate local supersaturation evolution and suppress drying-induced nonuniformity. Through coordinated control of droplet dynamics, evaporation behavior, and crystallization pathways, droplet-mediated methods can achieve increasingly uniform large-area perovskite films despite their

intrinsically discrete deposition nature.

3.2.1 Spray coating

Spray coating is a representative droplet-mediated deposition method in which precursor solution is atomized into micron-scale droplets and transported to the substrate through a spray plume. During the deposition process, droplets undergo spreading, coalescence, partial solvent evaporation, and eventual assembly into a continuous wet film, which subsequently dries and crystallizes into a perovskite layer. Compared with meniscus-guided coating, spray coating eliminates direct liquid–substrate contact during deposition and therefore offers greater flexibility for large-area, textured, or nonplanar substrates. It is also highly compatible with continuous R2R manufacturing and high-throughput processing. From the perspective of film crystallization control, the central challenge of spray coating lies in synchronizing droplet coalescence and solvent evaporation across the deposited area. Since the film formation originates from numerous discrete droplets rather than from a continuous liquid bridge, local thickness fluctuations, uneven drying, and droplet-overlap heterogeneity can readily generate spatially nonuniform supersaturation fields. Consequently, the atomization process and droplet transport dynamics strongly influence the subsequent crystallization pathway and final film morphology.

As illustrated in Fig. 5(a-c), spray coating can be categorized according to the atomization mechanism into ultrasonic atomization, pneumatic atomization, and electrostatic atomization (electrospray). Ultrasonic atomization uses high-frequency vibration to generate relatively uniform fine droplets, enabling improved control over droplet loading and spray distribution. Pneumatic atomization employs compressed gas to shear the liquid stream into droplets and is attractive for scalable manufacturing because of its structural simplicity and high throughput, although droplet-size

fluctuations are generally larger and therefore require tighter process control. Electrospray utilizes high electric fields to generate charged microdroplets, enabling improved regulation of droplet size and flux through electrohydrodynamic effects [29].

The overall spray-coating process is governed by coupled interactions among ink formulation, atomization dynamics, droplet transport, substrate wetting, and solvent evaporation. Ink composition determines viscosity, surface tension, and volatility, which collectively influence droplet generation and spreading behavior. Atomization conditions, including nozzle geometry, ultrasonic power, gas pressure, and applied voltage, regulate droplet-size distribution and droplet flux. Meanwhile, spray distance and carrier-gas flow determine flight time and in-flight evaporation, thereby affecting droplet impact state and local solvent content upon substrate arrival. On the substrate side, temperature and wettability further control droplet spreading, coalescence kinetics, and wet-film lifetime.

For scalable spray coating, the deposited wet-film thickness can be approximately expressed as:

$$t_{\mathrm{wet}} \approx \frac{\eta_{\mathrm{dep}} Q}{us} \tag{13}$$

where η_{dep} is the deposition efficiency (accounting for overspray, rebound, and other losses), Q is the volumetric flow rate, u is the scan speed, and s is the scan-line spacing. This relationship highlights that film thickness is jointly determined by droplet delivery and lateral scan overlap during deposition. Importantly, however, achieving thickness uniformity alone does not guarantee synchronized crystallization. In spray-coated films, local variations in droplet density and coalescence often produce heterogeneous drying pathways. Slow local drying can induce capillary-driven solute redistribution and coffee-ring-type accumulation, while incomplete droplet merging may leave pinholes or rough surface features. These effects become increasingly pronounced during scale-up because spatial nonuniformities in gas flow, substrate temperature, and solvent-vapor accumulation

can progressively desynchronize nucleation and crystal growth across the coating area. Consequently, scalable spray coating generally requires active regulation of non-equilibrium drying conditions. Substrate heating and gas-assisted drying are widely employed to accelerate solvent removal and suppress local solvent accumulation. These approaches are frequently combined with solvent engineering and co-solvent/additive design to regulate intermediate-phase formation and evaporation trajectories, thereby improving droplet coalescence and suppressing coffee-ring formation, pinholes, and crystallization heterogeneity.

Recent progress in spray coating has shifted attention from atomization alone to the chemical environment within each droplet. Feng et al. [30] developed a localized high-concentration (LHC) precursor strategy by combining strong- and weak-ligand solvents. The weak-ligand component restricted the diffusion of FA^+ and maintained close association between A-site cations and lead-iodide complexes. This promoted confined pre-nucleation within the droplets and suppressed the competing crystallization pathways observed in the ligand-rich state (Fig. 5(d)). The precursor could therefore convert directly into the α-phase after deposition, with fewer intermediate phases and a more uniform crystal orientation. The strategy produced continuous perovskite films over 10 × 10 cm^2 substrates. A 5 × 5 cm^2 mini-module with an active area of 14 cm^2 reached a PCE of 22.5%, as shown in Fig. 5(e). Small-area devices achieved a PCE of 25.5%, with a certified value of 25.2%. Composition can also be adjusted after the initial spray-coated film has formed. Heo et al. [31] first deposited $CsPbI_2Br$ and then applied a $CsPbI_3$ solution using an orthogonal spray process. The second deposition produced an iodine-rich $CsPbI_{3-x}Br_x$ region near the film surface. Fig. 5(f) shows that the Br/Pb ratio increased gradually with profiling depth. Extending the second spray step drove the iodine-rich region further into the underlying film, while spray times above 15 s produced a $CsPbI_3$-rich surface layer. The

resulting composition gradient broadened light absorption and modified the internal electric-field distribution. It also improved charge separation and collection. Devices with an aperture area of 0.096 cm^2 reached a PCE of 16.81%. A seven-cell submodule with an aperture area of 112 cm^2 achieved a PCE of 13.82%. During an ISOS-L-1 light-soaking test, the unencapsulated submodule showed less than 10% degradation after 1,000 h under continuous one-sun illumination at open circuit in N_2 at room temperature.

An electric field provides another means of regulating crystallization during droplet deposition. Niu et al. [32] used electrospray to prepare wide-bandgap mixed-halide perovskite films. In the spin-coated film, the absorption edge shifted from approximately 710 to 750 nm during annealing, indicating gradual evolution from a bromide-rich composition toward the final iodide-bromide mixture (Fig. 5(g)). By contrast, the electrosprayed film already showed an absorption edge near 750 nm before extended annealing, and little subsequent change was observed (Fig. 5(h)). This result indicates that the mixed-halide composition formed much earlier during electrospray deposition. The authors attributed the accelerated process to electric polarization and Coulomb fission of the charged droplets. These effects promoted solvent removal and reduced the difference between the crystallization rates of iodide- and bromide-rich species. The resulting devices reached PCEs of 21.44% for an aperture area of 0.08 cm^2 and 20.77% for 1.0 cm^2. Unencapsulated p-i-n devices also retained 90% of their initial efficiency after 1,550 h of stabilized power-output tracking under one-sun white-LED illumination in N_2 at room temperature. Collectively, these studies demonstrate that spray coating is fundamentally a coupled problem of droplet dynamics, solvent transport, and non-equilibrium crystallization. Achieving scalable high-quality perovskite films requires not only stable atomization and droplet delivery but also synchronized drying and supersaturation evolution throughout the entire

deposition area.

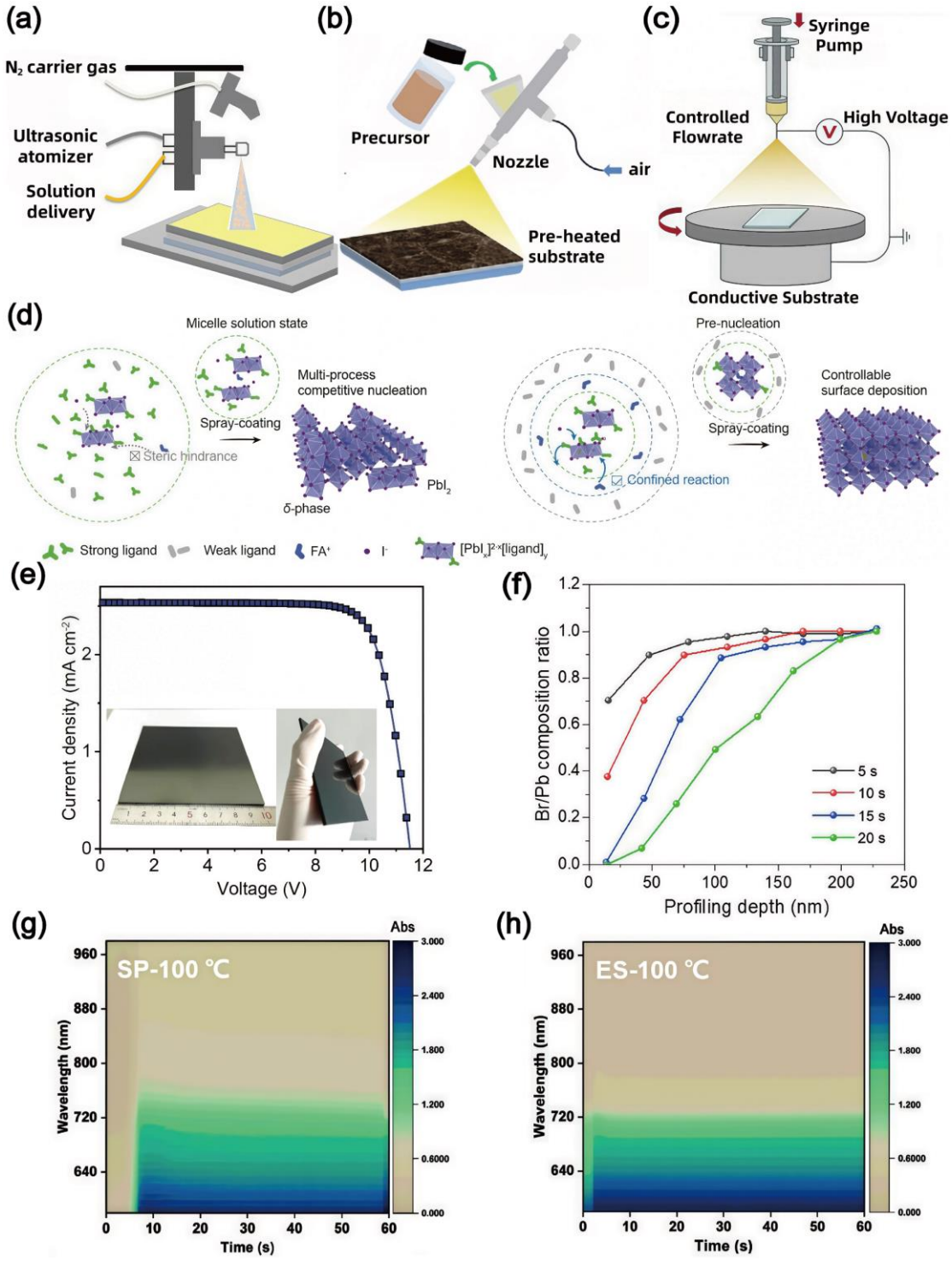

Fig. 5 (a) Schematic illustration of ultrasonic spray coating. Reproduced with permission from Ref. [33], © American Chemical Society 2020. (b) Schematic illustration of pneumatic spray coating using air-assisted atomization and a preheated substrate. Reproduced with permission from Ref. [34], © The

Royal Society of Chemistry 2016. (c) Schematic illustration of electrospray coating under an applied electric field. Reproduced with permission from Ref. [32], © Wiley-VCH GmbH 2023. (d) Comparison of the ligand-rich precursor state and the localized high-concentration strategy during spray coating, showing competitive nucleation and confined pre-nucleation, respectively. (e) J-V characteristic of a 5 × 5 cm^2 mini-module; the inset shows a 10 × 10 cm^2 spray-coated perovskite film. Reproduced with permission from Ref. [30], © Elsevier Inc. 2025. (f) Br/Pb composition profiles of graded $CsPbI_{3-x}Br_x$ films prepared using different $CsPbI_3$ spray times. Reproduced with permission from Ref. [31], © Elsevier Inc. 2020. (g, h) In situ time-resolved ultraviolet–visible absorption contour plots of spin-coated and electrosprayed mixed-halide perovskite films during annealing at 100 °C, respectively. Reproduced with permission from Ref. [32], © Wiley-VCH GmbH 2023.

3.2.2 Inkjet printing

Inkjet printing differs fundamentally from spray coating in both deposition philosophy and crystallization regulation. Whereas spray coating rapidly covers a substrate through the overlap of atomized droplets, inkjet printing deposits individual droplets with digitally programmed spatial positioning, enabling mask-free and highly localized material deposition. This digital addressability allows precise patterning with minimal material waste, but also imposes substantially stricter requirements on droplet reproducibility, ink stability, and synchronization between deposition and crystallization.

In a typical inkjet-printing process, individual precursor droplets are generated at the nozzle, transported through the gas phase with partial solvent evaporation, deposited onto the substrate, and subsequently spread and merge with neighboring droplets. Local wet films are therefore assembled sequentially from discrete droplets before undergoing solvent evaporation, supersaturation buildup,

nucleation, and crystal growth to form the final perovskite layer. Compared with continuous coating methods, film formation in inkjet printing is intrinsically intermittent and spatially discretized, making the coupling between droplet coalescence and crystallization particularly important.

As illustrated in Fig. 6(a-c), inkjet printing is commonly categorized into continuous inkjet (CIJ) and drop-on-demand (DOD) modes. CIJ continuously generates droplets and uses electrostatic deflection for pattern control, enabling relatively high throughput but requiring more complex recirculation and droplet-management systems. In contrast, DOD printing ejects droplets only when triggered, resulting in higher material utilization and improved positional accuracy. Consequently, DOD is more widely adopted for patterned functional films and perovskite optoelectronics. Depending on the actuation mechanism, DOD systems can be further divided into piezoelectric and thermal-bubble printing.

Inkjet printing shares many hydrodynamic features with other droplet-mediated deposition methods, including the importance of droplet size, spreading behavior, and substrate wetting. However, because film formation originates from individually positioned droplets, the final film thickness and continuity are additionally determined by the spatial arrangement of droplets during deposition. Under simplified conditions, the wet-film thickness can be approximately expressed as:

$$t_{\mathrm{wet}} \approx \frac{N_{\mathrm{pass}} V_d}{p_x p_y} \tag{14}$$

where N_{pass} is the number of passes, V_d is the droplet volume, and p_x and p_y are the drop pitch in the x- and y-directions, respectively. This relationship highlights an important distinction between inkjet printing and spray coating. In spray coating, film formation is primarily governed by statistical droplet overlap within a spray plume. In inkjet printing, by contrast, local film morphology is directly

programmed through droplet placement density and deposition sequence. As a result, crystallization uniformity depends strongly on whether neighboring droplets can coalesce and dry synchronously before substantial local supersaturation differences develop.The primary scale-up challenge in inkjet printing therefore lies not only in droplet generation itself, but also in maintaining temporal synchronization among droplet deposition, spreading, coalescence, evaporation, and crystallization. If local drying occurs before adjacent droplets fully merge, thickness discontinuities, voids, and irregular grain structures can readily emerge. Moreover, because large-area printing often requires prolonged operation, nozzle reliability and ink stability become critical practical constraints. Nozzle clogging, satellite droplets, or gradual rheological drift can directly introduce missing features and spatial nonuniformity across the printed area.

Compared with spray coating, inkjet printing is therefore particularly suitable for applications requiring patterned, localized, or digitally programmable deposition rather than rapid blanket coating. Nevertheless, scalable large-area implementation still requires careful coordination of droplet dynamics and crystallization kinetics. In practice, substrate heating, controlled gas flow, wettability engineering, and solvent/additive design are commonly employed to widen the processing window, regulate droplet coalescence, and suppress drying-induced heterogeneity.

The role of the printed droplet varies across reported inkjet processes. It can trigger a local conversion reaction, control the deposited precursor dose, or modify the drying pathway through solvent design. Wei et al. [35] demonstrated the first function using a reactive ink composed of carbon black and methylammonium iodide (MAI). In this process, inkjet printing did not deposit the complete perovskite absorber directly. A PbI_2 layer was first formed on compact TiO_2, after which the reactive ink was printed onto selected regions. The supplied MAI converted PbI_2 into $MAPbI_3$, while the carbon

component formed the electrode at the same location (Fig. 6(d)). This approach combined patterning, perovskite conversion, and electrode deposition in a single printing step. It also produced a more intimate $MAPbI_3$/carbon interface than the route based on separate carbon printing and MAI-bath conversion. The resulting planar carbon-based devices reached a PCE of 11.60%. When the complete absorber is deposited from a precursor ink, the local ink volume becomes a direct means of controlling film thickness. Eggers et al. [36] varied the printing resolution to adjust the amount of precursor delivered per unit area. The film thickness increased from approximately 400 nm at 600 dots per inch (dpi) to nearly 4 μm at 2,000 dpi, as shown by the selected cross-sectional scanning electron microscopy (SEM) images in Fig. 6(e). Large columnar grains extended through the printed absorbers, with few horizontal grain boundaries. Device performance reached its maximum at approximately 1,100 dpi, corresponding to a thickness of about 1.5 μm. At higher resolutions, the benefits of increased thickness and longer carrier lifetime were offset by poorer surface quality and compositional inhomogeneity. The optimized devices delivered a single-scan PCE above 21% and a stabilized PCE of up to 18.5%. A proof-of-concept device with an active area of approximately 1 cm^2 showed a mean PCE of 10.4%, indicating that further optimization was still required during area expansion. Ink formulation provides another route for regulating droplet drying and film formation. Chalkias et al. [37] developed a 0.8 M γ-valerolactone (GVL)-based ink as a lower-toxicity alternative to a conventional 1.8 M DMF-based formulation. The DMF ink produced rod-like structures, incomplete surface coverage, and periodic line defects associated with nonuniform drying (Fig. 6(f)). In contrast, the GVL ink formed a compact film with larger grains and fewer coffee-ring-type defects (Fig. 6(g)). The lower volatility and weak coordinating ability of GVL moderated solvent removal and reduced the formation of persistent solvent–precursor intermediates. This behavior improved the balance

between nucleation and crystal growth and also enabled annealing-free absorber formation. Using a carbon-based, hole-transport-material-free architecture, the authors fabricated an all-printed mini-module with a 100 cm^2 aperture area and a 52.4 cm^2 active area (Fig. 6(h)). The mini-module achieved a stabilized PCE of 10.07%, compared with 12.33% for a 0.32 cm^2 cell from the same batch. The above discussion indicates that inkjet printing is fundamentally a digitally programmed crystallization process in which droplet placement, coalescence dynamics, and local drying pathways jointly determine large-area film quality. Achieving reliable scalable printing therefore requires synchronized control over droplet generation, wet-film assembly, and supersaturation evolution throughout the deposition process.

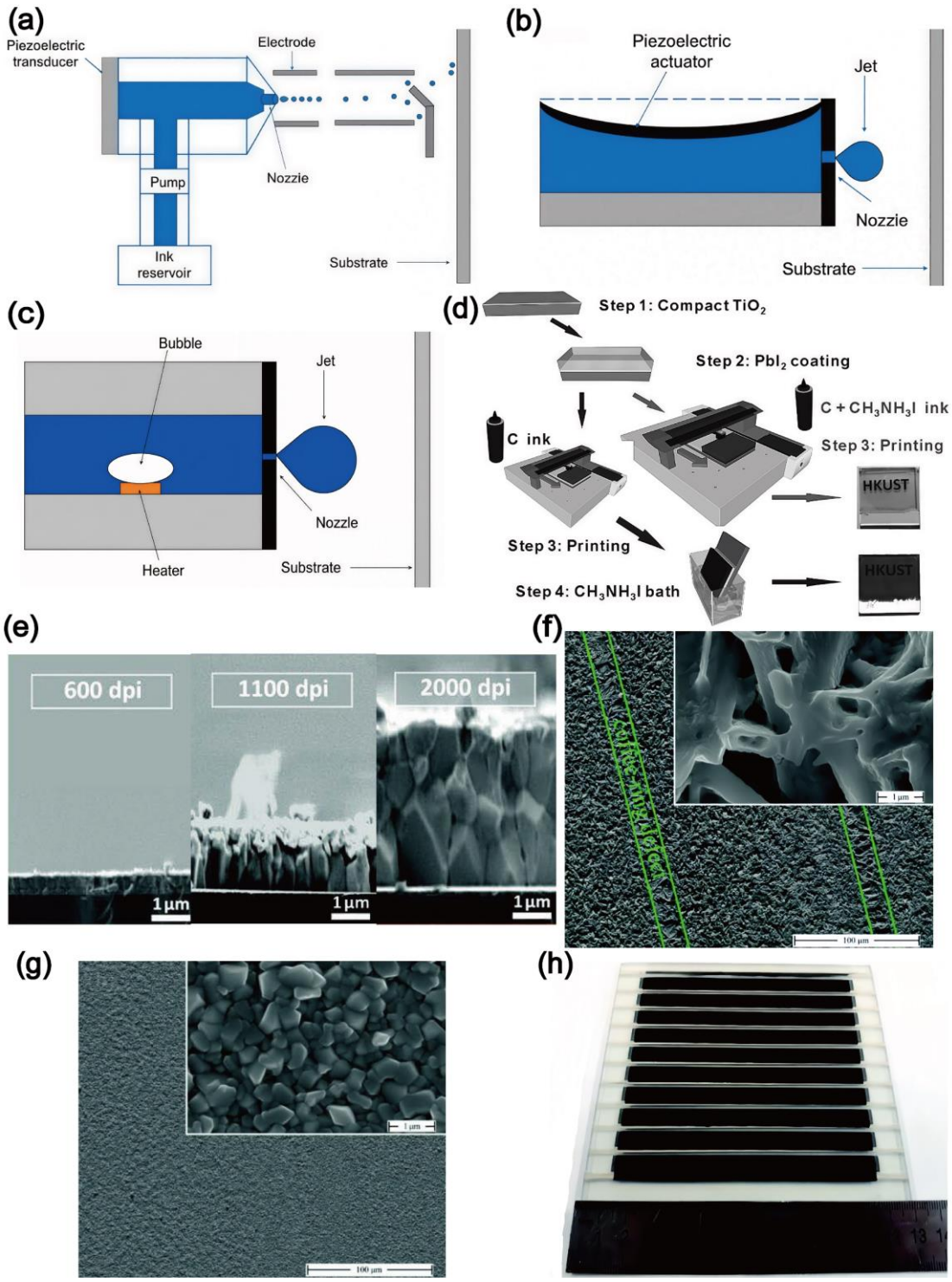

Fig. 6 (a-c) Schematics of typical inkjet-printing modes: (a) continuous inkjet (CIJ); (b) piezoelectric drop-on-demand (DOD); (c) thermal drop-on-demand (DOD). Reproduced from Ref. [38] under CC BY 4.0, © The Author(s) 2024. (d) Fabrication route for reactive inkjet printing of a carbon/MAI ink onto a predeposited PbI_2 layer. Reproduced with permission from Ref. [35], © Wiley-VCH Verlag

GmbH & Co. KGaA, Weinheim 2014. (e) Selected cross-sectional SEM images of inkjet-printed perovskite absorbers prepared at 600, 1,100, and 2,000 dpi. Reproduced with permission from Ref. [36], © The Authors 2019. (f, g) Top-view SEM images of perovskite films printed from (f) 1.8 M DMF- and (g) 0.8 M GVL-based precursor inks. (h) Photograph of an all-printed perovskite mini-module with a 100 cm^2 aperture area and a 52.4 cm^2 active area. Reproduced from Ref. [37] under CC BY, © The Authors 2023.

3.3 Printing-based deposition

Printing-based deposition differs fundamentally from both meniscus-guided coating and droplet-mediated deposition in the manner by which precursor ink is transferred to the substrate. Instead of forming a continuous liquid bridge or depositing isolated droplets, printing-based methods rely on patterned metering elements to repeatedly transfer controlled amounts of ink onto the substrate surface. During this process, precursor solution is first confined within predefined volumetric cells or patterned surface structures on a printing plate and subsequently transferred to the substrate under combined pressure and shear forces, forming a wet film with a designed geometry and thickness distribution.

From the perspective of crystallization control, the defining feature of printing-based deposition is that wet-film thickness and local solvent loading are preset by the transfer mechanics of the printing unit itself. Consequently, the quality and uniformity of the final perovskite film depend strongly on how efficiently and uniformly ink can be extracted from the patterned template and redistributed across the substrate before drying and crystallization occur. During mass transfer, ink flow from an individual metering cell to the substrate can be approximately described as pressure-driven viscous flow through a confined channel. Under a simplified cylindrical-channel approximation, the volumetric transfer rate can be expressed using the Hagen–Poiseuille relation:

$$Q = \frac{\pi D^4}{128\mu}\frac{\Delta p}{L} \tag{15}$$

where μ is the viscosity, Δp is the effective pressure drop, and D and L are the equivalent channel diameter and length scale, respectively. Although highly simplified, this relationship captures several important physical principles governing printing-based deposition. First, increasing the effective transfer pressure generally promotes more complete extraction of ink from the patterned cells and improves substrate coverage. Second, because flow rate scales strongly with the characteristic channel dimension ((D^4)), the geometry of the metering structure, including cell depth, aperture size, and pattern morphology, plays a decisive role in determining the transferable ink volume and resulting film-thickness uniformity. In contrast, higher ink viscosity suppresses transfer efficiency by increasing viscous resistance, thereby reducing deposited mass and potentially generating incomplete coverage.

Based on this transfer framework, the deposited wet-film thickness can be approximately related to the effective transferred volume per metering unit together with the projected transfer area and the overall transfer efficiency. In practical systems, however, the actual transferred volume is often lower than the nominal cell volume because of residual ink retention inside the template, back-suction during detachment, edge accumulation, incomplete spreading, and ink misting during high-speed operation. These transfer losses become increasingly important during large-area manufacturing because small local variations in transfer efficiency can evolve into macroscopic thickness nonuniformity and asynchronous crystallization behavior. After transfer, the deposited precursor film undergoes spreading, solvent evaporation, supersaturation buildup, and crystallization following mechanisms broadly similar to those discussed for other solution-based methods. However, because the initial wet-film geometry is discretely defined by the printing template, printing-based deposition is particularly sensitive to local transfer uniformity and contact-line stability. Uneven transfer or incomplete

spreading can readily induce thickness discontinuities, local drying heterogeneity, and spatial variations in nucleation density. Consequently, scalable printing-based deposition requires coordinated regulation of transfer mechanics, wetting behavior, and drying kinetics to ensure synchronized crystallization across the printed area. In practical processing, substrate heating, solvent engineering, rheology modification, and surface-energy control are frequently employed to stabilize transfer behavior and suppress drying-induced nonuniformity during large-area film formation.

3.3.1 Screen printing

As illustrated in Fig. 7(a), screen printing transfers precursor paste to the substrate through a patterned mesh under the combined action of pressure and shear. During printing, a squeegee drives the high-viscosity paste across the screen surface while simultaneously forcing it through the open mesh apertures onto the substrate. After the screen separates from the substrate (snap-off), the deposited paste undergoes relaxation, spreading, and leveling governed by surface tension and the thixotropic rheology of the paste itself, ultimately forming a continuous wet film. Compared with meniscus-guided coating and droplet-mediated deposition, screen printing operates in a fundamentally different rheological regime. Rather than relying on low-viscosity liquid entrainment or droplet coalescence, screen printing processes highly viscous, paste-like formulations in which transfer mechanics and post-transfer relaxation dominate the initial film-formation pathway. Consequently, the crystallization behavior of screen-printed perovskites is strongly coupled to paste rheology, pore filling, and solvent redistribution during relaxation and drying.

A key advantage of screen printing is its compatibility with thick and functional formulations. Because a relatively large precursor volume can be transferred in a single pass, the resulting film thickness typically ranges from several micrometers to tens of micrometers. This makes screen printing

particularly attractive for patterned electrodes, mesoporous scaffolds, and functional interlayers that require both substantial thickness and predefined geometry. In addition, the process inherently offers high material utilization and favorable compatibility with scalable R2R manufacturing. The quality of printed films is governed by the coupled effects of mesh geometry, transfer mechanics, and paste rheology. Screen parameters, including mesh count, open area, wire diameter, and screen tension, determine the transferable paste volume and achievable pattern resolution. Meanwhile, the snap-off distance and separation dynamics regulate liquid-bridge rupture and therefore influence edge definition and thickness uniformity. The squeegee hardness, angle, speed, and applied pressure collectively determine the local pressure drop and shear stress acting on the paste, thereby controlling mesh filling, transfer efficiency, and the formation of streak or stripe defects.

Paste rheology plays an equally important role. High viscosity improves shape retention after transfer but can hinder complete mesh filling and spreading. Conversely, overly low viscosity may improve transfer but increase edge spreading and thickness nonuniformity. The final morphology therefore depends critically on balancing viscous flow, thixotropic recovery, and surface-tension-driven leveling during the short post-transfer relaxation period before crystallization begins. Ink formulation, solvent volatility, ambient conditions, and drying protocols further regulate solvent redistribution and supersaturation evolution during this stage. For the crystallization control, screen printing introduces a distinct solidification environment compared with other solution-processing methods. Since the deposited layer is relatively thick and contains a high local solvent loading, solvent extraction and supersaturation buildup are often slower and more spatially heterogeneous. As a result, crystallization is particularly sensitive to pore infiltration, local drying gradients, and the synchronization between solvent removal and intermediate-phase conversion. Effective process design

therefore requires coordinated regulation of paste rheology, drying kinetics, and crystallization pathways to avoid void formation, incomplete conversion, and structural nonuniformity.

Recent studies have addressed the main constraints of screen printing at different stages of film formation. Chen et al. [39] developed a perovskite ink based on methylammonium acetate (MAAc). Its viscosity could be adjusted through temperature and precursor concentration. As shown in Fig. 7(b), cooling the ink or increasing its concentration produced a marked increase in viscosity. This tunability supported stable ink transfer through the screen and limited excessive spreading after release. The process produced continuous films with areas ranging from 0.25 to 25 cm^2 (Fig. 7(c)), while the film thickness could be adjusted from 120 to 1,200 nm. The resulting devices achieved PCEs of 20.52% and 18.12% at active areas of 0.05 and 1 cm^2, respectively. A fully screen-printed mini-module with a designated area of 16.37 cm^2 reached a PCE of 11.80%. A different problem arises when the perovskite ink is printed into a mesoporous scaffold. Chen et al. [40] introduced methylammonium propionate (MAPa) into the MAAc-based ink to regulate solvent removal and crystallization. With MAAc alone, perovskite crystals formed rapidly near the upper part of the m-TiO_2/m-ZrO_2 scaffold. The resulting surface layer restricted further solvent escape and left the lower pores incompletely converted (Fig. 7(d)). In the mixed-solvent system, MAPa slowed crystal growth and maintained channels for MAAc evaporation. Crystallization therefore extended further into the scaffold and produced denser pore filling (Fig. 7(e)). The optimized ink contained 75% MAAc and 25% MAPa and yielded a champion PCE of 16.95% in fully screen-printed carbon-electrode PVSCs. Yao et al. [41] addressed nonuniform film formation during droplet spreading and annealing. In the control ink, strong solvent-solute interactions restricted droplet spreading and promoted rapid nucleation at isolated positions. The transition from discrete dots to connected lines and then to a continuous film was therefore incomplete,

resulting in a discontinuous film with small grains (Fig. 7(f)). The addition of 1% chloride and 1% bromide weakened Pb-O coordination and improved ink wetting. Stronger interactions between Pb^{2+} and halide ions also delayed rapid phase formation. These changes allowed neighboring droplets to merge before crystallization and produced a continuous film with larger grains. The screen-printed devices reached a PCE of approximately 21.8%. A 5 × 5 cm^2 mini-module with an active area of 12.60 cm^2 achieved a PCE of 18.95%. These studies show that screen printing is not merely a pattern-transfer technique but a rheology-controlled crystallization process in which paste flow, solvent redistribution, and post-transfer relaxation jointly determine large-area film formation and device performance.

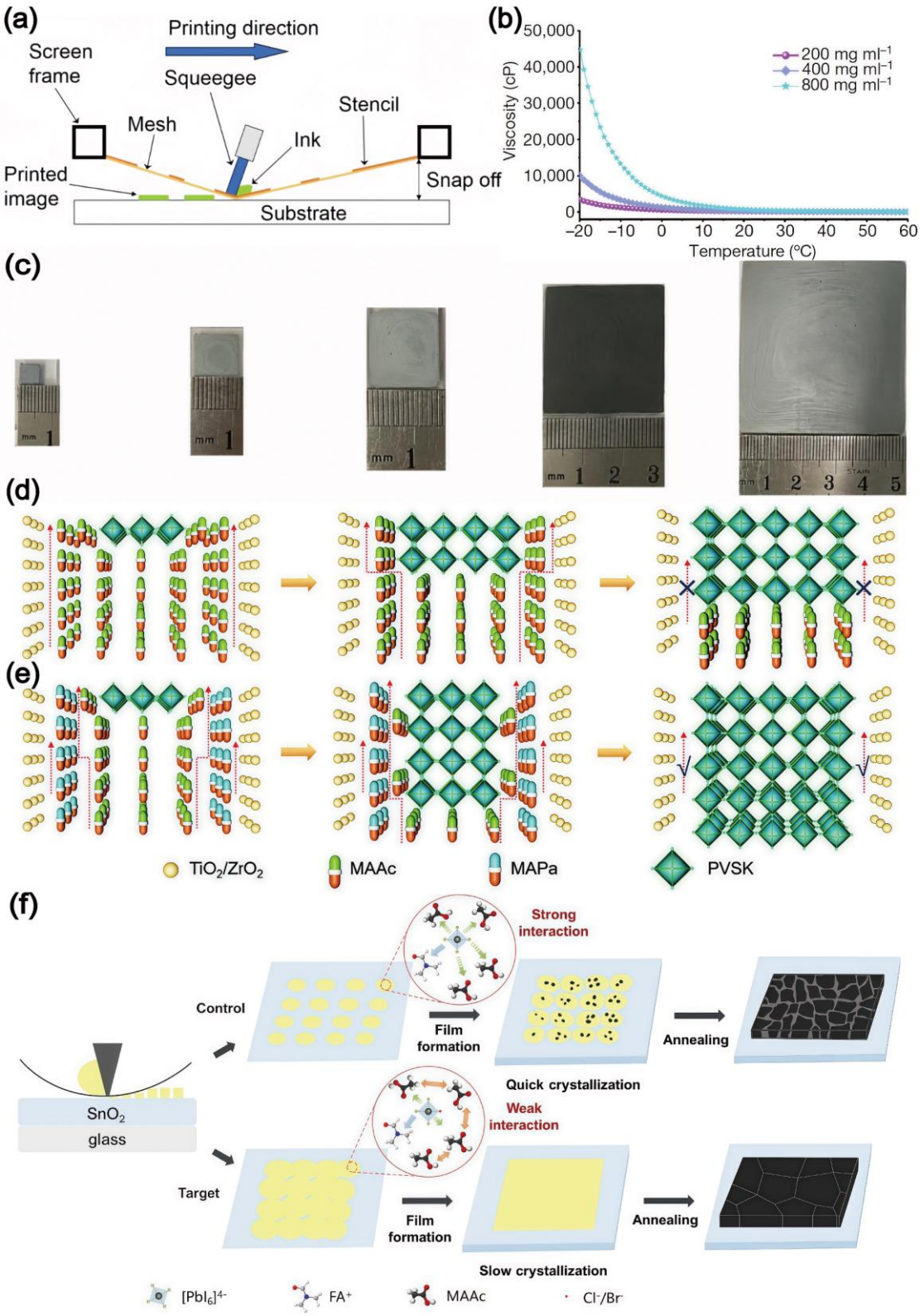

Fig. 7 (a) Schematic illustration of the screen-printing process. Reproduced with permission from Ref. [42], © Wiley-VCH Verlag GmbH & Co. KGaA, Weinheim 2018. (b) Temperature-dependent viscosity of perovskite inks with different precursor concentrations. (c) Photographs of screen-printed

perovskite films with areas ranging from 0.25 to 25 cm^2. Reproduced with permission from Ref. [39], © The Author(s) 2022. (d, e) Schematic illustration of perovskite crystallization within an m-TiO_2/m-ZrO_2 scaffold using (d) MAAc and (e) 75% MAAc + 25% MAPa as the solvent systems. Reproduced with permission from Ref. [40], © Wiley-VCH GmbH 2023. (f) Formation of screen-printed perovskite films from the control ink and the target ink containing 1% chloride and 1% bromide additives. Reproduced with permission from Ref. [41], © Wiley-VCH GmbH 2025.

3.3.2 Flexographic printing

Flexographic printing is a mature R2R manufacturing technology widely employed in high-throughput printing industries. Unlike screen printing, which transfers relatively thick paste layers through a mesh, flexographic printing utilizes a sequence of metered transfer steps to deliver a precisely controlled amount of low-viscosity ink onto a moving substrate. Consequently, flexographic printing is particularly attractive for large-area perovskite manufacturing because it combines high printing speed, patterning capability, and compatibility with continuous production lines. As illustrated in Fig. 8(a), the precursor solution is first supplied to a ceramic anilox roller containing a dense array of engraved microcells. These microcells act as volumetric reservoirs that meter a well-defined quantity of ink. Excess solution is removed by a doctor blade, leaving only the ink retained within the cells. The metered ink is subsequently transferred to a flexible printing plate carrying raised relief features and finally deposited onto the substrate under the pressure exerted by an impression cylinder [43]. Through this multi-stage transfer process, flexographic printing achieves precise control over ink delivery while maintaining high printing speeds.

For the perovskite film formation, the defining characteristic of flexographic printing is that wet-film thickness and solvent loading are predetermined by the volumetric transfer capacity of the anilox

roller. Consequently, the uniformity of subsequent crystallization depends strongly on the consistency of ink metering and transfer across the entire web width. Variations in transferred volume directly translate into local differences in wet-film thickness, drying rate, supersaturation evolution, and ultimately nucleation density. Several process parameters govern transfer uniformity. The geometry of the anilox cells, including cell volume, line count, depth, and open-area fraction, determines the amount of solution that can be carried and released during each printing cycle. Equally important is the interaction between the doctor blade and the anilox roller, which controls the removal of excess ink and suppresses cross-web streak formation. The mechanical properties of the printing plate, impression pressure, substrate speed, and web tension further influence transfer efficiency, feature fidelity, and edge definition [44].

Compared with other solution-processing techniques, the primary challenge in flexographic printing arises from its exceptionally high operating speed. As web velocity increases, the characteristic timescales of deposition, solvent evaporation, and crystallization become increasingly compressed. Maintaining film uniformity therefore requires careful synchronization between ink transfer and solvent removal. If drying proceeds too slowly, excessive liquid redistribution and feature broadening may occur. Conversely, overly rapid solvent loss can induce premature supersaturation, nonuniform nucleation, and incomplete film coalescence. Effective process design thus requires coordinated control of ink rheology, substrate temperature, drying conditions, and printing speed to ensure that crystallization remains synchronized across the moving web.

These coupled requirements are illustrated by recent studies that progressed from high-speed additive patterning to the control of spatial nonuniformity during ink transfer and leveling. Huddy et al. [43] demonstrated direct control over printing and post-transfer drying by depositing

$MA_{0.6}FA_{0.4}PbI_3$ absorbers at 60 m·min^{-1}. Flexography also allowed the perovskite pattern to be formed during deposition and therefore avoided a separate scribing step. The optical micrographs in Fig. 8(b) show that mechanical scribing left residual material, while laser scribing produced a less regular edge. In contrast, additive flexographic patterning formed a clean and continuous gap. The process produced features of approximately 50 μm with a line-edge roughness below 3 μm and was demonstrated over an area of 140 cm^2. Devices containing the optimized flexography-printed absorbers reached a PCE of 20.4% over an active area of 0.134 cm^2. High printing speed alone, however, does not ensure spatial uniformity. When the printing plate separates from the substrate, ink splitting can introduce periodic thickness disturbances. These disturbances develop into Saffman–Taylor fingers if the ink does not level before drying fixes the wet-film profile (Fig. 8(c)). The same group later examined this competition using Bayesian optimization [45]. The study varied the Pb concentration, 2-methoxyethanol content, DMSO content, MA fraction, printing pressure, and anilox-cell volume. Spatial variation in photoluminescence (PL) intensity was used to evaluate film uniformity. The PL map and fast Fourier transform in Fig. 8(d) reveal the periodic structure left by incomplete leveling. After optimization, the more uniform ink produced small-area devices with PCEs of approximately 20% and 1 cm^2 devices with PCEs above 16%. The less uniform ink showed a larger performance loss after the device area was increased (Fig. 8(e)). These studies highlight that flexographic printing is fundamentally a high-throughput, metered-transfer crystallization process. Successful implementation depends not only on precise ink delivery but also on synchronizing wet-film formation, solvent removal, and crystallization under the extremely short residence times associated with industrial R2R manufacturing.

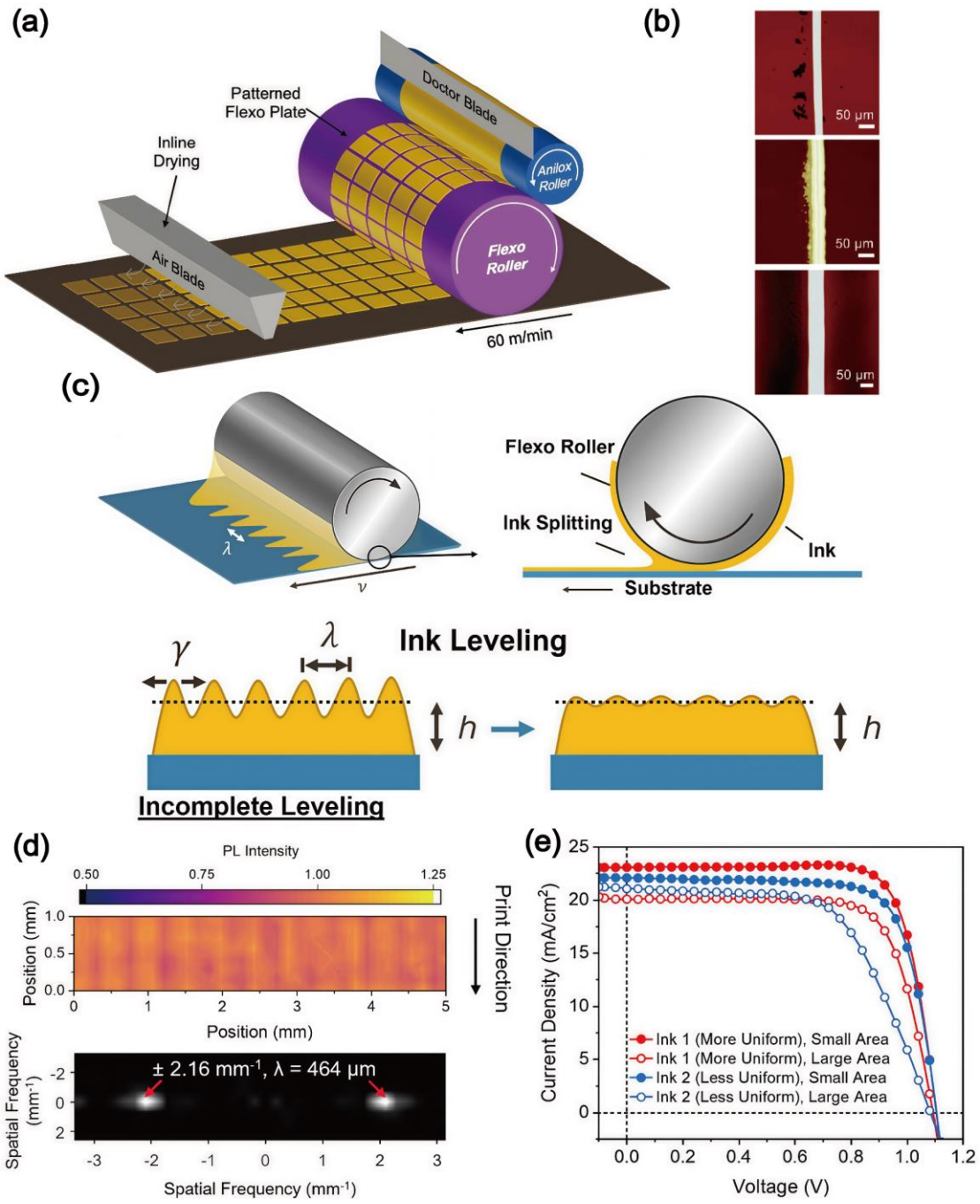

Fig. 8 (a) Schematic illustration of a typical flexographic printing process. (b) Optical micrographs of perovskite pattern edges produced by mechanical scribing, laser scribing, and additive flexographic patterning, from top to bottom. Reproduced with permission from Ref. [43], © Wiley-VCH GmbH 2023. (c) Schematic illustration of ink splitting, the formation of Saffman-Taylor disturbances, and subsequent ink leveling after transfer from the flexographic plate. (d) PL map and corresponding fast Fourier transform of an incompletely leveled perovskite film, showing periodic variations along the

printing direction. (e) J-V characteristics of small-area and 1 cm^2 devices prepared with the more uniform and less uniform inks. Reproduced with permission from Ref. [45], © Wiley-VCH GmbH 2025.

3.3.3 Gravure printing

Gravure printing is a high-resolution, R2R compatible deposition technology that has attracted increasing attention for scalable perovskite manufacturing. Similar to flexographic printing, gravure printing relies on volumetric ink metering through a rotating cylinder. However, in gravure printing the metering function is integrated directly into the engraved cylinder itself, enabling highly precise control over ink transfer and pattern definition at industrially relevant web speeds. As shown in Fig. 9(a), the surface of the gravure cylinder contains a dense array of micron-scale engraved cells that serve as ink reservoirs. During operation, the cylinder rotates through an ink bath, allowing the cells to become filled with precursor solution. Excess ink remaining on the cylinder surface is subsequently removed by a doctor blade, leaving only the metered volume retained within the engraved cells. When the cylinder enters the nip region and contacts the receiving substrate, the ink is transferred from the cells to the substrate surface, forming a patterned wet film that subsequently undergoes spreading, solvent evaporation, supersaturation buildup, and crystallization to yield the final perovskite layer [46].

For the film formation, gravure printing can be viewed as a metered-transfer crystallization process in which the initial wet-film geometry is predetermined by the cell architecture of the gravure cylinder. Consequently, the local solvent loading, wet-film thickness, and supersaturation trajectory are directly linked to the volume and spatial distribution of ink released from individual cells. Uniform crystallization therefore requires not only consistent ink transfer but also synchronized drying and phase conversion across the printed area. The key process variables originate from both cell geometry

and transfer dynamics. Parameters such as cell depth, cell volume, cell opening area, and engraving density determine the amount of ink available for transfer and ultimately influence the achievable film thickness and pattern resolution. Meanwhile, gravure-cylinder speed affects the residence time available for cell filling and ink release. Doctor-blade angle, contact force, and blade stability govern the removal of excess ink and therefore influence cross-web uniformity and defect formation. The nip pressure between the gravure cylinder and substrate further controls transfer efficiency and feature fidelity.

Ink rheology plays a particularly important role in gravure printing. The precursor solution must simultaneously satisfy several requirements including efficient filling of the engraved cells, stable retention during cylinder rotation, reproducible release during substrate contact, and sufficient post-transfer spreading to eliminate discontinuities between adjacent printed regions. Consequently, ink viscosity, surface tension, solvent volatility, and drying kinetics must be carefully matched to the cell geometry and printing speed. In practice, optimization of gravure printing is therefore often achieved through the co-design of ink formulation and cylinder architecture. Compared with other solution-processing methods, the key challenge in gravure printing lies in maintaining synchronized crystallization under high-speed continuous operation. Because wet-film thickness is determined by discrete cell-to-cell transfer events, local variations in transfer efficiency can generate thickness fluctuations and nonuniform solvent distribution. Furthermore, the high web speeds commonly used in gravure printing compress the timescales of spreading, solvent evaporation, and crystal nucleation. If solvent removal is too slow, excessive liquid redistribution and pattern distortion may occur. Conversely, overly rapid drying can induce premature supersaturation and spatially heterogeneous nucleation. Effective large-area processing therefore requires coordinated regulation of transfer

mechanics, solvent extraction, and crystallization kinetics.

Early studies established that crystallization control must be closely coordinated with ink transfer during gravure printing. Kim et al. [47] used antisolvent bathing immediately after printing to convert the wet precursor layer into $MAPbI_3$. The engraved pattern was reproduced on the flexible substrate with clear edges, demonstrating the patterning capability of gravure printing (Fig. 9(b)). The optimized process produced dense perovskite films and enabled gravure printing of SnO_2, $MAPbI_3$, and Spiro-OMeTAD on flexible polyethylene terephthalate/indium tin oxide (PET/ITO) substrates. The resulting devices reached a PCE of 17.2%. The same group subsequently developed a tert-butanol (tBuOH) antisolvent bath with a wider processing window [48]. The device efficiency remained nearly unchanged when the bathing time was varied from 10 to 60 s (Fig. 9(c)). This tolerance reduced the sensitivity of film formation to fluctuations in web transport and bath residence time. The method was then transferred to a pilot-scale R2R process. Gravure-printed flexible devices reached 19.1%, while fully R2R-processed devices with a poly(3-hexylthiophene) hole-transport layer achieved 13.8%.

Antisolvent bathing nevertheless increases solvent consumption and adds another unit to the production line. Bisconti et al. [49] addressed this limitation by adding starch as a rheological modifier to the perovskite ink. The polymer increased the ink viscosity and helped regulate film formation after transfer from the engraved cells. Perovskite layers could therefore be printed under ambient conditions without an antisolvent bath, gas blowing, or a heated substrate. As shown in Fig. 9(d), the printed layer was crystallized by infrared treatment followed by thermal annealing. The process was implemented on a pilot R2R line (Fig. 9(e)) using flexible substrates with a total length of 50 m. The resulting devices reached PCEs close to 10%. Although the efficiency was lower than that obtained with antisolvent bathing, the process required fewer manufacturing steps and reduced precursor and solvent

consumption. Ink modification has also been used to address the phase instability of gravure-printed $FAPbI_3$. Vanni et al. [50] introduced camphorsulfonic-salified chitosan (CHIC) into the precursor solution. CHIC adjusted the ink viscosity, improved film morphology, and stabilized the photoactive α-phase without requiring methylammonium chloride or an antisolvent bath. Flexible gravure-printed devices containing 2 $mg \cdot mL^{-1}$ CHIC reached a PCE of 13.4%. The additive also improved shelf stability. Unencapsulated devices containing CHIC retained more than 80% of their initial efficiency after 1,200 h in ambient air, whereas the reference devices degraded rapidly (Fig. 9(f)). Overall, gravure printing represents a transfer-controlled crystallization process in which cylinder architecture, ink rheology, and drying dynamics collectively determine wet-film formation and subsequent crystal growth. Its combination of precise volumetric metering, high pattern resolution, and compatibility with continuous R2R production makes gravure printing a promising platform for future large-area perovskite photovoltaic manufacturing.

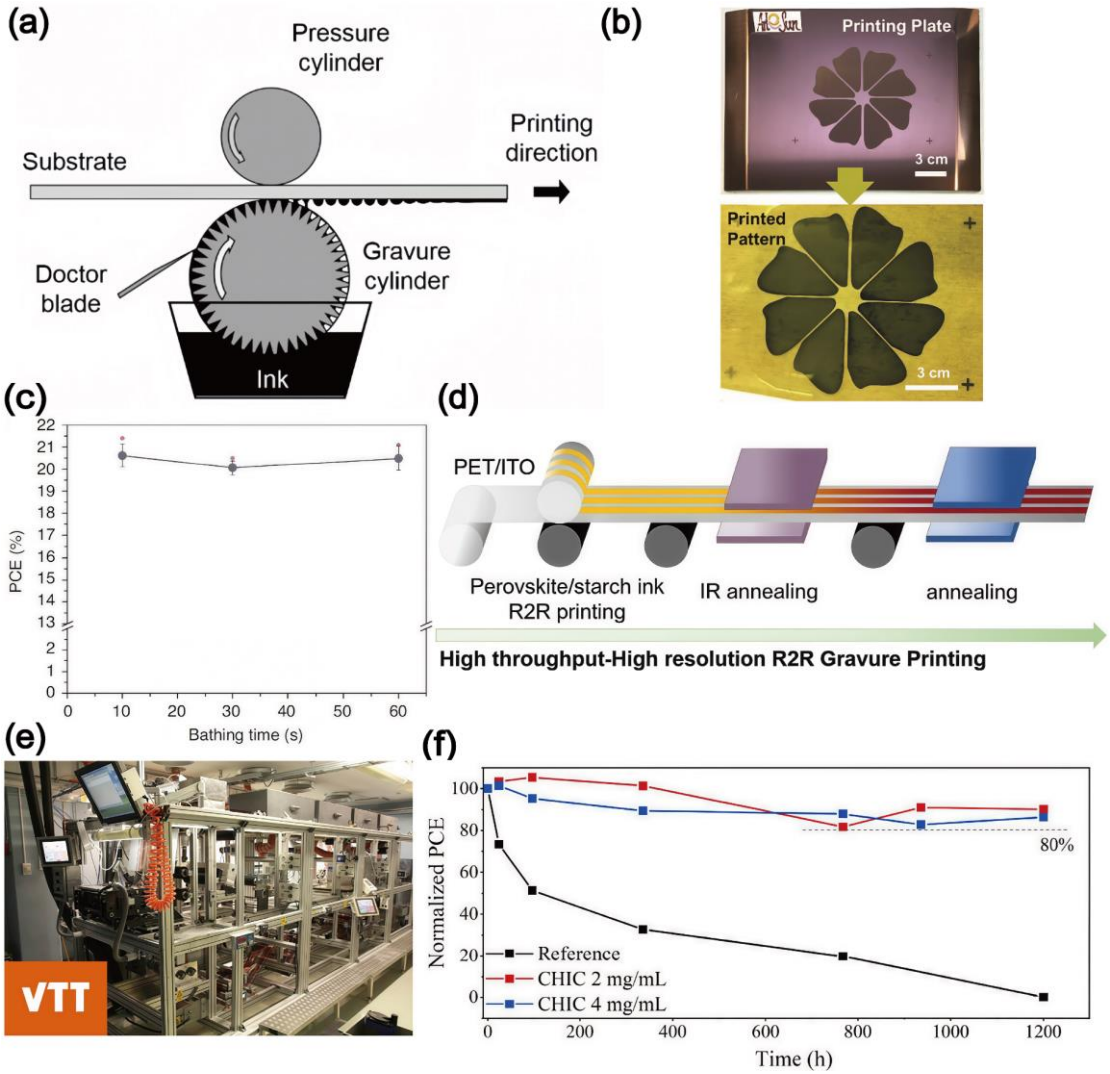

Fig. 9 (a) Schematic illustration of the gravure-printing process, including ink metering by the engraved cylinder and doctor blade. Reproduced from Ref. [51] under CC BY 4.0, © The Author(s) 2022. (b) Photographs of the engraved printing plate and the corresponding perovskite pattern printed on a flexible PET substrate. Reproduced from Ref. [47] under CC BY, © The Authors 2019. (c) PCE of devices prepared using different tBuOH bathing times. Reproduced from Ref. [48] under CC BY 4.0, © The Author(s) 2020. (d) Antisolvent-free R2R gravure printing of a perovskite–starch ink, followed by infrared treatment and thermal annealing. (e) Photograph of the pilot R2R gravure-printing line. Reproduced from Ref. [49] under CC BY 4.0, © The Authors 2021. (f) Shelf stability of unencapsulated $FAPbI_3$ devices containing different concentrations of CHIC during storage in ambient

air. Reproduced from Ref. [50] under CC BY, © The Author(s) 2024.

3.4 Comparison of solution-processing routes from a crystallization-control perspective

Although meniscus-guided coating, droplet-mediated deposition, and printing-based approaches differ substantially in deposition configuration and fluid-delivery mechanisms, they ultimately share a common objective that is generating a wet precursor layer that evolves through solvent evaporation, supersaturation buildup, nucleation, crystal growth, and solidification into a continuous perovskite film. From a crystallization perspective, the key distinction among these methods lies not in how the precursor is delivered, but in how mass transport and solvent removal are regulated during film formation.

Meniscus-guided coating establishes a continuous wet film through hydrodynamic entrainment and therefore offers the most direct control over film thickness and solvent-evaporation dynamics. Droplet-mediated deposition forms the film through droplet impact, spreading, and coalescence, making crystallization highly sensitive to local thickness fluctuations and drying heterogeneity. Printing-based methods rely on volumetric ink transfer from patterned templates, where rheology, transfer efficiency, and post-transfer relaxation largely determine the subsequent supersaturation pathway and crystallization behavior. Despite these differences, all solution-processing routes face a common challenge during scale-up which is maintaining synchronized supersaturation evolution and crystallization across large areas. Spatial variations in thickness, evaporation rate, temperature, or solute concentration can lead to heterogeneous nucleation, non-uniform grain growth, and defect formation. Therefore, scalable perovskite manufacturing fundamentally requires simultaneous control of fluid transport, mass transfer, and crystallization kinetics. The major characteristics of different solution-processing routes are summarized in Table 1.

Table 1. Comparison of scalable solution-processing routes from a crystallization perspective.

Process category	Representative methods	Film formation mechanism	Dominant transport process	Primary crystallization challenge	Relative scalability	Relative crystallization controllability
Meniscus-guided coating	Blade coating, Slot-die coating	Continuous wet-film entrainment	Hydrodynamic flow and solvent evaporation	Synchronizing supersaturation across large areas	Excellent	High
Droplet-mediated deposition	Spray coating, Inkjet printing	Droplet impact, spreading, and coalescence	Droplet transport and local drying	Suppressing local nucleation heterogeneity and coffee-ring effects	Moderate-High	Moderate
Printing-based deposition	Screen printing, Flexographic printing, Gravure printing	Metered ink transfer from patterned templates	Ink transfer and post-transfer leveling	Uniform solvent distribution and crystallization after transfer	High	Moderate-High

Note: The qualitative ratings provide relative comparisons among the three process categories. Relative scalability considers compatibility with continuous processing, deposition throughput, and the ability to maintain uniform material delivery over large areas. Relative crystallization controllability considers control over wet-film thickness, solvent removal, supersaturation evolution, and spatially synchronized crystallization. The ratings may vary with equipment design, ink formulation, and operating conditions.

From a solidification viewpoint, the progression from meniscus-guided coating to droplet-mediated and printing-based deposition represents a gradual transition from hydrodynamic-controlled film formation to transfer-controlled film formation. However, regardless of the deposition strategy, the final film quality is ultimately governed by the same sequence of supersaturation generation, nucleation, crystal growth, and defect evolution. This common crystallization framework provides a useful basis for comparing solution-processing and vapor-based deposition routes, which are discussed in the following section.

4 Vapor-based deposition: growth kinetics and control

In solution processing, perovskite film formation is governed by the coupled evolution of fluid flow, solvent evaporation, supersaturation buildup, nucleation, and crystal growth. Consequently, large-area film quality is highly sensitive to spatial variations in wet-film thickness, evaporation rate, and solute transport, which can lead to asynchronous crystallization and non-uniform microstructures. As discussed in the previous sections, scalable solution processing fundamentally requires precise control over supersaturation pathways and crystallization kinetics across the entire coating area.

Vapor-based deposition follows a fundamentally different route to perovskite film formation. Instead of generating supersaturation through solvent removal, precursors are supplied directly in the gas phase and transported to the substrate surface, where film growth proceeds through adsorption, surface diffusion, chemical reaction, nucleation, and lattice incorporation. Film formation is therefore governed primarily by vapor transport and surface-growth kinetics rather than by wet-film hydrodynamics. From a solidification perspective, the controlling variable shifts from solution supersaturation to precursor flux, surface reaction rate, and adatom mobility.

This difference provides several potential advantages for large-area manufacturing. Because

precursor delivery can be precisely regulated through source temperature, vapor pressure, gas flow, or deposition power, vapor-based methods generally offer superior control over film thickness, composition uniformity, and multilayer interface formation. Furthermore, the absence of liquid flow eliminates many defects associated with solvent evaporation, dewetting, and drying-induced heterogeneity. However, vapor-phase growth introduces its own challenges, including maintaining stoichiometric precursor incorporation, controlling phase evolution during growth, mitigating thermal decomposition, and achieving high throughput over large areas. Although vapor-based deposition encompasses diverse techniques, including CVD, thermal evaporation, sputtering, electron-beam evaporation, and pulsed laser deposition (PLD), their underlying physics can be understood within a common framework consisting of five sequential steps which are precursor generation, vapor-phase transport, surface adsorption, crystal growth through incorporation and reaction, and eventual formation of the target perovskite phase. The efficiency and uniformity of each step collectively determine the final film quality and device performance. Based on this crystallization-centered perspective, the following sections discuss vapor-based deposition methods according to their dominant growth mechanisms. First, CVD-based approaches are examined from the viewpoint of gas-phase transport and surface-reaction kinetics. Next, evaporation-based methods are analyzed as flux-controlled growth processes. Finally, sputtering, electron-beam evaporation, and pulsed laser deposition are discussed as energy-assisted non-equilibrium deposition routes, where energetic species introduce additional kinetic pathways for film formation and crystallization.

4.1 Chemical vapor deposition: transport, reaction, and conversion kinetics

Chemical vapor deposition (CVD) represents one of the main vapor-phase routes for perovskite film growth. In contrast to solution processing, where crystallization is driven by solvent evaporation

and supersaturation buildup, CVD relies on the continuous delivery of volatile precursors from the gas phase to the substrate surface, where nucleation, crystal growth, and phase formation occur through gas–solid reactions. Consequently, film formation is governed by the interplay between precursor transport and surface reaction kinetics. The overall growth process can be divided into five sequential steps: (i) precursor generation at the source, (ii) vapor-phase transport through the reactor, (iii) mass transfer across the near-surface boundary layer, (iv) adsorption and surface reaction, and (v) incorporation into the growing perovskite lattice. Uniform film formation requires each of these steps to proceed in a spatially synchronized manner across the entire substrate.

The first step is precursor generation. For a volatile precursor species i, the source sublimation or evaporation flux (kg·m^{-2}·s^{-1}) can be described by the Knudsen-Langmuir relation [52,53]:

$$J_{sub,i} = \alpha_i\left(P_{sat,i} - P_i\right)\sqrt{\frac{M_i}{2\pi RT}} \tag{16}$$

where $J_{sub,i}$ is the sublimation or evaporation mass flux of precursor species i at the source. α_i is the condensation coefficient. $P_{sat,i}$ is the saturation vapor pressure of species i at the source temperature T. P_i is the corresponding partial pressure in the reactor. M_i is the molar mass of species i, and R is the gas constant (J·mol^{-1}·K^{-1}). Eq. (16) shows that the source temperature sets the thermodynamic driving force for precursor generation through the difference between the saturation vapor pressure and the actual working partial pressure.

The temperature dependence of the saturation vapor pressure can be described by the Clausius-Clapeyron relation [54]:

$$\ln\frac{P_{sat,i,2}}{P_{sat,i,1}} = -\frac{\Delta H_{\mathrm{i}}}{R}\left(\frac{1}{T_2} - \frac{1}{T_1}\right) \tag{17}$$

where ΔH_{i} is the sublimation enthalpy of precursor species i (J·mol^{-1}). T_1 and T_2 are two source temperatures corresponding to saturation vapor pressures $P_{sat,i,1}$ and $P_{sat,i,2}$ respectively. Eq. (17)

implies that precursor supply can rise sharply with heating because the saturation vapor pressure increases exponentially with source temperature.

The source-release flux is not the same as the flux arriving at the substrate. After leaving the source, precursor species are transported by convection and diffusion. Their concentration distribution depends on carrier-gas flow, reactor pressure, temperature, residence time, and reactor geometry [55,56]. Higher temperature generally promotes diffusion. Higher pressure increases the precursor concentration but reduces its diffusivity. The concentration above the substrate reflects the balance between these effects [57,58]. Gas-phase reactions, condensation, and deposition on the reactor wall may further reduce the amount available for film growth.

Near the substrate, precursor delivery is controlled by the gas-phase boundary layer. The molar flux of precursor i to the substrate surface can be written as [59,60]:

$$J_{mt,i} = h_i\left(C_{i,g} - C_{i,s}\right), \qquad h_i \sim D_i/\delta \tag{18}$$

where $J_{mt,i}$ ($\mathrm{mol \cdot m^{-2} \cdot s^{-1}}$) is the molar flux arriving at the substrate surface. $C_{i,g}$ is the precursor concentration in the bulk gas, and $C_{i,s}$ is its concentration next to the substrate. The mass-transfer coefficient h_i depends on the diffusion coefficient D_i, the boundary-layer thickness δ, and the local flow conditions. A larger concentration difference increases the driving force for mass transfer. Faster diffusion or a thinner boundary layer also increases the surface flux.

Boundary-layer transport is especially important during large-area deposition. Flow velocity and temperature may vary across a large substrate. These variations change $C_{i,g}$, D_i, and δ. The resulting surface flux may therefore differ from one position to another. Such differences can produce nonuniform film thickness, composition, and reaction rate, even when the average precursor supply is sufficient. After reaching the substrate, the precursor must adsorb and react before it can enter the

growing perovskite lattice. The temperature dependence of the effective reaction-rate coefficient can be described by the Arrhenius relation [61]:

$$k_{\mathrm{r}} = A_{pre} \exp\left(-\frac{E_a}{RT}\right) \tag{19}$$

where k_{r} is the effective reaction-rate coefficient, A_{pre} is the pre-exponential factor, and E_a is the activation energy. Eq. (19) describes the kinetic effect of substrate temperature. It does not describe precursor delivery. When surface reaction is much faster than precursor delivery, $C_{i,s}$ decreases and growth becomes mass-transfer-limited. When surface reaction is slower, precursor consumption at the surface becomes the limiting step. Intermediate conditions correspond to mixed control. Net film growth is therefore determined by both the surface flux in Eq. (18) and the reaction kinetics in Eq. (19). The following sections apply this framework to two CVD routes: direct single-step growth and two-step vapor–solid conversion.

4.1.1 Single-step CVD: direct vapor-phase growth

Single-step CVD feeds the organic and inorganic precursors into the reactor during the same deposition period. The vapors reach a heated substrate and form the perovskite directly at the gas-solid interface. No predeposited inorganic layer or separate vapor-conversion step is required. This shortens the processing sequence but makes film growth more sensitive to the ratio of the precursor fluxes.

For a hybrid perovskite with the general formula ABX_3, the overall reaction can be written in an idealized form as:

$$\mathrm{A}X(g) + BX_2(g) \rightarrow ABX_3(s) \tag{20}$$

where $\mathrm{A}X(g)$ denotes a vapor-phase organic ammonium halide (e.g., MAI or formamidinium iodide (FAI)), $BX_2(g)$ denotes a vapor-phase metal halide (e.g., PbI_2 or $PbCl_2$), and $ABX_3(s)$ is the target perovskite solid.

Sustained growth requires both precursors to reach the surface in appropriate amounts. Under steady or quasi-steady conditions, the incorporated flux of each species can be related to the net surface formation rate:

$$J_{inc,i} = \nu_i \, r_s \quad (i = AX,\, BX_2) \tag{21}$$

where $J_{inc,i}$ is the net molar flux of species i incorporated into the film, ν_i is its stoichiometric coefficient, and r_s is the effective net formation rate of the perovskite per unit area. Here, r_s reflects the combined effects of precursor adsorption, surface reaction, lattice incorporation, desorption, and decomposition. Its value is governed mainly by the substrate temperature and the near-surface partial pressures of both precursors. At low surface coverage, an increase in either precursor partial pressure can raise r_s. When one precursor is present in excess, r_s is controlled mainly by the deficient precursor. For the reaction described by Eq. (20), the relative net molar fluxes incorporated into the film should be consistent with the stoichiometric coefficients required for forming the target perovskite.

The corresponding film-thickness growth rate is:

$$\frac{dd}{dt} = \frac{M_f}{\rho_f} \, r_s \tag{22}$$

where M_f and ρ_f are the molar mass and density of the perovskite, respectively. Eqs. (20)-(22) connect the single-step reaction to the precursor-generation and transport processes described by Eqs. (16)-(19). Source temperature controls vapor generation, while pressure and carrier-gas flow determine precursor transport through the reactor. Substrate temperature affects adsorption, surface reaction, and desorption. The objective is therefore not to maximize the total precursor supply, but to maintain a stable stoichiometric window at the growth surface.

Over a large substrate, the local flux ratio may vary even when the inlet ratio is fixed. Temperature gradients, precursor depletion, and nonuniform boundary layers can therefore generate spatial

variations in r_s, film thickness and phase composition. Representative studies show how single-step CVD evolved from shared-flow solid-source systems toward more independent control of precursor activation and delivery. Tavakoli et al. [62] provided an early demonstration of single-step CVD for planar PVSCs. As shown in Fig. 10(a), MAI and PbX_2 were placed at different positions in a tube furnace according to their vaporization behavior. An Ar flow transported both vapors to TiO_2/FTO substrates in a lower-temperature region, where the perovskite formed directly. After optimization of the source temperature and in situ annealing, the process produced continuous $MAPbI_3$ and $MAPbI_{3-x}Cl_x$ films. The mixed-halide devices reached a PCE of 11.1% (Fig. 10(b)). Because both precursor vapors were transported by the same carrier-gas flow, the local flux ratio remained sensitive to source position, source temperature, and precursor depletion. Muratov et al. [63] subsequently examined whether precursor selection could reduce this mismatch. $PbAc_2$ could be processed at a lower temperature than PbI_2 and produced smoother $MAPbI_3$ films under the reported conditions. The reactor was later modified to provide separate carrier-gas flows and distinct evaporation and deposition zones. The resulting absorber was incorporated into an inverted p-i-n device, which reached a PCE of 5.54% after dark storage. The strong post-fabrication change indicates that the absorber and its interfaces remained metastable. Precursor substitution can widen the deposition window, but independent flux control and post-growth stabilization are still required.

More precise control was demonstrated by Bryan et al. [64] using metal-organic chemical vapor deposition (MOCVD). As shown in Fig. 10(c), methylamine, hydrogen halide, and $PbEt_4$ were delivered through separate precursor streams. A single-temperature reactor produced sparse $MAPbI_3$ coverage because the temperature required for $PbEt_4$ activation was incompatible with stable perovskite growth. The reactor was therefore divided into two temperature zones. The upstream

temperature T_1 activated the lead precursor, while the downstream temperature T_2 controlled perovskite growth. Continuous and phase-pure $MAPbI_3$ films were obtained at T_1 = 300 °C and T_2 = 170 °C. The phase map in Fig. 10(d) defines the corresponding growth window. Low T_1 resulted in MAI-rich material or no lead-containing deposit, whereas high T_2 favored PbI_2 because of perovskite decomposition. Excessively high T_1 also shifted the product toward a lead-rich composition. Phase-pure $MAPbI_3$ was obtained only within an intermediate region where precursor activation and film stability were balanced. The growth rate increased strongly with T_1 (Fig. 10(e)). An Arrhenius fit gave an apparent activation energy of 43.7 ± 17.3 kcal·mol^{-1}, close to the calculated value of 44.1 kcal·mol^{-1} for $PbEtI_3$ formation. This agreement suggests that activation of the lead precursor was a rate-limiting step rather than simple precursor evaporation.

Single-step CVD therefore places the main control problem at the growth surface, where the precursor flux ratio must remain within a phase-pure window while activation and incorporation rates vary with reactor temperature. Shared-flow solid-source systems provide a simple configuration but remain vulnerable to precursor depletion and thermal gradients. Independently metered MOCVD separates precursor activation from film growth, although it requires more demanding precursor handling and exhaust management. For large-area deposition, the relevant design target is a spatially stable stoichiometric window rather than the highest possible precursor supply.

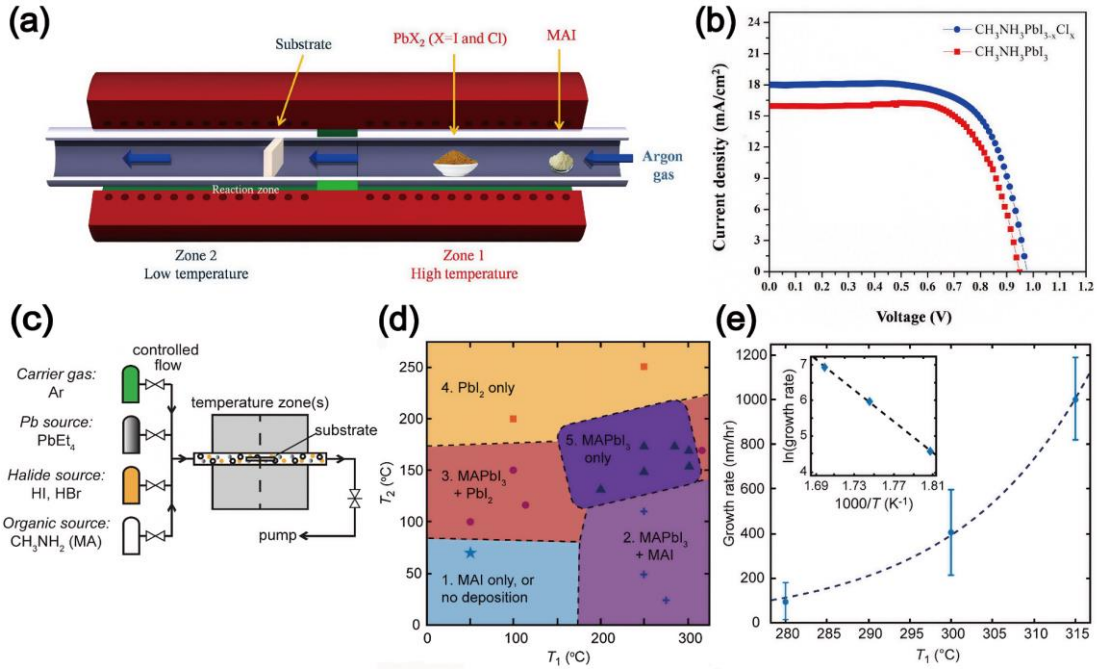

Fig. 10 (a) Schematic of single-step CVD using spatially separated MAI and PbX_2 sources, an Ar carrier gas, and a lower-temperature substrate region. (b) Current density-voltage characteristics of $MAPbI_3$ and $MAPbI_{3-x}Cl_x$ solar cells prepared by single-step CVD. Reproduced from Ref. [62] under CC BY 4.0, © The Author(s) 2015. (c) Schematic of an MOCVD reactor with independently controlled methylamine, hydrogen halide, and $PbEt_4$ precursor streams. (d) Phase map showing the products obtained at different activation-zone temperatures (T_1) and growth-zone temperatures (T_2). (e) $MAPbI_3$ growth rate as a function of T_1; the inset shows the corresponding Arrhenius analysis. Reproduced with permission from Ref. [64], © American Chemical Society 2025.

4.1.2 Two-step CVD: vapor-solid conversion growth

Two-step CVD separates the deposition of the inorganic precursor from the subsequent vapor-solid conversion. An inorganic metal-halide layer is first deposited on the substrate by solution coating or vacuum evaporation. An organic halide is then supplied in the vapor phase and reacts with the predeposited layer. For an idealized ABX_3 perovskite, this conversion can be represented as:

$$AX(g) + BX_2(s) \rightarrow ABX_3(s) \tag{23}$$

where $AX(g)$ represents the vapor-phase organic halide and $BX_2(s)$ represents the solid inorganic precursor. Eq. (23) describes the overall stoichiometric relationship rather than the detailed reaction pathway. More complex expressions are required for mixed-cation or mixed-halide compositions. Unlike single-step CVD, the amount of BX_2 is fixed before vapor exposure. The inorganic precursor loading and the AX vapor supply can therefore be adjusted independently.

The general mass-balance relation in Eq. (22) remains applicable to two-step CVD. However, the net formation rate r_s is generally not constant. Once the first perovskite layer forms, the incoming AX species must pass through this product layer before reaching the remaining BX_2. The conversion rate is therefore controlled by gas-phase transport, diffusion through the perovskite layer, and reaction at the buried interface.

Zhu et al. [65] developed a moving-front model for the conversion of PbI_2 by MAI vapor. Using generalized symbols, the relation between the converted perovskite thickness and reaction time can be written as:

$$d^2 + \left(\frac{D}{h} + \frac{D}{k}\right) d = \frac{DC_1}{N} t \tag{24}$$

where, d is the thickness of the converted perovskite layer. D is the effective diffusivity of AX through the product layer, and h is the gas-phase mass-transfer coefficient. k is the effective reaction coefficient at the buried interface. C_1 is the AX concentration in the gas phase above the film. N is the molar amount of AX incorporated per unit volume of the perovskite product. t is the vapor-exposure time. For the ideal 1:1 conversion in Eq. (23), N can be estimated from the perovskite density and molar mass.

During the early stage of conversion, the product layer is thin. Gas-phase transport and interfacial reaction therefore have a strong influence on the conversion rate. As the product layer becomes thicker,

the d^2 term becomes increasingly important. The conversion then approaches diffusion-controlled behavior, and d increases approximately with the square root of time. Longer vapor exposure consequently produces progressively smaller thickness increments.

Eq. (24) also identifies the main process variables in two-step CVD. Reactor geometry, gas flow, and precursor supply affect h and C_1. Substrate temperature affects both the interfacial reaction coefficient k and the effective diffusivity D. The density, porosity, and grain-boundary structure of the converted perovskite can also change D. Increasing the vapor supply alone may therefore be insufficient when diffusion through the product layer becomes the main limitation.

The development of two-step CVD links early demonstrations of vapor conversion with later observations of the moving reaction front and control of the thermal cycle. Leyden et al. [66] reported an early two-step hybrid chemical vapor deposition (HCVD) process for PVSCs. It is classified here as a two-step CVD route because the metal-halide precursor film is deposited first and then converted into the perovskite by exposure to an organic-halide vapor. As shown in Fig. 11(a), MAI powder and substrates coated with a metal-halide precursor were placed in different temperature zones of a tube furnace. N_2 transported MAI vapor from the high-temperature source region to the lower-temperature substrate region, where it reacted with the predeposited $PbCl_2$ layer. The process produced continuous films and enabled planar devices with a PCE of 11.8%. The devices retained nearly the same efficiency after approximately 1,100 h of storage in dry N_2. The spatial progress of this conversion was later resolved by Moser et al. [67]. Fig. 11(b-d) shows cross-sectional SEM images and time-of-flight secondary-ion mass spectrometry profiles obtained at different conversion times. The inorganic precursor remained beneath the film surface at the beginning of the reaction. After 5 min, a perovskite layer had formed above the unconverted precursor, and full conversion was reached after 20 min. The

reaction front therefore moved from the outer surface toward the substrate. FAI had to diffuse through the growing perovskite layer to reach the buried interface, while Cs species diffused through the remaining PbI_2 in the opposite direction. These observations support the moving-front description in Eq. (24) and show why product-layer diffusion affects both conversion completeness and compositional uniformity.

Qiu et al. [68] extended two-step HCVD to Cs-FA mixed-cation perovskite modules. PbI_2 and CsBr were first co-evaporated onto patterned substrates and subsequently exposed to FAI vapor to form $Cs_{0.1}FA_{0.9}PbI_{2.9}Br_{0.1}$. As shown in Fig. 11(e), the yellow PbI_2/CsBr precursor film was converted into a dark-brown perovskite film over a 10 × 10 cm^2 substrate. Modules with a designated area of 91.8 cm^2 reached a PCE of 9.34%. In a separate stability test, encapsulated modules with a designated area of 22.4 cm^2 showed an extrapolated T_{80} lifetime of approximately 500 h under continuous one-sun illumination at 25 °C and steady-state power-output tracking. The same group subsequently shortened the thermal cycle through rapid hybrid chemical vapor deposition (RHCVD) [69]. The temperature profiles in Fig. 11(f) show that rapid heating and cooling reduced the total conversion time from several hours to less than 10 min. Rapid heating increased precursor delivery and initiated conversion within a short period, while rapid cooling limited further reaction and reduced the thermal exposure of the substrate and electron-transport layer. Modules with a designated area of 22.4 cm^2 reached a PCE of 12.3% and retained approximately 90% of their initial output after more than 800 h of continuous operation under illumination in dry N_2 (Fig. 11(g)).

These results place the main limitation of two-step CVD at the moving conversion front. Uniform vapor delivery controls the initial supply of the organic precursor, but the reaction progressively becomes more dependent on diffusion through the growing perovskite layer. The thermal cycle must

provide sufficient time for complete conversion without imposing unnecessary thermal exposure. Large-area processing therefore requires gas-phase delivery, product-layer diffusion, interfacial reaction, and thermal history to remain compatible across the entire substrate.

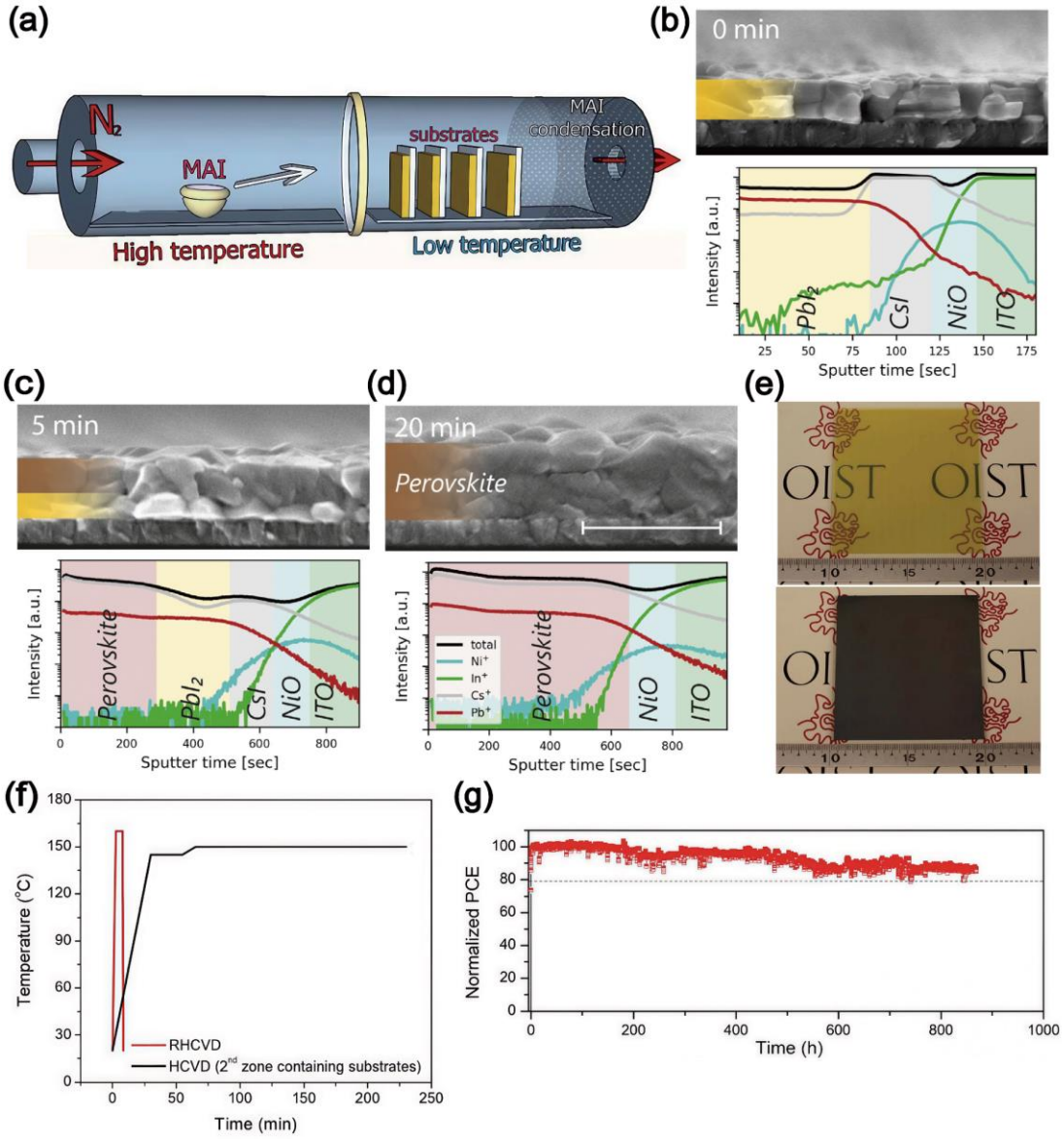

Fig. 11 (a) Schematic of a multi-zone hybrid chemical vapor deposition (HCVD) process in which MAI vapor is transported by N_2 from the high-temperature source region to metal-halide-coated substrates in a lower-temperature region. Reproduced from Ref. [66] under CC BY 3.0, © The Royal Society of Chemistry 2014. (b-d) Cross-sectional SEM images and time-of-flight secondary ion mass spectrometry (ToF-SIMS) depth profiles showing the conversion of a CsI/PbI_2 precursor after 0, 5, and

20 min of FAI vapor treatment, respectively. Reproduced from Ref. [67] under CC BY, © Moser, Feeney, Jones, and Small 2022. (e) Optical images of a PbI_2/CsBr precursor film and the converted $Cs_{0.1}FA_{0.9}PbI_{2.9}Br_{0.1}$ film on 10 × 10 cm^2 patterned substrates. Reproduced with permission from Ref. [68], © The Royal Society of Chemistry 2019. (f) Comparison of the substrate-temperature profiles during conventional HCVD and rapid hybrid chemical vapor deposition (RHCVD). (g) Continuous operation of an RHCVD module under illumination in dry N_2, showing retention of approximately 90% of the initial output after more than 800 h. Reproduced with permission from Ref. [69], © The Royal Society of Chemistry 2020.

4.2 Flux-controlled film growth in thermal evaporation

Whereas CVD relies on the coupled processes of precursor generation, carrier-gas transport, boundary-layer delivery, and surface reaction, thermal evaporation operates under a fundamentally different transport regime. Under high vacuum, precursor species travel from the source to the substrate through near-collisionless molecular transport, which largely suppresses carrier-gas-mediated convection and diffusion. Consequently, film growth is governed primarily by the generation, transport, spatial distribution, and incorporation of precursor fluxes rather than by gas-phase reaction and boundary-layer mass-transfer limitations.

From a physical perspective, thermal evaporation can therefore be viewed as a flux-controlled growth process. Film formation proceeds through four sequential steps: (i) precursor evaporation or sublimation at the source, (ii) molecular transport through the vacuum chamber, (iii) geometric redistribution of the emitted flux across the substrate, and (iv) incorporation of the arriving species into the growing solid through condensation, surface diffusion, reaction, and crystallization. The resulting film thickness and compositional uniformity depend on the coordinated balance among

source emission, chamber pressure, source-to-substrate geometry, and substrate-side incorporation kinetics.

Molecular transport requires the mean free path of the vapor species to be sufficiently long relative to the source-to-substrate distance. The mean free path can be estimated as:

$$\lambda = \frac{k_B T}{\sqrt{2}\pi p {d_m}^2} \tag{25}$$

where λ is the mean free path, k_B is the Boltzmann constant, T is the absolute temperature, p is the chamber pressure, and d_m is the effective molecular collision diameter. Eq. (25) shows that decreasing the chamber pressure increases the molecular mean free path. When λ becomes much larger than the source-to-substrate distance, evaporated species undergo few collisions before reaching the substrate, and transport approaches the molecular-beam regime. Under these conditions, precursor generation at the source can be described by the Knudsen-Langmuir and vapor-pressure relations in Eqs. (16) and (17). Once generated, however, the emitted flux is not distributed uniformly across the substrate. Even in the molecular-beam regime, differences in source-to-substrate distance, emission angle, and incidence angle produce position-dependent variations. The mapping of the source flux onto the substrate can therefore be expressed using a position-dependent geometric factor [70–72]:

$$J_i(\mathbf{x}) = J_{i,0} \cdot G_i(\mathbf{x}), \qquad G_i(x) \propto \frac{\cos^{n_i} \alpha_i\,(x) \cos \theta_i\,(x)}{r_i(x)^2} \tag{26}$$

where $J_{i,0}$ is a reference molar flux associated with source emission, and $G_i(\mathbf{x})$ describes its spatial redistribution across the substrate. The angles α_i and θ_i are measured relative to the source normal and substrate normal, respectively, while r_i is the distance from the source to position x. The exponent n_i describes the angular distribution of the emitted species. Its value is close to unity for an ideal cosine emitter, and larger values indicate a more directional distribution. Because $G_i(\mathbf{x})$ varies with position, a stable source flux can still produce a thickness gradient across a large substrate. Source

placement, substrate motion, and uniformity masks are therefore important for controlling the spatial distribution of the deposited material.

The incident flux is not necessarily equal to the amount incorporated into the film. Some arriving species are retained on the surface, whereas others desorb before entering the growing solid. A simple surface balance can be written as [73–75]:

$$J_{i,net}(x) = s_i J_i(x) - J_{i,des}(x) \tag{27}$$

where $J_{i,net}$ is the net incorporation flux, s_i is the initial sticking probability, and $J_{i,des}$ is the desorption flux. Both sticking and desorption depend on substrate temperature and surface composition. Differences among precursor species can cause the incorporated composition to deviate from the emitted source-flux ratio. Taken together, Eqs. (25)–(27) describe how source emission is converted into a position-dependent net incorporation flux at the substrate. Once the incorporated precursors form the target perovskite phase, the film-thickness growth rate follows the general mass-balance relation in Eq. (22), $\frac{dd}{dt} = \left(\frac{M_f}{\rho_f}\right) r_s$. In thermal evaporation, r_s is determined by the stoichiometric balance among the net precursor fluxes and by the selected deposition strategy. In single-source evaporation, several vapor species originate from one compound source, and their relative evaporation and incorporation determine both r_s and the deposited composition. In co-evaporation, independently controlled precursor fluxes arrive simultaneously, and the deficient precursor limits r_s once the required stoichiometric ratio is considered. In sequential evaporation, the deposited precursor inventory sets the maximum amount of product, while subsequent diffusion and reaction determine the time-dependent formation rate and extent of conversion. These three growth modes are discussed in the following sections.

4.2.1 Single-source flux deposition

Single-source evaporation supplies all perovskite-forming constituents from one pre-synthesized compound, usually in the form of a powder, pellet, or coating. Using one compound feed avoids the independent heating and calibration required for multiple precursor sources. This simpler source configuration, however, does not mean that only one vapor species is produced. Halide perovskites often undergo dissociative evaporation or sublimation. Several volatile species may therefore be released from the same source. These species can have different vapor pressures, sticking probabilities, and desorption rates. Source temperature controls their generation through the relations given in Eqs. (16) and (17). After transport through the vacuum chamber, their local incident fluxes are redistributed by the geometric factor in Eq. (26). Surface sticking and desorption then determine the net incorporation flux in Eq. (27). The target perovskite phase can form only when the incorporated species provide the required elemental ratios. Single-source evaporation therefore simplifies the deposition system, but film growth still depends on several coupled vapor fluxes.

The available process window is determined by both source stability and surface incorporation. A low source temperature may provide insufficient material, whereas excessive heating can accelerate decomposition or change the relative supply of volatile species. Substrate temperature must support surface diffusion and crystallization without causing excessive desorption of the organic halide. Because the individual vapor species cannot normally be adjusted independently during deposition, source preparation and thermal history become particularly important. Post-deposition annealing is also frequently required to complete phase formation. Over a large substrate, source-to-substrate geometry and substrate motion govern spatial uniformity. Temporal changes in source composition or evaporation rate can introduce an additional thickness or composition gradient.

The practical implications of these constraints are evident in the evolution of single-source

evaporation systems. Longo et al. [76] provided an early demonstration using flash evaporation. A $MAPbI_3$ precursor layer was deposited on tantalum foil and annealed to form a polycrystalline source. A high-current pulse then rapidly evaporated the complete source layer under vacuum. The deposited material reconstructed into crystalline $MAPbI_3$ and produced planar solar cells with a PCE of 12.2%. Because the material on the foil was consumed in each run, film thickness and repeatability depended on the initial amount and distribution of the source material. Liang et al. [77] subsequently used pre-synthesized $MAPbI_3$ powder in a conventional single-source thermal-evaporation system. The source and rotating-substrate arrangement is shown in Fig. 12(a). A continuous $MAPbI_3$ film was deposited over an area of 10 × 10 cm^2 (Fig. 12(b)). The approximately 500-nm-thick film was obtained within about 3 min and subsequently annealed at 140 °C. Measurements at different substrate positions showed similar crystallinity, composition, morphology, and thickness, while the Pb/I ratio remained close to the expected value. Devices fabricated from these films reached a PCE of 7.73% with little hysteresis. The result demonstrates the importance of stable source emission and substrate rotation when a single compound source is extended to a 100 cm^2 deposition area.

Abzieher et al. [78] addressed the batch nature of conventional single-source evaporation by developing continuous flash sublimation (CFS). As illustrated in Fig. 12(c), the precursor salts were converted into a perovskite source powder by mechanochemical synthesis and supplied to a preheated tantalum boat using a vibratory feeder. Each powder particle was rapidly sublimed before the next particle arrived. The feeding frequency controlled the material supply and therefore the deposition rate. Approximately 350-nm-thick $CsPb(I_xBr_{1-x})_3$ films were deposited within 2-5 min at rates ranging from 67 to 134 $nm \cdot min^{-1}$. Devices retained PCEs above 14% over much of this range (Fig. 12(d)), and the champion device reached 14.9%. Five consecutive deposition runs were completed without replacing

the source powder, with the relative photovoltaic parameters remaining within a narrow range (Fig. 12(e)). Separating powder storage from the heated evaporation zone thus enabled a replenishable source flux. Control at the source, however, does not by itself determine nucleation at the substrate. Yang et al. [79] deposited a 15-nm-thick CsCl seed layer before single-source thermal evaporation of a 400-nm-thick $FAPbI_3$ film. The absorber was deposited from one pre-synthesized compound source and then annealed at 150 °C. This process is better described as seed-assisted single-source evaporation than as sequential precursor evaporation because CsCl acts mainly as a heterogeneous nucleation layer. Cross-sectional images show that the seed layer reduced voids at the buried interface and promoted denser film growth (Fig. 12(f)). The corresponding p-i-n device reached a PCE of 20.26%, compared with 17.82% for the control device without the seed layer (Fig. 12(g)).

The progression from batch flash evaporation to continuous powder feeding shows that single-source processing can simplify equipment without eliminating flux-stability requirements. Source synthesis and feeding determine the temporal stability of the emitted material, whereas substrate motion and interfacial nucleation determine its spatial distribution and incorporation. Because the individual vapor species cannot normally be corrected independently during deposition, reproducible source preparation and thermal management remain particularly important during scale-up.

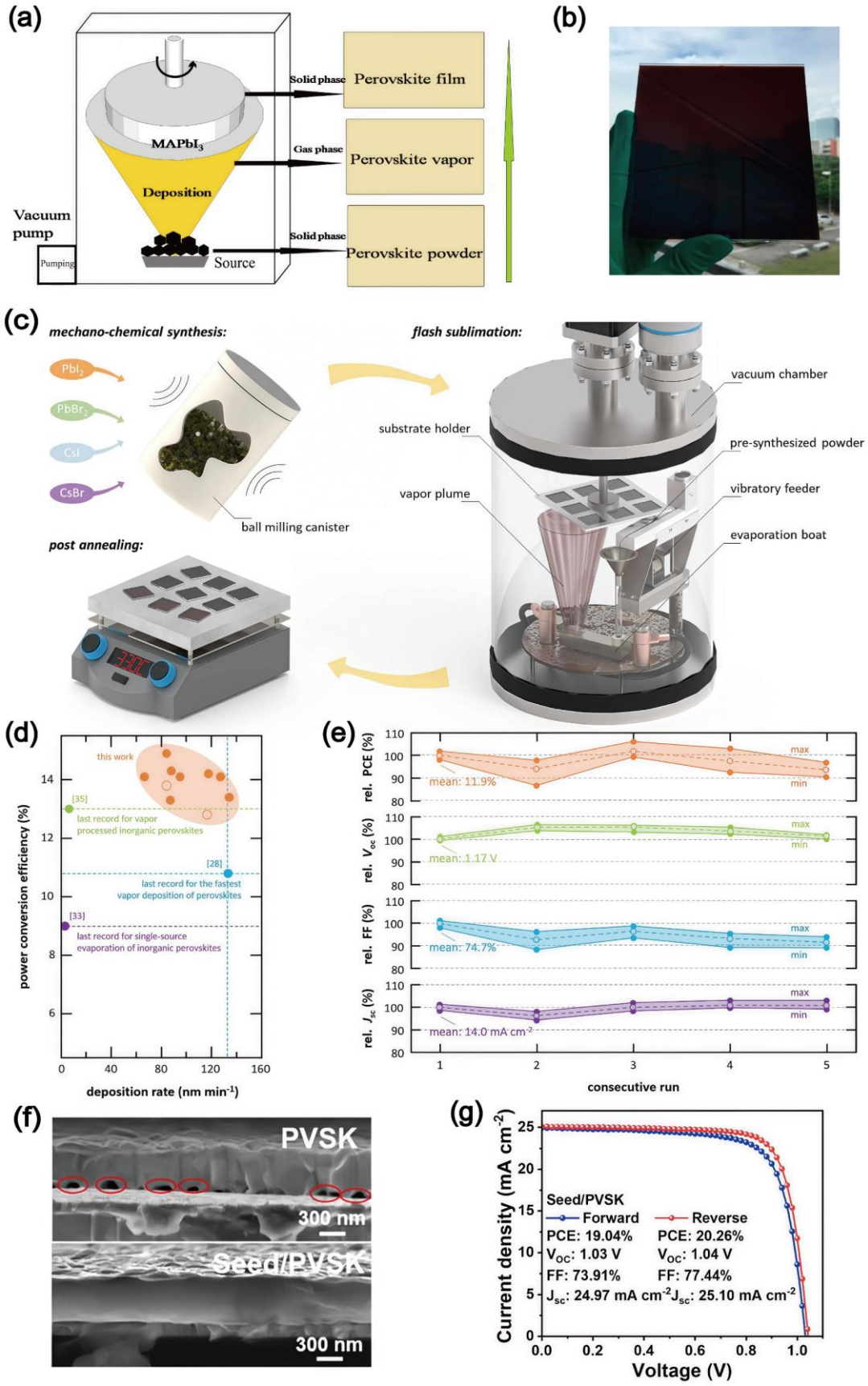

Fig. 12 (a) Schematic of single-source thermal evaporation using $MAPbI_3$ powder. (b) Photograph of

a 100 cm^2 $MAPbI_3$ film prepared by single-source thermal evaporation. Reproduced from Ref. [77] under CC BY 4.0, © The Authors 2018. (c) Schematic of continuous flash sublimation (CFS), including mechanochemical source preparation, continuous powder feeding, flash sublimation, and post-deposition annealing. (d) Relationship between deposition rate and device efficiency for CFS-processed inorganic perovskite absorbers. (e) Relative photovoltaic parameters obtained over five consecutive CFS deposition runs. Reproduced with permission from Ref. [78], © The Royal Society of Chemistry 2024. (f) Cross-sectional SEM images of $FAPbI_3$ films prepared without and with a CsCl seed layer, labeled PVSK and Seed/PVSK in the original figure, respectively. (g) Forward- and reverse-scan J-V curves of the champion Seed/PVSK device. Reproduced with permission from Ref. [79], © The Royal Society of Chemistry 2026.

4.2.2 Stoichiometry-controlled co-evaporation

Co-evaporation delivers different precursor vapors simultaneously from independently heated sources. The rate of each source can be adjusted separately, allowing the nominal precursor ratio to be tuned during deposition. This flexibility is particularly useful for multicomponent perovskites. Each precursor is still governed by the spatial flux distribution in Eq. (26) and the surface balance in Eq. (27). The specific challenge in co-evaporation is to match the resulting net incorporation fluxes at the substrate. For $MAPbI_3$ formation from MAI and PbI_2, their net molar fluxes should be approximately equal. A deficient precursor limits perovskite formation, while excess material may desorb or remain as a secondary phase.

During co-evaporation, the rate of each source is commonly monitored using a quartz crystal microbalance (QCM). These measurements are used to set the nominal precursor-flux ratio. However, a QCM records the material deposited at the sensor position rather than the net amount incorporated

into the film. The sensor and substrate differ in position, orientation, temperature, and surface properties. This difference is especially important for volatile organic salts, which can re-evaporate from a warm substrate. Each precursor therefore requires a tooling-factor calibration under the intended deposition conditions. Here, the tooling factor refers to the ratio between the thickness deposited on the substrate and that indicated by the QCM. For large substrates, the angular flux distributions from the different sources must also overlap. Substrate rotation, source placement, and uniformity masks are commonly used to control the local precursor ratio.

The distinction between nominal source control and actual incorporation at the substrate is illustrated by the following studies. Liu et al. [80] provided an early demonstration using separate MAI and $PbCl_2$ sources. The dual-source arrangement is shown in Fig. 13(a). Both materials were deposited simultaneously, allowing the $MAPbI_{3-x}Cl_x$ absorber to form directly on the substrate. The resulting planar heterojunction devices reached a PCE of 15.4%. Although this result established the feasibility of simultaneous vapor deposition, monitoring the two source rates did not determine whether the same precursor ratio was retained at the substrate. Roß et al. [81] examined this difference during the co-evaporation of $MAPbI_3$. Fig. 13(b) shows the tooling factors of MAI and PbI_2 at substrate temperatures from -30 to 60 °C. The PbI_2 tooling factor remained close to 30%-34%, whereas the MAI tooling factor decreased by more than 70% over the same range. The same nominal MAI/PbI_2 source-rate ratio could therefore produce different film compositions at different substrate temperatures. By adjusting the MAI supply, substrate temperature, and MeO-2PACz hole-transport layer, the authors obtained a stabilized PCE of 20.6%.

The process was subsequently extended to larger substrates and more complex precursor combinations. Ritzer et al. [82] prepared fully evaporated and laser-scribed modules by co-evaporating

PbI_2 and MAI at a substrate temperature of 25 °C. The photoluminescence map in Fig. 13(c) shows a relatively uniform absorber over a 64 cm^2 substrate, corresponding to a module aperture area of approximately 51 cm^2. The 51.1 cm^2 module contained 18 series-connected cell stripes, had a geometric fill factor of 94%, and reached PCEs of 16.6% and 16.5% in the reverse and forward scans, respectively (Fig. 13(d)). A smaller 4.0 cm^2 module reached 18.0%. Shen et al. [83] later applied multisource evaporation to wide-bandgap perovskites. The system used independently controlled FAI, PbI_2, $PbBr_2$, and CsI sources, together with a smaller $PbCl_2$ co-source (Fig. 13(e)). Replacing 5 mol% of the PbI_2 supply with $PbCl_2$ improved phase formation without requiring a separate seed layer. After annealing, the films developed a pronounced (100) face-up orientation instead of a random orientation (Fig. 13(f)). All-vacuum-deposited cells reached a laboratory PCE of 19.3% and a certified PCE of 18.35% over 0.25 cm^2, while 1 cm^2 cells reached 18.5%. Under the ISOS-L-2 light-soaking aging protocol, encapsulated 0.25 and 1 cm^2 champion cells showed T_{80} lifetimes of approximately 1,080 and 900 h, respectively. Aging was performed at open circuit under 0.76-sun full-spectrum illumination at 75 ± 5 °C in ambient air with 50%–60% relative humidity. The absorber was also integrated into 1 cm^2 perovskite–silicon tandem cells, which reached 27.2% with a solution-processed self-assembled monolayer and 24.3% in an all-vacuum configuration.

Co-evaporation provides direct control over the nominal supply from each source, but the incorporated composition also depends on substrate temperature, precursor retention, and the spatial overlap of the vapor fluxes. Adding more sources broadens the accessible composition range while increasing sensitivity to calibration error and source drift. During prolonged large-area deposition, composition feedback at the substrate is therefore more informative than source-rate monitoring alone.

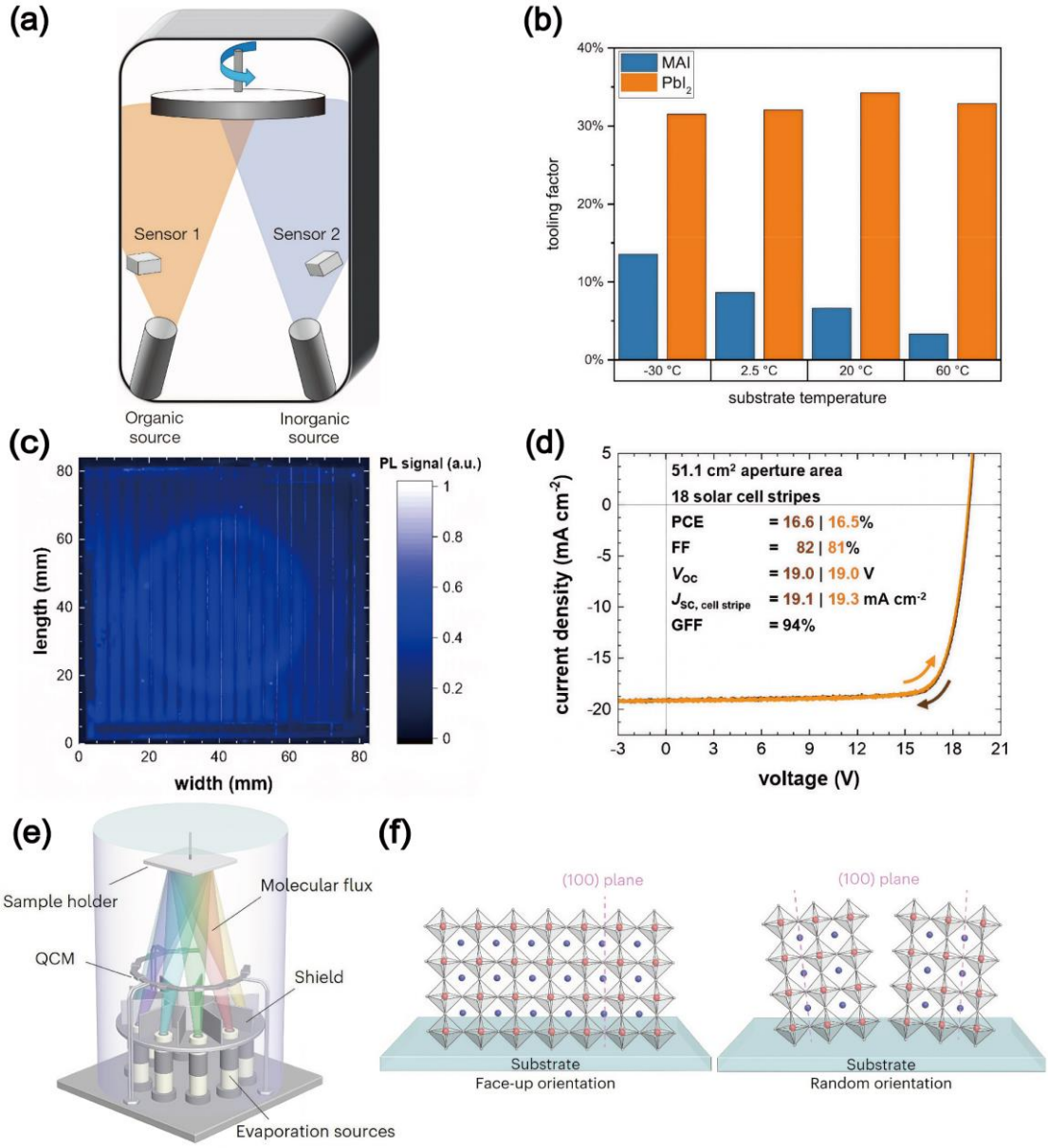

Fig. 13 (a) Dual-source vapor-deposition system with separate organic and inorganic sources. Reproduced with permission from Ref. [80], © Macmillan Publishers Limited 2013. (b) Tooling factors of MAI and PbI_2 as a function of substrate temperature, showing the stronger temperature dependence of MAI retention. Reproduced with permission from Ref. [81], © American Chemical Society 2020. (c) Photoluminescence map of a co-evaporated perovskite absorber deposited on a 64 cm^2 substrate. (d) Current density-voltage characteristics of an all-evaporated module with a 51.1 cm^2 aperture area and 18 interconnected cell stripes. Reproduced with permission from Ref. [82], © The

Authors 2021. (e) Multisource co-evaporation system with independently supplied precursors. (f) Schematic comparison of face-up and random orientations of the perovskite (100) crystal planes. Reproduced from Ref. [83] under CC BY 4.0, © The Author(s) 2026.

4.2.3 Sequential evaporation and post-conversion growth

Sequential evaporation separates precursor delivery from perovskite formation. Each precursor is deposited during a distinct step, and the resulting layers are subsequently converted by thermal treatment. Some perovskite may form when the precursor layers first contact each other. Complete conversion, however, usually requires later interdiffusion and reaction. This distinguishes sequential evaporation from co-evaporation, in which the precursors arrive simultaneously and the perovskite forms during deposition.

The first constraint is the amount of each precursor deposited per unit area. For precursor i, its areal molar amount can be calculated from the deposited thickness:

$$n_i = \frac{\rho_i h_i}{M_i} \tag{28}$$

where n_i is the areal molar amount, ρ_i is the density of the deposited precursor layer, h_i is its thickness, and M_i is its molar mass. For a reaction written as $\nu_A A + \nu_B B \rightarrow P$, the maximum amount of perovskite that can form is set by the limiting precursor [84]:

$$n_{P,max} = \min\left(\frac{n_A}{\nu_A}, \frac{n_B}{\nu_B}\right) \tag{29}$$

Eqs. (28) and (29) show that the precursor thicknesses already define the stoichiometric limit before annealing begins. A deficient layer restricts the final amount of perovskite, whereas an excess layer can remain as a secondary phase or be lost during heating. Once conversion is complete, the corresponding film thickness follows the mass-balance relation in Eq. (22). Longer annealing can improve conversion, but it cannot compensate for an incorrect precursor inventory.

The second constraint is solid-state transport during post-conversion. In a simple bilayer structure, the more mobile precursor must pass through the product layer to reach the remaining reactant. The characteristic diffusion length of species i can be estimated as [85]:

$$L_D \sim \sqrt{2D_i t} \tag{30}$$

where D_i is the effective diffusion coefficient and t is the conversion time. Full conversion becomes difficult when L_D, i is smaller than the required transport distance. This distance is influenced by the thickness of each precursor layer, the density of the inorganic film, and the grain-boundary structure of the growing perovskite. Repeating thinner precursor stacks can shorten the diffusion path, even when the total deposited amount remains unchanged.

The diffusion coefficient depends strongly on temperature and can be expressed using an Arrhenius relation [86]:

$$D_i = D_{0,i} \exp\left(-\frac{E_{D,i}}{RT}\right) \tag{31}$$

where $D_{0,i}$ is the pre-exponential factor, $E_{D,i}$ is the activation energy for diffusion, R is the gas constant, and T is the absolute temperature. Increasing the annealing temperature can accelerate interdiffusion and shorten the conversion time. The useful temperature range is nevertheless limited. Insufficient heating leaves unreacted precursor, whereas excessive heating can promote organic-halide loss, perovskite decomposition, or void formation. Large-area processing therefore requires both a uniform precursor inventory and a uniform thermal history.

Previous studies show how the conversion window is shaped by both thermal history and the structure of the precursor stack. Chen et al. [87] deposited $PbCl_2$ first and then MAI at substrate temperatures between 65 and 85 °C. At 65 °C, the reaction did not extend through the complete $PbCl_2$ layer. Raising the temperature to 75 °C produced continuous $MAPbI_{3-x}Cl_x$ films with fused crystalline

domains, whereas further heating to 85 °C reduced crystalline quality despite the apparently complete surface coverage. Devices prepared at 75 °C reached a PCE of 15.4%, with an average value of approximately 14%. Maintaining this temperature window becomes more difficult as the deposition area increases. Feng et al. [88] sequentially deposited PbI_2, FAI, and CsI before in-vacuum annealing (Fig. 14(a)). The process produced FA-based perovskite films on 400 cm^2 glass substrates and 300 cm^2 flexible PET substrates (Fig. 14(b)). Annealing at 45 °C left incompletely converted material near the bottom of the film. A temperature of 60 °C promoted conversion throughout the precursor stack and produced compact grains, while 80 °C caused FAI loss, partial decomposition, cracks, and pinholes. The optimized process yielded small-area devices with a PCE of 21.32%. Increasing the deposition area therefore did not remove the conversion constraint but made temperature uniformity across the substrate more important.

The diffusion pathway can also be modified through the precursor structure. Li et al. [89] first co-evaporated PbI_2, $PbCl_2$, and CsI to form a Cl-containing inorganic layer and then deposited FAI in a separate step (Fig. 14(c)). Chloride modified the crystallinity and orientation of the lead-halide precursor, promoted FAI diffusion during annealing, and accelerated conversion to $Cs_{0.05}FA_{0.95}PbI_3$. The resulting films were compact and pinhole-free. Devices with aperture areas of 0.1 and 1 cm^2 reached PCEs of 24.42% and 23.44%, respectively, while a 14.4 cm^2 mini-module reached 19.87% (Fig. 14(d)). Schulz et al. [90] subsequently examined the diffusion step quantitatively by sequentially depositing PbI_2 and FAI and monitoring $FAPbI_3$ formation using in situ X-ray diffraction (XRD). Increasing the nominal annealing temperature from 90 to 120 °C reduced the approximate conversion time from 200 to 50 min (Fig. 14(e)). Fitting the phase evolution with a diffusion model produced diffusion coefficients that followed an Arrhenius relation, with an activation energy of 0.84 ± 0.18 eV

(Fig. 14(f)). These measurements connect the temperature dependence in Eq. (31) with the conversion of an actual sequentially deposited precursor stack. Sequential evaporation relocates the main growth-control problem from simultaneous flux matching to precursor inventory and post-deposition conversion. Uniform layer thickness is insufficient if the precursor structure, diffusion distance, or substrate temperature varies across the deposition area. These variables must therefore be coordinated within the same conversion window.

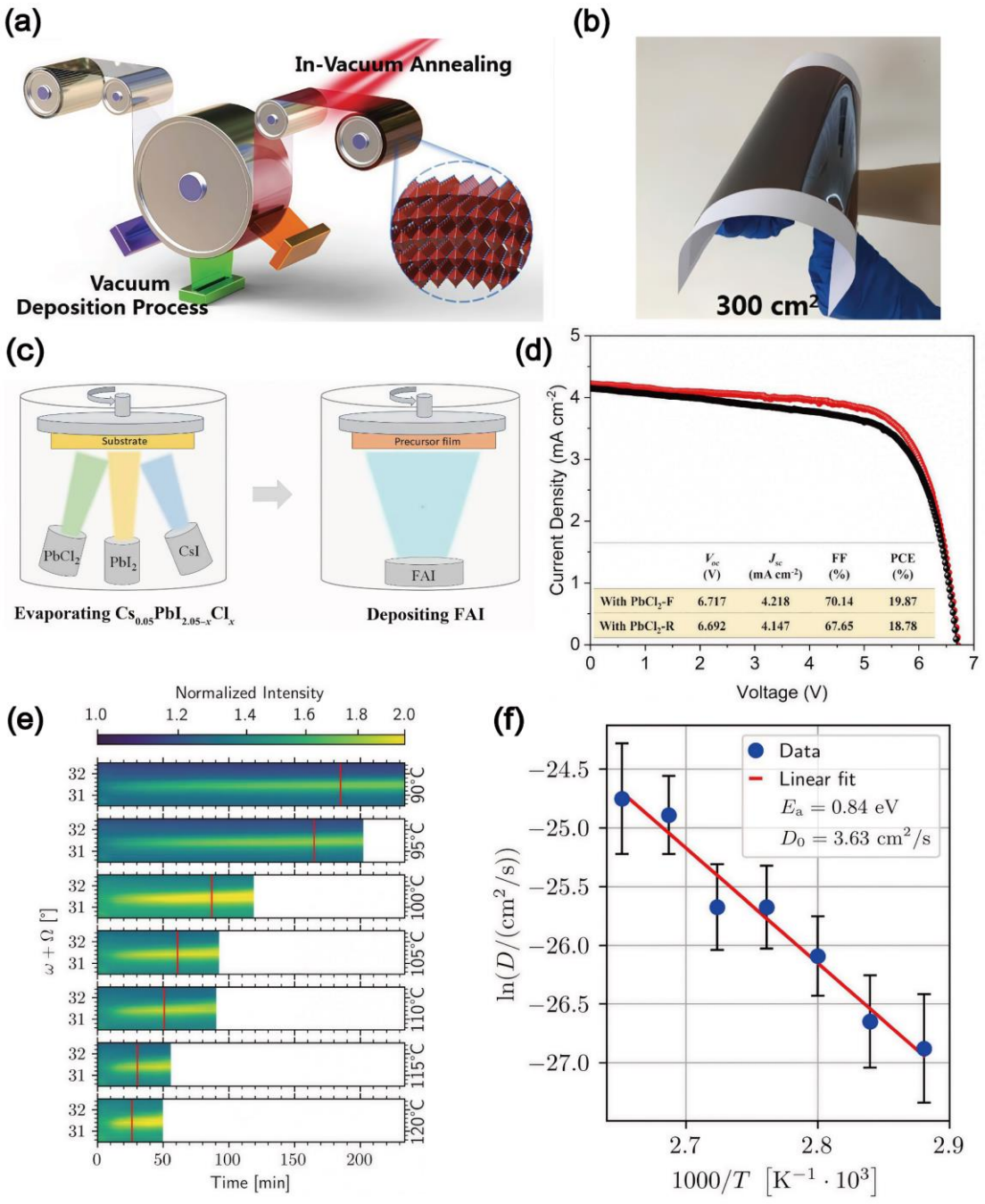

Fig. 14 (a) Schematic illustration of multisource vacuum deposition followed by in-vacuum annealing. (b) Photograph of a FA-based perovskite film deposited on a 300 cm^2 flexible PET substrate. Reproduced with permission from Ref. [88], © The Royal Society of Chemistry 2021. (c) Schematic of Cl-containing alloy-mediated sequential vacuum evaporation, in which the inorganic precursor film is deposited before FAI. (d) Current density–voltage characteristics of a mini-module with an aperture area of 14.4 cm^2. F and R denote the forward and reverse scans, respectively. Reproduced with permission from Ref. [89], © The Authors 2022. (e) In situ XRD maps showing the conversion of a PbI_2/FAI stack at different annealing temperatures. The red lines mark the fitted conversion end time. (f) Arrhenius plot of the extracted FAI diffusion coefficients, giving an activation energy of 0.84 eV. Reproduced with permission from Ref. [90], © the Owner Societies 2026.

4.3 Non-equilibrium film growth in energy-assisted vapor deposition

Unlike CVD and thermal evaporation, where film growth is governed primarily by precursor transport, reaction kinetics, or flux delivery, energy-assisted vapor-deposition techniques introduce an additional degree of freedom: energetic species that actively modify precursor generation, transport, and surface incorporation. As a result, film formation is no longer determined solely by mass transfer and stoichiometric flux balance, but also by the transfer of kinetic, plasma, or photon energy into the growing film.

The introduction of external energy drives the deposition process further from thermodynamic equilibrium and fundamentally alters the growth pathway. Energetic species can enhance nucleation density, increase adatom mobility, promote film densification, and expand the processing window for low-temperature deposition. At the same time, excessive energy input may induce non-ideal effects, including re-sputtering, ion-induced damage, preferential loss of volatile components, defect

generation, and partial decomposition of the perovskite phase. Consequently, the central challenge in energy-assisted deposition is not only achieving sufficient precursor supply, but also balancing energy delivery and material incorporation to maintain stoichiometry, phase purity, and film integrity.

From a growth-kinetics perspective, these methods can be distinguished by how external energy is introduced into the deposition process. In sputtering, momentum transfer from energetic plasma species governs target erosion and influences film growth through ion-assisted deposition. In electron-beam evaporation, highly localized electron-beam heating generates intense and controllable vapor fluxes, while also introducing non-equilibrium evaporation behavior for multicomponent materials. In PLD, short laser pulses ablate the target surface and generate a highly energetic transient plume whose dynamics directly determine film composition and growth. Although their hardware implementations differ substantially, all three approaches share the common feature that precursor incorporation is strongly coupled to externally supplied energy. The following sections discuss sputtering, electron-beam evaporation, and PLD from the perspective of energy-assisted non-equilibrium film growth and its implications for scalable perovskite-film fabrication.

4.3.1 Sputtering

Sputtering is distinguished from thermal evaporation by its plasma-assisted precursor-generation mechanism. A low-pressure plasma, usually sustained in Ar, supplies positive ions that are accelerated toward a solid target. Momentum transfer at the target surface ejects atoms, molecules, and clusters, which then travel through the working gas and reach the substrate. In radio-frequency (RF) magnetron sputtering, a magnetic field confines electrons near the target and increases the ionization efficiency. Because the precursor flux is generated by ion bombardment rather than thermal sublimation or evaporation, sputtering is classified as an energy-assisted deposition method. This energetic

environment can produce dense and conformal coatings, but it can also cause plasma damage, re-sputtering, preferential loss of volatile components, and stoichiometric deviation. These effects are particularly important for metal-halide perovskites.

For perovskite fabrication, sputtering is commonly implemented through two routes. In direct compound-target sputtering, a composite target contains all the components required for the perovskite, although post-deposition annealing may still be needed to establish the final composition and phase. In conversion-based sputtering, an inorganic precursor layer is deposited first and subsequently converted into the perovskite through a vapor or solution treatment, analogous to the conversion strategy used in two-step CVD. The latter route should be distinguished from direct perovskite sputtering because the perovskite phase forms mainly after the plasma-deposition step.

The source flux is controlled by the incident ion supply and the sputtering response of each target component. If j_i is the ion current density, the molar flux of species g leaving the target can be approximated as [91–93]:

$$\Phi_{g,0} = \frac{j_i}{zeN_A} Y_g(E_i, \alpha) \tag{32}$$

where z is the ion charge state, e is the elementary charge, and N_A is Avogadro's constant. The sputtering yield $Y_g(E_i, \alpha)$ gives the number of species g ejected per incident ion. It depends on the ion energy E_i, incidence angle α, and target properties. Eq. (32) separates the ion supply from the response of the target. Increasing RF power commonly changes both j_i and E_i, but the relationship depends on the plasma and sheath conditions. It should not be treated as a universal linear relationship between RF power and deposition rate. Different target components can also have different sputtering yields. The emitted composition may therefore deviate from the target composition before gas-phase transport begins.

After leaving the target, the sputtered species are scattered by the working gas and distributed across the substrate. A reduced net-incorporation balance can be written as [94]:

$$\Gamma_g^{net}(x) = s_g(T_s)\,\Phi_{g,0} G_g(x) \exp\left[-\frac{L(x)}{\lambda_g}\right] - r_{\mathrm{des},g}(T_s) - r_{\mathrm{rs},g}(V_b) \tag{33}$$

where $\Gamma_g^{net}(x)$ is the net molar incorporation flux of species g at position x, T_s is the substrate temperature, and V_b is the substrate-bias voltage. $G_g(x)$ is the geometric distribution factor, $L(x)$ is the transport distance, and λ_g is the mean free path of species g. The sticking coefficient s_g describes the fraction of arriving species retained at the surface, while $r_{\mathrm{des},g}(T_s)$ and $r_{\mathrm{rs},g}(V_b)$ represent the desorption and re-sputtering fluxes, respectively. The mean-free-path and geometric terms correspond to the general relations in Eqs. (25) and (26). Eq. (33) extends the surface balance in Eq. (27) by including re-sputtering. Increasing the working pressure strengthens gas-phase scattering and can broaden the lateral flux distribution, but it also reduces the direct arriving flux. A substrate bias or an intense energetic-particle flux can increase re-sputtering and aggravate the loss of volatile components.

For large-area deposition, spatial and temporal uniformity must be considered together. Target-to-substrate geometry, working pressure, and substrate motion determine the lateral distribution of the arriving flux. Target erosion, composition changes, and mechanical degradation alter the source flux during repeated operation. A high deposition rate does not necessarily indicate stable composition. Process optimization must therefore consider film composition and target condition in addition to thickness uniformity.

Reported studies show that film composition can change at several stages, from target erosion and transport to post-deposition annealing and subsequent device-stack integration. Raifuku et al. [95] first deposited PbI_2 by sputtering and then converted it into $MAPbI_3$ in MAI vapor. Direct sputtering from

a perovskite target was also examined, but the resulting film contained residual PbI_2. The converted films provided conformal coverage on rough substrates and produced solar cells with a reverse-scan PCE of 1.84%. Direct compound-target sputtering became more effective when post-deposition phase evolution was incorporated into the process. Gao et al. [96] prepared mechanosynthesized MABr-containing $FAPbI_3$-based targets for magnetron sputtering. The as-sputtered films contained mixed phases and excess organoammonium halides. During annealing, a bromide-rich intermediate formed before transformation into a continuous $FAPbI_3$-dominated layer (Fig. 15(a)). Selective loss of volatile components accompanied this solid-state phase transition, so the deposited film did not preserve the target composition unchanged. After optimization, the champion device reached a PCE of 20.1% (Fig. 15(b)), while a device with an active area of 49 mm^2 reached 16.2%. Annealing therefore determined not only crystallinity but also the final composition and phase.

Energetic-particle damage also becomes important when functional layers are sputtered onto an existing perovskite surface. Peng et al. [97] deposited the main functional layers of an inverted device by magnetron sputtering (Fig. 15(c)). Before SnO_2 deposition, a 6-nm buffer composed of poly(methyl methacrylate) (PMMA) and [6,6]-phenyl-C61-butyric acid methyl ester (PCBM) was spin-coated onto the perovskite. Time-of-flight secondary ion mass spectrometry (ToF-SIMS) showed extensive Sn penetration without the buffer layer (Fig. 15(d)), whereas the buffer delayed Sn penetration and shortened the Sn-Pb mixed region (Fig. 15(e)). Devices containing a sputtered $MAPbI_3$ absorber and sputtered inorganic transport layers reached a PCE of 14.62%. In a separate device configuration using a solution-deposited perovskite absorber, devices containing the sputtered transport layers and PMMA/PCBM buffer retained 93.5% of their initial efficiency after storage in N_2 for 2,000 h. Since the buffer layer was spin-coated, this structure should not be described as a completely dry-processed

device. Its main relevance here is the control of sputtering damage during device-stack integration. Repeated operation introduces a different limitation at the target. Laxmi et al. [98] systematically examined target stoichiometry, RF power, and Ar pressure. A nominally stoichiometric target produced a PbI_2-rich film, indicating substantial loss of organic components. Perovskite formation required targets containing excess FAI, as shown by the thin-film XRD patterns in Fig. 15(f). The resulting films nevertheless contained excess iodine or degraded organic species and showed poor microstructure. The FAI-rich targets also developed cracks and holes during sputtering (Fig. 15(g)). Increasing the organic content of the target can therefore assist phase formation while reducing its mechanical stability and reusability.

Taken together, these results distinguish thickness control from composition control in sputtering. Increasing the ion supply may raise the emitted flux in Eq. (32), but it can also intensify selective loss and re-sputtering in Eq. (33). Film-composition measurements should therefore be combined with monitoring of target evolution, particularly during repeated deposition. A uniform thickness profile does not guarantee that the film composition remains uniform across the substrate or between successive runs.

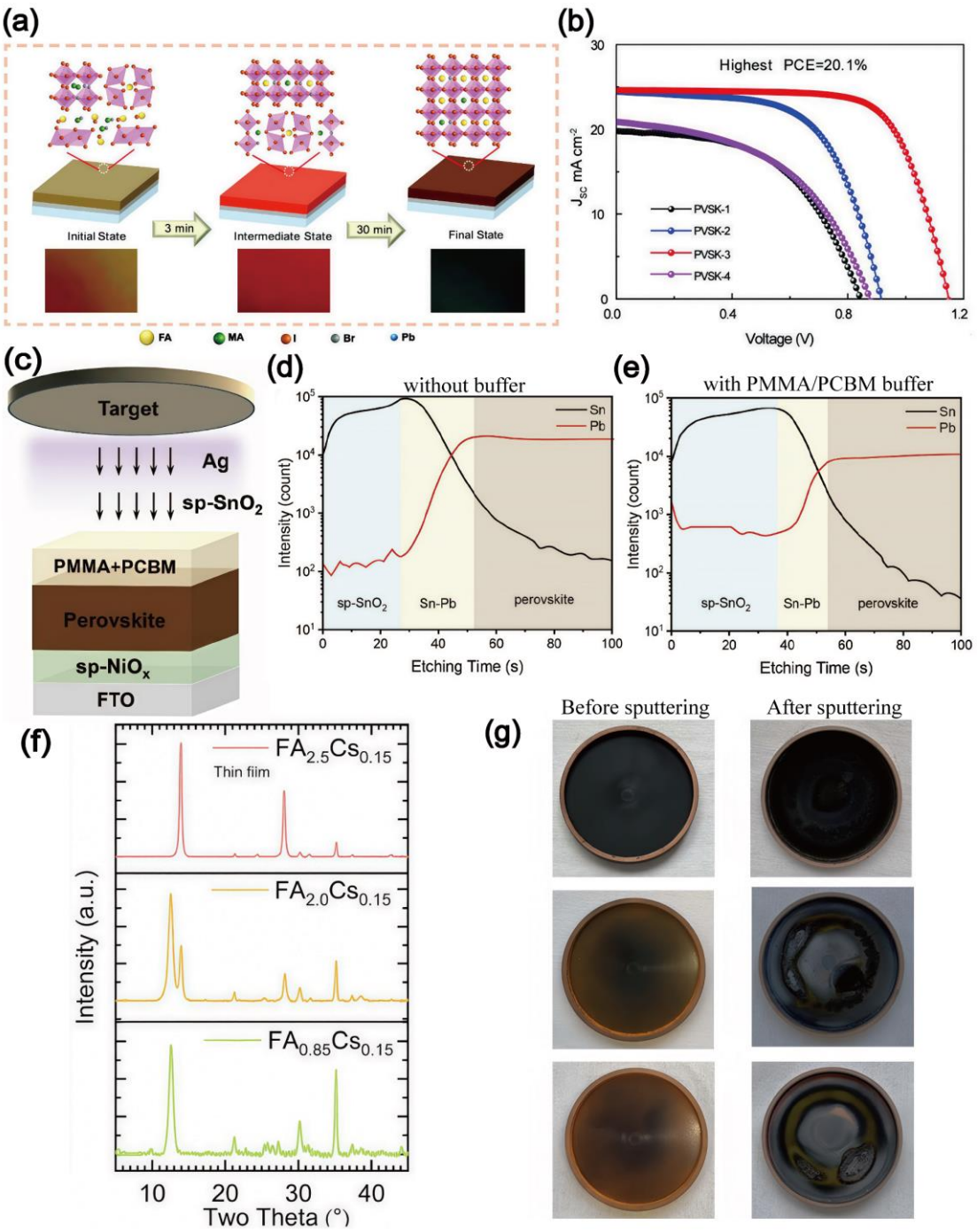

Fig. 15 (a) Solid-state compositional and phase evolution of a sputtered MABr-containing $FAPbI_3$-based film during thermal annealing. (b) Current density–voltage characteristics of devices prepared from sputtered films with different precursor compositions. Reproduced with permission from Ref. [96], © Wiley-VCH GmbH 2024. (c) Device structure and fabrication sequence using sputtered NiO_x, perovskite, SnO_2, and Ag layers together with a spin-coated PMMA/PCBM buffer. (d, e) ToF-SIMS

depth profiles obtained without and with the PMMA/PCBM buffer, respectively. Reproduced with permission from Ref. [97], © American Chemical Society 2023. (f) XRD patterns of films sputtered from targets with different FAI contents. (g) Photographs of targets before and after sputtering. The left and right columns show the targets before and after sputtering, respectively. The rows from top to bottom correspond to $FA_{0.85}Cs_{0.15}$, $FA_{2.0}Cs_{0.15}$, and $FA_{2.5}Cs_{0.15}$ target compositions. Reproduced from Ref. [98] under CC BY 4.0, © The Author(s) 2026.

4.3.2 Electron-beam evaporation

Electron-beam evaporation differs from sputtering in where the external energy enters the process. In sputtering, energetic ions eject material from the target and may also reach the growing film. In electron-beam evaporation, the primary electron beam is directed at the source. Its energy is converted into localized heating, which causes the source material to evaporate under high vacuum. The vapor then travels to the substrate mainly as neutral species. The downstream transport is therefore closer to thermal evaporation than to sputtering. Electron-beam evaporation is energy-assisted at the source rather than at the growing surface.

The source output is governed by the energy delivered to the beam spot. The mean absorbed beam-power density can be expressed as:

$$q_b = \frac{P_{abs}}{A_{spot}} = \frac{\eta V_{acc} I_b}{A_{spot}} \tag{34}$$

where q_b is the mean absorbed beam-power density, P_{abs} is the power absorbed by the source, and A_{spot} is the effective beam-spot area. The factor η represents the fraction of the electrical beam power absorbed by the source. V_{acc} and I_b are the acceleration voltage and beam current, respectively. At the same electrical power, a smaller beam spot provides a higher local energy input. Eq. (34), however, does not directly give the source temperature or evaporation rate. Part of the

absorbed power drives evaporation, while the remainder is lost through radiation and heat conduction to the crucible. Beam scanning and changes in the source surface also redistribute the local energy input.

Once the source temperature is established, vapor generation follows the saturation-vapor-pressure and source-flux relations in Eqs. (17) and (16), respectively. Transport through the high-vacuum chamber and incorporation at the substrate can then be described using Eqs. (25)–(27). The strong local heating also creates a narrow processing window for compound sources. Different components may evaporate at different rates, so the vapor composition does not necessarily reproduce the source composition. Excessive beam-power density can promote source decomposition, spitting, and preferential loss of volatile halides. The vapor flux may also change as the beam moves across the source or as the source level falls. These effects are particularly restrictive for hybrid perovskites because organic components are thermally unstable. Direct deposition has therefore been demonstrated mainly for inorganic compositions. Post-deposition annealing is usually required to improve crystallinity and complete phase reconstruction.

The limited literature on direct electron-beam deposition has so far concentrated on $CsPbBr_3$ and the phase reconstruction required after deposition. Liu et al. [99] used single-source electron-beam evaporation to prepare $CsPbBr_3$ absorbers. A CsBr-rich source was prepared from CsBr and $PbBr_2$ at a molar ratio of 2:1 and thermally treated before deposition (Fig. 16(a)). The source contained $CsPbBr_3$ together with Cs_4PbBr_6 and reduced the formation of the Pb-rich $CsPb_2Br_5$ phase. Films were deposited at room temperature under high vacuum and subsequently annealed. The as-deposited film showed continuous coverage but consisted of small grains (Fig. 16(b)). Annealing at 350 °C for 10 min produced much larger grains while maintaining dense coverage (Fig. 16(c)). The corresponding device

reached a PCE of 7.81% over an active area of 0.06 cm^2 (Fig. 16(d)). He et al. [100] later introduced a water-vapor treatment (WVT) between electron-beam deposition and thermal annealing. Water molecules temporarily dissolved and redistributed CsBr at the film surface and grain boundaries. The enlarged XRD region in Fig. 16(e) shows that the Cs_4PbBr_6-related peak was suppressed after short treatment but increased again at longer treatment times. As illustrated schematically in Fig. 16(f), short exposure promoted the conversion of Cs_4PbBr_6 to $CsPbBr_3$, whereas prolonged exposure removed more CsBr and favoured $CsPb_2Br_5$ formation. A 3 s treatment provided the best balance between phase reconstruction and subsequent grain growth, increasing the device PCE from 2.13% to 7.45%. WVT is therefore part of the post-deposition crystallization sequence rather than a separate electron-beam deposition mechanism. Evidence for direct electron-beam evaporation of perovskite absorbers remains limited to small-area $CsPbBr_3$ devices. Lateral film uniformity and module-scale operation have not yet been demonstrated. Changes in the compound source during prolonged beam exposure also remain an important uncertainty. The central challenge is maintaining sufficiently congruent material transfer to provide a reproducible starting film for the subsequent phase-reconstruction process.

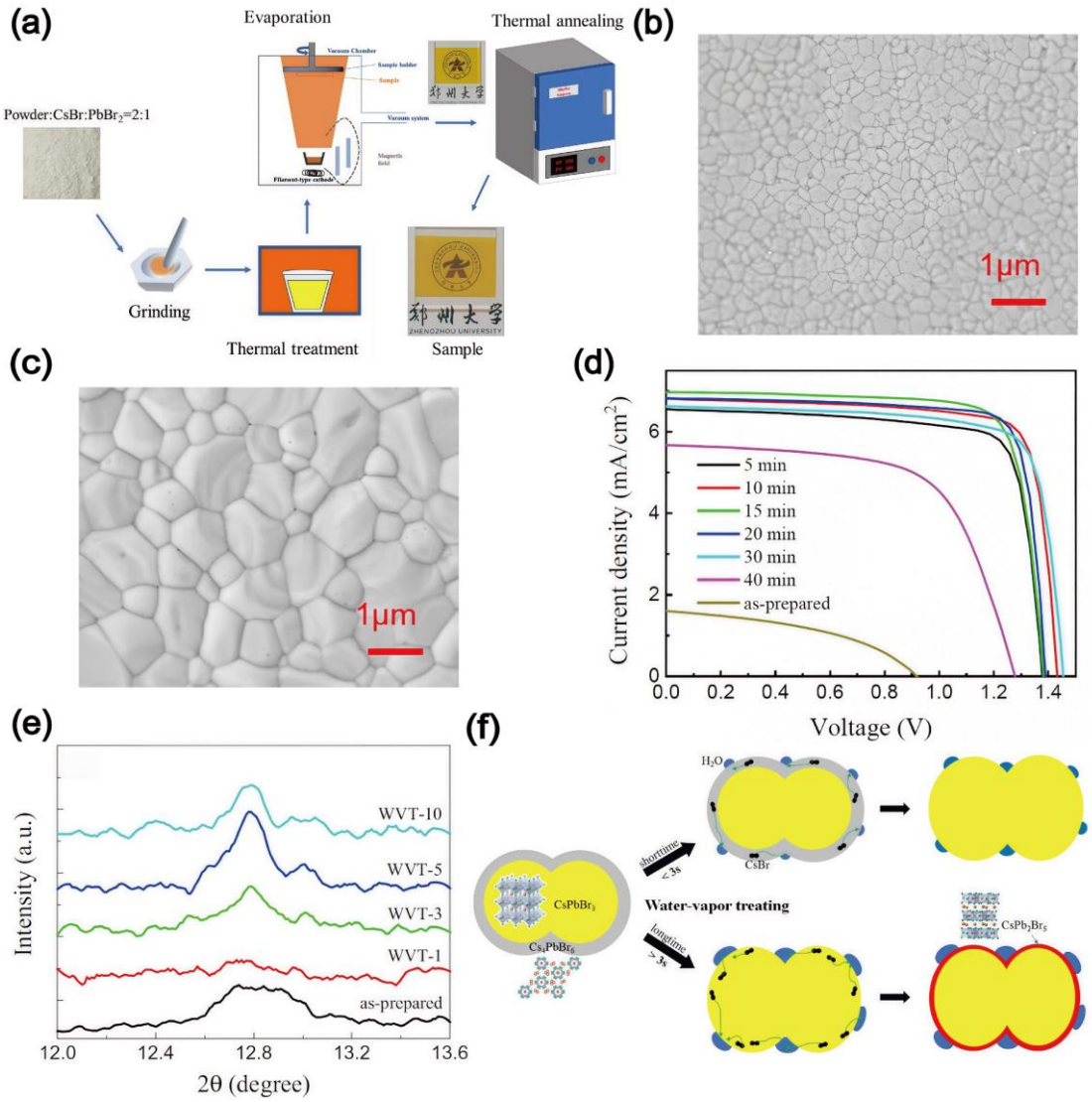

Fig. 16 (a) Preparation of the compound source, single-source electron-beam evaporation, and thermal annealing. (b, c) Top-view SEM images of the as-deposited film and the film annealed at 350 °C for 10 min, respectively. (d) J-V curves of devices based on films annealed at 350 °C for different times. Reproduced with permission from Ref. [99], © International Solar Energy Society 2022. (e) Enlarged XRD region showing the Cs_4PbBr_6-related diffraction peak after different water-vapor treatment (WVT) times and subsequent annealing. (f) Schematic of CsBr redistribution and the associated phase evolution during short and prolonged WVT. Reproduced with permission from Ref. [100], © The Author(s) 2023.

4.3.3 Pulsed laser deposition (PLD)

PLD generates the precursor supply by coupling short laser pulses into a solid target. Each pulse rapidly heats and ablates a small region of the target surface. The ejected atoms, molecules, ions, clusters, and particles form a transient plume and travel toward the substrate. This source mechanism differs from the continuous heating used in thermal and electron-beam evaporation. It can transfer several target components within a single pulse and is therefore attractive for depositing multicomponent perovskites from one source. However, target-to-film composition transfer is not necessarily congruent. Organic and halide components can be lost during ablation or plume transport. Energetic particles and droplets may also damage the growing surface or produce local defects.

The incident laser fluence is the primary parameter used to describe the energy delivered to the target [101]:

$$F = \frac{E_{pulse}}{A_{spot}} \tag{35}$$

where E_{pulse} is the energy of one laser pulse and A_{spot} is the irradiated area on the target. Fluence is more informative than pulse energy alone because a change in beam focusing changes the energy density even when the pulse energy remains constant. The ablation threshold depends on the target material, laser wavelength, pulse duration, and surface condition [102,103]. Below this threshold, material removal is limited. Excessive fluence can intensify target melting, preferential loss of volatile species, and the ejection of large particles. A suitable operating window must therefore provide a stable plume without imposing excessive energy on either the target or the growing film.

Laser fluence describes the energy delivered by each pulse, whereas the repetition rate determines how often the target is irradiated. At a fixed fluence, increasing the repetition rate usually raises the time-averaged material supply and shortens the deposition time. The total pulse number is commonly used to control the nominal film thickness [104]. These relationships remain valid only when the

amount removed by each pulse is stable. Target heating, crater formation, surface-composition changes, and mechanical degradation can alter the ablation yield during a long deposition. Target rotation or scanning is therefore used to distribute laser exposure and maintain a more reproducible source flux.

After leaving the target, the plume may travel ballistically under high vacuum or undergo collisions in a background gas. Increasing the gas pressure can broaden and thermalize the plume. This reduces the kinetic energy of species arriving at the substrate, but it can also decrease the deposition efficiency. Target-to-substrate distance, plume direction, and substrate motion determine the lateral flux distribution. The geometric and mean-free-path terms in Eqs. (25) and (26) provide a qualitative description of these effects, although a transient PLD plume cannot be represented fully by a steady molecular flux. Surface incorporation can still be considered using the net-flux balance in Eq. (27), although both the plume flux and the resulting growth rate are time dependent. These factors govern the stability and spatial overlap of successive plumes during deposition.

Experiments on hybrid and inorganic perovskites reveal that target-to-film transfer depends on more than the nominal target composition. Plume geometry, pulse frequency, and the physical state of the target can all change the material that reaches and remains on the substrate. Bansode et al. [105] compared conventional on-axis deposition with an off-axis arrangement (Fig. 17(a)). Direct plume impingement from a stoichiometric target produced a PbI_2-rich film because of preferential loss of iodine and organic components. The off-axis arrangement reduced the impact of high-energy species and improved retention of the volatile components, although the target composition still required adjustment. A PbI_2:MAI molar ratio of 1:4 produced a nearly stoichiometric $MAPbI_3$ film at room temperature, whereas a stoichiometric target did not. Devices prepared using this process reached a PCE of approximately 7.7%. The same composition-transfer problem was later addressed in the more

complex $MA_{1-x}FA_xPbI_3$ system. Soto-Montero et al. [106] adjusted the organic-to-inorganic and MA-to-FA ratios in targets containing MAI, FAI, PbI_2, and $PbCl_2$ to compensate for differences in ablation and incorporation. Introducing 20 mol% $PbCl_2$ into the lead-halide fraction improved film compactness and increased device efficiency by about one absolute percentage point. Subsequent oleylammonium iodide (OAmI) surface treatment reduced nonradiative recombination and produced a PCE of 19.7% (Fig. 17(b)). Because this highest efficiency also depended on solution-based surface passivation, it should not be attributed to PLD growth alone.

Deposition throughput introduces another trade-off. Kliner et al. [107] increased the laser repetition rate from 4 to 40 Hz and raised the $MA_{1-x}FA_xPbI_3$ deposition rate from 6 to 80 $nm \cdot min^{-1}$. The deposition time for a 400-nm film over a 2.5 × 2.5 cm^2 area decreased from approximately 75 to 5 min. In situ photoluminescence measurements indicated that the main stages of nucleation and grain coalescence remained similar across this rate range, but the final material quality was rate dependent. Rapidly deposited films showed reduced preferred orientation and lower crystallinity. The time-resolved microwave conductivity (TRMC) results in Fig. 17(c,d) show that the carrier-mobility sum decreased from approximately 3 to 1 $cm^2 \cdot V^{-1} \cdot s^{-1}$ as the deposition rate increased from 6 to 80 $nm \cdot min^{-1}$. Adding $PbCl_2$ to the target increased the TRMC response by approximately 20% at both deposition rates but did not fully compensate for the loss associated with rapid growth.

All-inorganic $CsPbBr_3$ avoids organic-cation loss but remains sensitive to the source and target structure. Wang et al. [108] deposited $CsPbBr_3$ into a mesoporous TiO_2 scaffold from a single $CsPbBr_3$ target. Post-treatment produced crystalline films with relatively uniform elemental distributions, and the resulting devices reached a PCE of 6.3%. More recently, Fan et al. [109] compared a conventional powder-pressed target with a melt-quenched $CsPbBr_3$ target. The powder-pressed target contained

many internal voids, whereas the melt-quenched target was dense and relatively uniform (Fig. 17(e)). Its measured density was 14.1% higher, and its thermal conductivity was also improved. The authors attributed the improved film quality to weaker phase explosion during ablation, which reduced the ejection of large neutral particles and lowered the kinetic energy of species reaching the substrate (Fig. 17(f)). Devices prepared with the melt-quenched target reached a PCE of 10.71%. Unencapsulated devices retained 93% of their initial efficiency after 150 days at 70% relative humidity under continuous indoor white-light illumination. The proposed plume mechanism would nevertheless benefit from direct measurements of particle-size and kinetic-energy distributions.

The reported results separate the roles of the principal PLD variables. Fluence sets the energy delivered by each pulse, repetition rate controls the delivery frequency, and target composition and structure determine the material entering the plume. During large-area deposition, target erosion and repeated plume overlap may cause thickness uniformity to diverge from composition and electronic quality. Spatially resolved composition measurements and in situ optical monitoring will therefore be needed to distinguish these effects.

Viewed together, vapor-based methods differ mainly in how precursors are delivered and which growth variable must remain stable during scale-up. In CVD, carrier-gas transport supplies volatile precursors, and film growth depends on the balance between gas-phase transport and surface-reaction kinetics. The main scale-up challenge is maintaining uniform precursor delivery and conversion. Thermal evaporation instead delivers molecular fluxes under high vacuum, making source flux, stoichiometric balance, and surface incorporation central; its scale-up depends on distributing these fluxes uniformly over large substrates. Energy-assisted methods generate the material flux through plasma or focused-beam interactions. Their critical variables include energy input, target response, and

target-to-film composition transfer, while scale-up must limit target evolution, energetic damage where relevant, and lateral flux non-uniformity.

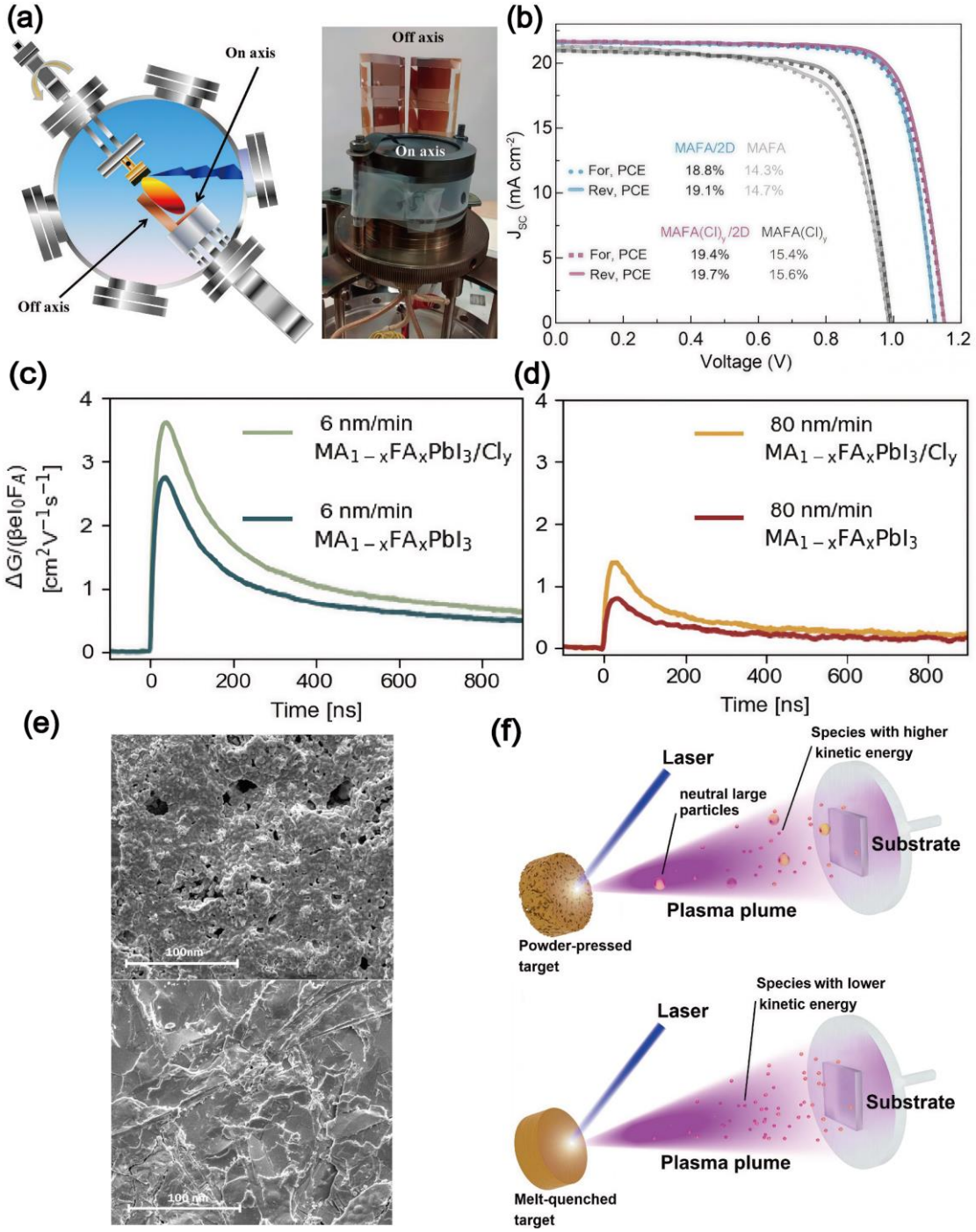

Fig. 17 (a) Schematic and substrate arrangements for on-axis and off-axis deposition of hybrid perovskite films. Reproduced with permission from Ref. [105], © American Chemical Society 2015. (b) Current density-voltage characteristics of devices containing single-source PLD-grown MA_{1-}

$_xFA_xPbI_3$ and $PbCl_2$-assisted $MA_{1-x}FA_xPbI_3$ absorbers, with and without OAmI surface passivation. Reproduced from Ref. [106] under CC BY, © The Authors 2023. (c, d) Time-resolved microwave conductivity (TRMC) photoconductance transients of films deposited at (c) 6 and (d) 80 $nm \cdot min^{-1}$ using targets with and without $PbCl_2$. Reproduced from Ref. [107] under CC BY 4.0, © The Authors 2025. (e) Top-view SEM images of powder-pressed and melt-quenched $CsPbBr_3$ targets. (f) Proposed effects of the two target structures on particle ejection and plume formation during PLD. Reproduced with permission from Ref. [109], © Wiley-VCH GmbH 2026.

5 Summary and outlook

This review has examined the fundamental mechanisms governing scalable perovskite thin-film formation across both solution-based and vapor-based deposition routes. Although these approaches employ distinct hardware platforms and precursor-delivery strategies, they share a common objective: achieving spatially uniform supersaturation, nucleation, crystal growth, and phase evolution over increasingly large areas while maintaining film quality and process reproducibility.

For solution-based deposition, including meniscus-guided coating, droplet-mediated deposition, and printing technologies, film formation is governed by the coupled evolution of fluid flow, solvent evaporation, solute transport, and crystallization. Scale-up introduces additional challenges associated with non-uniform drying, local concentration gradients, and synchronization of crystallization across large substrates. Consequently, controlling mass and heat transfer during wet-film evolution remains central to achieving uniform perovskite growth.

For vapor-based deposition, including CVD, thermal evaporation, sputtering, electron-beam evaporation, and pulsed laser deposition, growth is determined by precursor generation, gas-phase transport, surface reactions, and incorporation kinetics. Here, the major challenge shifts from wet-film

management to the precise control of precursor flux, stoichiometry, surface conversion, and non-equilibrium growth processes. Despite their differences, both solution and vapor routes ultimately seek to regulate the same fundamental quantity: the local driving force for perovskite phase formation.

Looking forward, several directions are expected to play increasingly important roles in advancing scalable perovskite manufacturing. First, more comprehensive multiscale models are needed to connect fluid dynamics, mass transport, nucleation, crystal growth, and defect formation across the broad temporal and spatial scales encountered in industrial production. Second, advanced in-situ and operando characterization techniques capable of tracking intermediate phases, local composition, and crystallization dynamics under realistic manufacturing conditions will be essential for validating mechanistic models. Third, the integration of machine learning, digital twins, and real-time process control may enable predictive optimization of deposition conditions and accelerate the transition from empirical process development to data-driven manufacturing. Finally, establishing unified process descriptors that are applicable across both solution and vapor deposition platforms could provide a common framework for comparing and optimizing scalable film-formation strategies. Experimentally accessible quantities, including wet-film thickness, solvent-evaporation rate, supersaturation rate, precursor flux, substrate temperature, and deposition rate, could serve as inputs for model validation, machine-learning optimization, digital-twin construction, and closed-loop process control. Ultimately, the future of perovskite manufacturing will depend not only on improvements in deposition equipment or device architecture, but also on a deeper mechanistic understanding of how transport phenomena, thermodynamics, and kinetics collectively govern film formation. Bridging crystallization science with manufacturing engineering will be critical for transforming perovskite technologies from laboratory demonstrations into reliable industrial products.

Availability of data and materials

The data and materials are available from the corresponding author upon reasonable request.

Competing interests

The authors have no competing interests to declare that are relevant to the content of this article.

Funding

Fundamental Research Funds for the Central Universities (No. 2026201007);

Open fund of State Key Laboratory of Solidification Processing in NPU (Grant No.SKLSP202517).

Author contributions

Qirui Deng: Writing - original draft, Writing - review and editing, Visualization, Data curation, Formal analysis. **Hu Guo**: Conceptualization, Methodology, Writing - original draft. **Ruihao Chen**: Writing - original draft, Writing - review and editing. **Yuanhang Cheng**: Funding acquisition, Supervision, Project administration, Writing - review and editing.

Acknowledgements

Y. Cheng thanks the funding supported by the Fundamental Research Funds for the Central Universities (No. 2026201007), as well as the support by the fund of the State Key Laboratory of Solidification Processing in NPU (Grant No.SKLSP202517).

References

[1] Pelay U, Luo L, Fan Y, *et al.* Thermal energy storage systems for concentrated solar power plants. *Renew Sustain Energy Rev* 2017, **79**: 82–100.

[2] Wang G, Yao Y, Chen Z, *et al.* Thermodynamic and optical analyses of a hybrid solar CPV/T system with high solar concentrating uniformity based on spectral beam splitting technology. *Energy* 2019, **166**: 256–266.

[3] National Renewable Energy Laboratory. Best Research-Cell Efficiency Chart. Information on https://www.nrel.gov/pv/interactive-cell-efficiency.html

[4] Green MA, Dunlop ED, Yoshita M, *et al.* Solar cell efficiency tables (Version 66). *Prog Photovolt Res Appl* 2025, **33**: 795–810.

[5] Chen J, Zhu GP, Wang KL, *et al.* Unveiling full-dimensional distribution of trap states toward highly efficient perovskite photovoltaics. *eScience* 2025, **5**: 100326.

[6] Davis RL, Jayaraman S, Chaikin PM, *et al.* Creating controlled thickness gradients in polymer thin films via flowcoating. *Langmuir* 2014, **30**: 5637–5644.

[7] Probstein RF. *Physicochemical Hydrodynamics: An Introduction*. 2nd ed. Hoboken (USA): John Wiley & Sons, 2005.

[8] Kang B, Yan F. Emerging strategies for the large-scale fabrication of perovskite solar modules: from design to process. *Energy Environ Sci* 2025, **18**: 3917–3954.

[9] Wang Z, Duan X, Zhang J, *et al.* Manipulating the crystallization kinetics of halide perovskites for large-area solar modules. *Commun Mater* 2024, **5**: 131.

[10] Zhou Y, Game OS, Pang S, *et al.* Microstructures of organometal trihalide perovskites for solar cells: Their evolution from solutions and characterization. *J Phys Chem Lett* 2015, **6**: 4827–4839.

[11] Kwon SG, Hyeon T. Formation mechanisms of uniform nanocrystals via hot-injection and heat-up methods. *Small* 2011, **7**: 2685–2702.

[12] Lee J, Lee D, Jeong D, *et al.* Control of crystal growth toward scalable fabrication of perovskite solar cells. *Adv Funct Mater* 2019, **29**: 1807047.

[13] Whitehead CB, Özkar S, Finke RG. LaMer's 1950 model for particle formation of instantaneous nucleation and diffusion-controlled growth: A historical look at the model's origins, assumptions, equations, and underlying sulfur sol formation kinetics data. *Chem Mater* 2019, **31**: 7116–7132.

[14] Zhao H, Li C, Zhang Y, *et al.* Defect suppression via tailoring functionalized additives for efficient and stable $CsPbI_3$ perovskite solar cells. *Carbon Energy* 2026, **8**: e70107.

[15] Liu H, Liu K, Zhang B, *et al.* Data-driven design of scalable perovskite film fabrication via machine learning-guided processing. *Carbon Energy* 2026, **8**: e70164.

[16] Li J, Munir R, Fan Y, *et al.* Phase transition control for high-performance blade-coated perovskite solar cells. *Joule* 2018, **2**: 1313–1330.

[17] Deng Y, Zheng X, Bai Y, *et al.* Surfactant-controlled ink drying enables high-speed deposition of perovskite films for efficient photovoltaic modules. *Nat Energy* 2018, **3**: 560–566.

[18] Bu T, Ono LK, Li J, *et al.* Modulating crystal growth of formamidinium–caesium perovskites for over 200 cm^2 photovoltaic sub-modules. *Nat Energy* 2022, **7**: 528–536.

[19] Butt MA. Thin-film coating methods: A successful marriage of high-quality and cost-effectiveness—A brief exploration. *Coatings* 2022, **12**: 1115.

[20] Deng Y, Van Brackle CH, Dai X, *et al.* Tailoring solvent coordination for high-speed, room-temperature blading of perovskite photovoltaic films. *Sci Adv* 2019, **5**: eaax7537.

[21] Hamukwaya SL, Hao H, Zhao Z, *et al.* A review of recent developments in preparation methods for large-area perovskite solar cells. *Coatings* 2022, **12**: 252.

[22] Li J, Dagar J, Shargaieva O, *et al.* Ink design enabling slot-die coated perovskite solar cells with >22% power conversion efficiency, micro-modules, and 1 year of outdoor performance evaluation. *Adv Energy Mater* 2023, **13**: 2203898.

[23] Geistert K, Ternes S, Ritzer DB, *et al.* Controlling thin film morphology formation during gas quenching of slot-die coated perovskite solar modules. *ACS Appl Mater Interfaces* 2023, **15**: 52519–52529.

[24] Zimmermann I, Al Atem M, Fournier O, *et al.* Sequentially slot-die-coated perovskite for efficient and scalable solar cells. *Adv Mater Interfaces* 2021, **8**: 2100743.

[25] Matondo JT, Hu H, Ding Y, *et al.* Slot-die coating for scalable fabrication of perovskite solar cells and modules. *Adv Mater Technol* 2024, **9**: 2302082.

[26] Aqeel AB, Mohasan M, Lv P, *et al.* Effects of nozzle and fluid properties on the drop formation dynamics in a drop-on-demand inkjet printing. *Appl Math Mech* 2019, **40**: 1239–1254.

[27] Bastola A, He Y, Im J, *et al.* Formulation of functional materials for inkjet printing: A pathway towards fully 3D printed electronics. *Mater Today Electron* 2023, **6**: 100058.

[28] Yarin AL. Drop impact dynamics: splashing, spreading, receding, bouncing…. *Annu Rev Fluid Mech* 2006, **38**: 159–192.

[29] Chen H, Ding X, Pan X, *et al.* Comprehensive studies of air-brush spray deposition used in fabricating high-efficiency $CH_3NH_3PbI_3$ perovskite solar cells: Combining theories with practices. *J Power Sources* 2018, **402**: 82–90.

[30] Feng X, Xu F, Peng C, *et al.* Confined crystallization strategy enabling high-quality perovskite film for advanced photovoltaics. *Joule* 2026, **10**: 102228.

[31] Heo JH, Zhang F, Xiao C, *et al.* Efficient and stable graded $CsPbI_{3-x}Br_x$ perovskite solar cells and submodules by orthogonal processable spray coating. *Joule* 2021, **5**: 481–494.

[32] Niu X, Li N, Cui Z, *et al.* Anion confinement for homogeneous mixed halide perovskite film growth by electrospray. *Adv Mater* 2023, **35**: 2305822.

[33] Cai H, Liang X, Ye X, *et al.* High efficiency over 20% of perovskite solar cells by spray coating via a simple process. *ACS Appl Energy Mater* 2020, **3**: 9696–9702.

[34] Heo JH, Lee MH, Jang MH, *et al.* Highly efficient $CH_3NH_3PbI_{3-x}Cl_x$ mixed halide perovskite solar cells prepared by re-dissolution and crystal grain growth via spray coating. *J Mater Chem A* 2016, **4**: 17636–17642.

[35] Wei Z, Chen H, Yan K, *et al.* Inkjet printing and instant chemical transformation of a $CH_3NH_3PbI_3$/nanocarbon electrode and interface for planar perovskite solar cells. *Angew Chem Int Ed* 2014, **53**: 13239–13243.

[36] Eggers H, Schackmar F, Abzieher T, *et al.* Inkjet-printed micrometer-thick perovskite solar cells with large columnar grains. *Adv Energy Mater* 2020, **10**: 1903184.

[37] Chalkias DA, Mourtzikou A, Katsagounos G, *et al.* Development of greener and stable inkjet-printable perovskite precursor inks for all-printed annealing-free perovskite solar mini-modules manufacturing. *Small Methods* 2023, **7**: 2300664.

[38] Jiang J, Chen X, Mei Z, *et al.* Review of droplet printing technologies for flexible electronic devices: Materials, control, and applications. *Micromachines* 2024, **15**: 333.

[39] Chen C, Chen J, Han H, *et al.* Perovskite solar cells based on screen-printed thin films. *Nature* 2022, **612**: 266–271.

[40] Chen C, Ran C, Guo C, *et al.* Fully screen-printed perovskite solar cells with 17% efficiency via tailoring confined perovskite crystallization within mesoporous layer. *Adv Energy Mater* 2023, **13**: 2302654.

[41] Yao Q, Gu Z, Chen C, *et al.* Weakening solvent-solute interactions for high-efficiency screen-printed perovskite solar cells. *Angew Chem Int Ed* 2025, **64**: e202501350.

[42] De Rossi F, Baker JA, Beynon D, *et al.* All printable perovskite solar modules with 198 cm^2 active area and over 6% efficiency. *Adv Mater Technol* 2018, **3**: 1800156.

[43] Huddy JE, Scheideler WJ. Rapid 2D patterning of high-performance perovskites using large-area flexography. *Adv Funct Mater* 2023, **33**: 2306312.

[44] Bould DC, Hamblyn SM, Gethin DT, *et al.* Effect of impression pressure and anilox specification on solid and halftone density. *Proc Inst Mech Eng Part B J Eng Manuf* 2011, **225**: 699–709.

[45] Huddy JE, Li Y, Klymenko M, *et al.* Spatial-uniformity-driven Bayesian optimization for rapid development of printed perovskite solar cells. *Small* 2026, **22**: e11799.

[46] Grau G, Kitsomboonloha R, Subramanian V. Fabrication of a high-resolution roll for gravure printing of 2 μm features. In: *Organic Field-Effect Transistors XIV; and Organic Sensors and Bioelectronics VIII*. Kymissis I, Shinar R, Torsi L, *et al.*, Eds. Bellingham (USA): SPIE, 2015: 95680M.

[47] Kim YY, Yang T, Suhonen R, *et al.* Gravure-printed flexible perovskite solar cells: Toward roll-to-roll manufacturing. *Adv Sci* 2019, **6**: 1802094.

[48] Kim YY, Yang TY, Suhonen R, *et al.* Roll-to-roll gravure-printed flexible perovskite solar cells using eco-friendly antisolvent bathing with wide processing window. *Nat Commun* 2020, **11**: 5146.

[49] Bisconti F, Giuri A, Suhonen R, *et al.* One-step polymer assisted roll-to-roll gravure-printed perovskite solar cells without using anti-solvent bathing. *Cell Rep Phys Sci* 2021, **2**: 100639.

[50] Vanni N, Giuri A, Calora M, *et al.* Camphorsulfonic-salified chitosan allowing MACl-free stabilization of pure $FAPbI_3$ α-phase via gravure printing in ambient air. *Sol RRL* 2024, **8**: 2400612.

[51] Sico G, Montanino M, Loffredo F, *et al.* Gravure printing for PVDF thin-film pyroelectric device manufacture. *Coatings* 2022, **12**: 1020.

[52] Langmuir I. The adsorption of gases on plane surfaces of glass, mica and platinum. *J Am Chem Soc* 1918, **40**: 1361–1403.

[53] Miyamoto S. A theory of the rate of sublimation. *Bull Chem Soc Jpn* 1933, **8**: 326–331.

[54] Dualeh A, Gao P, Seok SI, *et al.* Thermal behavior of methylammonium lead-trihalide perovskite photovoltaic light harvesters. *Chem Mater* 2014, **26**: 6160–6164.

[55] Platten JK. The Soret effect: a review of recent experimental results. *J Appl Mech* 2006, **73**: 5–15.

[56] Weickert J, Benhamouda B. A semidiscrete nonlinear scale-space theory and its relation to the Perona–Malik paradox. In: *Advances in Computer Vision*. Solina F, Kropatsch WG, Klette R, Bajcsy R, Eds. Vienna (Austria): Springer, 1997: 1–10.

[57] McGee HA. *Molecular Engineering*. New York (USA): McGraw-Hill, 1991.

[58] Neufeld PD, Janzen AR, Aziz R. Empirical equations to calculate 16 of the transport collision integrals Ω (l, s)* for the Lennard-Jones (12–6) potential. *J Chem Phys* 1972, **57**: 1100–1102.

[59] Limbu TB, Adhikari B, Song SK, *et al.* Toward understanding the phase-selective growth mechanism of films and geometrically-shaped flakes of 2D $MoTe_2$. *RSC Adv* 2021, **11**: 38839–38848.

[60] Jensen KF, Graves DB. Modeling and analysis of low pressure CVD reactors. *J Electrochem Soc* 1983, **130**: 1950–1957.

[61] Wang B, Young Wong K, Xiao X, *et al.* Elucidating the reaction pathways in the synthesis of organolead trihalide perovskite for high-performance solar cells. *Sci Rep* 2015, **5**: 10557.

[62] Tavakoli MM, Gu L, Gao Y, *et al.* Fabrication of efficient planar perovskite solar cells using a one-step chemical vapor deposition method. *Sci Rep* 2015, **5**: 14083.

[63] Muratov DS, Luchnikov LO, Saranin DS, *et al.* Single-step chemical vapor deposition of methyl ammonium lead halide perovskite for p-i-n solar cells. *ChemistrySelect* 2024, **9**: e202400147.

[64] Bryan AC, Meyers JK, Serafin LY, *et al.* Metal organic chemical vapor deposition of hybrid perovskites. *J Am Chem Soc* 2025, **147**: 10212–10218.

[65] Zhu R, Wei X, Xie G, *et al.* Numerical simulation of vapor deposition process of perovskite solar cells: The influence of methylammonium iodide vapor flow to perovskite growth. *J Sol Energy Eng* 2021, **143**: 011002.

[66] Leyden MR, Ono LK, Raga SR, *et al.* High performance perovskite solar cells by hybrid chemical vapor deposition. *J Mater Chem A* 2014, **2**: 18742–18745.

[67] Moser T, Kothandaraman R, Yang S, *et al.* Understanding the formation process of perovskite layers grown by chemical vapour deposition. *Front Energy Res* 2022, **10**: 883882.

[68] Qiu L, He S, Jiang Y, *et al.* Hybrid chemical vapor deposition enables scalable and stable Cs-FA mixed cation perovskite solar modules with a designated area of 91.8 cm^2 approaching 10% efficiency. *J Mater Chem A* 2019, **7**: 6920–6929.

[69] Qiu L, He S, Liu Z, *et al.* Rapid hybrid chemical vapor deposition for efficient and hysteresis-free perovskite solar modules with an operation lifetime exceeding 800 hours. *J Mater Chem A* 2020, **8**: 23404–23412.

[70] Fernández FE. Enhancement of thickness uniformity of thin films grown by pulsed laser deposition. *J Vac Sci Technol A* 1995, **13**: 421–427.

[71] Maissel LI, Glang R, Eds. *Handbook of Thin Film Technology*. New York (USA): McGraw-Hill, 1970.

[72] Sun J, Zhang W, Yi K, *et al.* Optimization of thickness uniformity of coatings on spherical substrates using shadow masks in a planetary rotation system. *Chin Opt Lett* 2014, **12**: 053101.

[73] Schroeder SLM, Gottfried M. *Temperature-Programmed Desorption (TPD): Thermal Desorption Spectroscopy (TDS)*. Advanced Physical Chemistry Laboratory, Freie Universität Berlin, 2002: 1–22. Information on https://pcprakt.userpage.fu-berlin.de/pdf_block_IV/TDS.pdf

[74] Poodt P, van Lieshout J, Illiberi A, *et al.* On the kinetics of spatial atomic layer deposition. *J Vac Sci Technol A* 2013, **31**: 01A108.

[75] Swenson H, Stadie NP. Langmuir's theory of adsorption: A centennial review. *Langmuir* 2019, **35**: 5409–5426.

[76] Longo G, Gil-Escrig L, Degen MJ, *et al.* Perovskite solar cells prepared by flash evaporation. *Chem Commun* 2015, **51**: 7376–7378.

[77] Liang G, Lan H, Fan P, *et al.* Highly uniform large-area (100 cm^2) perovskite $CH_3NH_3PbI_3$ thin-films prepared by single-source thermal evaporation. *Coatings* 2018, **8**: 256.

[78] Abzieher T, Muzzillo CP, Mirzokarimov M, *et al.* Continuous flash sublimation of inorganic halide perovskites: overcoming rate and continuity limitations of vapor deposition. *J Mater Chem A* 2024, **12**: 8405–8419.

[79] Yang L, Xie J, Su Z, *et al.* CsCl seed layer engineering for buried-interface modification enabling >20% efficiency in single-source vapor-deposited perovskite solar cells. *J Mater Chem A* 2026, **14**: 13462–13470.

[80] Liu M, Johnston MB, Snaith HJ. Efficient planar heterojunction perovskite solar cells by vapour deposition. *Nature* 2013, **501**: 395–398.

[81] Roß M, Gil-Escrig L, Al-Ashouri A, *et al.* Co-evaporated pin perovskite solar cells beyond 20% efficiency: impact of substrate temperature and hole-transport layer. *ACS Appl Mater Interfaces* 2020, **12**: 39261–39272.

[82] Ritzer DB, Abzieher T, Basibüyük A, *et al.* Upscaling of perovskite solar modules: The synergy of fully evaporated layer fabrication and all-laser-scribed interconnections. *Prog Photovolt Res Appl* 2022, **30**: 360–373.

[83] Shen X, Hui WT, Hu S, *et al.* Crystal-facet-directed all-vacuum-deposited perovskite solar cells. *Nat Mater* 2026, **25**: 999–1010.

[84] Cvitaš T. The Gibbs function of a chemical reaction. *Croat Chem Acta* 2007, **80**: 605–612.

[85] Crank J. *The Mathematics of Diffusion*. 2nd ed. Oxford (UK): Clarendon Press, 1979.

[86] Butrymowicz DB, Manning JR, Read ME. Diffusion in copper and copper alloys part IV. Diffusion in systems involving elements of group VIII. *J Phys Chem Ref Data* 1976, **5**: 103–200.

[87] Chen C, Kang H, Hsiao S, *et al.* Efficient and uniform planar-type perovskite solar cells by simple sequential vacuum deposition. *Adv Mater* 2014, **26**: 6647–6652.

[88] Feng J, Jiao Y, Wang H, *et al.* High-throughput large-area vacuum deposition for high-performance formamidine-based perovskite solar cells. *Energy Environ Sci* 2021, **14**: 3035–3043.

[89] Li H, Zhou J, Tan L, *et al.* Sequential vacuum-evaporated perovskite solar cells with more than 24% efficiency. *Sci Adv* 2022, **8**: eabo7422.

[90] Schulz T, Maiberg M, Schrader M, *et al.* Quantitative analysis of FAI-diffusion in sequentially evaporated $FAPbI_3$ perovskite thin films. *Phys Chem Chem Phys* 2026, **28**: 10169–10181.

[91] Goebel DM, Katz I, Mikellides IG. *Fundamentals of Electric Propulsion*. 2nd ed. Hoboken (USA): John Wiley & Sons, 2023.

[92] Daniels S. PVD process modelling and deposition into sub-micron features. Ph.D. Thesis. Dublin (Ireland): Dublin City University, 1999.

[93] Lundin D, Sarakinos K. An introduction to thin film processing using high-power impulse magnetron sputtering. *J Mater Res* 2012, **27**: 780–792.

[94] Mahne N, Čekada M, Panjan M. Total and differential sputtering yields explored by SRIM simulations. *Coatings* 2022, **12**: 1541.

[95] Raifuku I, Ishikawa Y, Bourgeteau T, *et al.* Fabrication of perovskite solar cells using sputter-processed $CH_3NH_3PbI_3$ films. *Appl Phys Express* 2017, **10**: 094101.

[96] Gao B, Zuo Z, Hu J, *et al.* Controlled solid-state phase transition of formamidinium dominated perovskite layers fabricated through magnetron sputtering for photovoltaics. *Adv Funct Mater* 2024, **34**: 2410428.

[97] Peng Z, Zuo Z, Qi Q, *et al.* Perovskite solar cells with all functional layers deposited by magnetron sputtering. *ACS Appl Energy Mater* 2023, **6**: 7556–7562.

[98] Laxmi L, Shilovskikh VV, Singh S, *et al.* Magnetron sputtering of hybrid metal halide perovskites: barriers to scalable fabrication. *EES Sol* 2026, **2**: 469–478.

[99] Liu L, Yang SE, Liu P, *et al.* High-quality and full-coverage $CsPbBr_3$ thin films via electron beam evaporation with post-annealing treatment for all-inorganic perovskite solar cells. *Sol Energy* 2022, **232**: 320–327.

[100] He B, Jiao D, Liu L, *et al.* Influence of water–vapor treatment on the properties of $CsPbBr_3$ perovskite solar cells. *Eur Phys J Plus* 2023, **138**: 412.

[101] Shepelin NA, Tehrani ZP, Ohannessian N, *et al.* A practical guide to pulsed laser deposition. *Chem Soc Rev* 2023, **52**: 2294–2321.

[102] Sancaktar E. Using excimer laser for manufacturing stimuli responsive membranes. *Membranes* 2023, **13**: 398.

[103] Hodapp TW, Fleming PR. Modeling topology formation during laser ablation. *J Appl Phys* 1998, **84**: 577–583.

[104] Willmott PR, Huber JR. Pulsed laser vaporization and deposition. *Rev Mod Phys* 2000, **72**: 315–328.

[105] Bansode U, Naphade R, Game O, *et al.* Hybrid perovskite films by a new variant of pulsed excimer laser deposition: A room-temperature dry process. *J Phys Chem C* 2015, **119**: 9177–9185.

[106] Soto-Montero T, Kralj S, Soltanpoor W, *et al.* Single-source vapor-deposition of $MA_{1-x}FA_xPbI_3$ perovskite absorbers for solar cells. *Adv Funct Mater* 2024, **34**: 2300588.

[107] Kliner V, Soto-Montero T, Nespoli J, *et al.* Pulsed laser deposition of halide perovskites with over 10-fold enhanced deposition rates. *J Phys Chem Lett* 2025, **16**: 1453–1460.

[108] Wang H, Wu Y, Ma M, *et al.* Pulsed laser deposition of $CsPbBr_3$ films for application in perovskite solar cells. *ACS Appl Energy Mater* 2019, **2**: 2305–2312.

[109] Fan X, Zhang H, Lu X, *et al.* Pulsed laser deposited $CsPbBr_3$ perovskite solar cells achieving 10.71% efficiency with exceptional long-term stability via target engineering. *Small* 2026, **22**: e73935.

Author biography

Qirui Deng received his B.E. degree from Nanjing University of Science and Technology in 2024. He is now a master candidate at Nanjing University of Science and Technology. His research focuses on

normal-bandgap perovskite solar cells, as well as the scalable fabrication of perovskite films using blade coating method.

Yuanhang Cheng is a professor at the School of New Energy, Nanjing University of Science and Technology (NJUST). Before joining NJUST, he was a research associate at the City University of Hong Kong (CityU) from 2021 to 2022. He also worked as a research fellow at the Solar Energy Research Institute of Singapore (SERIS), National University of Singapore (NUS) from 2018 to 2021. His research interests include highly efficient perovskite solar cells, new photovoltaic materials with various organic-inorganic composites, and solar-powered photoelectrochemical applications.

Author Name

Qirui Deng, Hu Guo, Ruihao Chen, Yuanhang Cheng

Graphical abstract

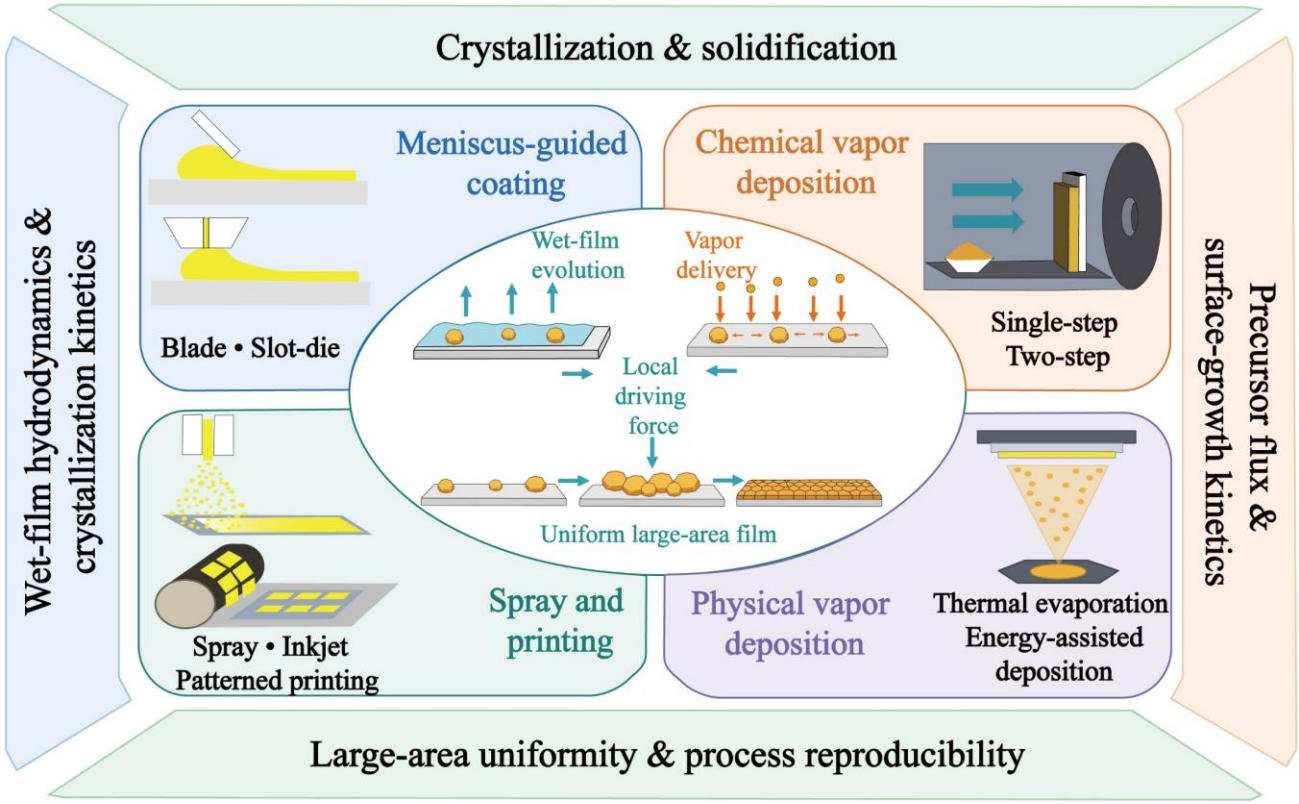

Overview of scalable perovskite film formation through solution- and vapor-based deposition routes, highlighting precursor transport, crystallization and solidification, and large-area film uniformity and process reproducibility.